CHARACTERIZATION OF NORMAL AND ABNORMAL BONES BY RAMAN SPECTROSCOPY

ANALYSIS OF MINERAL TO MATRIX RATIO OF BONE USING ADVANCED MATERIALS CHARACTERIZATION TECHNIQUES

by

MEET YAGNESH SHAH

Presented to the Faculty of the Graduate School of

The University of Texas at Arlington in Partial Fulfillment

of the Requirements

for the Degree of

MASTER OF SCIENCE IN MATERIALS SCIENCE AND ENGINEERING

THE UNIVERSITY OF TEXAS AT ARLINGTON

May 2018

Acknowledgements

I am delighted to express my gratitude to Dr. Harry Fred Tibbals for his excellent guidance, advice, and support throughout the two years of the thesis. This work is made possible due to his thorough interest and presence. Dr. Tibbals has always given me the best guidance whether it is related to the biology of the bone or materials science. I have gained a good experience working with him which will be very useful for my future career.

I am very thankful to Dr. Efstathios I Meletis for his invaluable guidance and support towards the thesis. I am also grateful to Dr. Jiechao Jiang, Mr. David Yan, and Materials Science and Engineering department for providing me the opportunity to work in the Laboratory.

I would also like to express my gratitude to Dr. Johnathan Rios and his team for providing us the rat bones samples. I also appreciate Mr. Bill Pierce and Texas Scottish Rite Hospital for allowing us to visit different laboratories and providing us the instruments we needed.

I would also like to thank Dr. Harry Fred Tibbals, Dr. Efstathios I Meletis and Dr. Yaowu Hao for taking part as a committee member. I appreciate Dr. Johnathan Rios for spending his invaluable time to attend my thesis defense session.

I am very thankful to my colleague Mr. Sunil Yadav for his help and support throughout the completion of this thesis.

I am very thankful to my family and my friends for their love and invaluable support towards my career.

April 13, 2018

Abstract

CHARACTERIZATION OF NORMAL AND ABNORMAL BONES BY RAMAN SPECTROSCOPY

ANALYSIS OF MINERAL TO MATRIX RATIO OF BONE USING ADVANCED MATERIALS CHARACTERIZATION TECHNIQUES

MEET YAGNESH SHAH, M.S

The University of Texas Arlington, 2018

Supervising Professor: Harry Fred Tibbals

Bone disorders and disease are associated with multiple factors. Some of the disorders and diseases are difficult to understand because of their unknown root causes. Our goal was to differentiate between normal and genetically modified rat bone groups by finding the difference in mineral to matrix (Mn/Mx) content using Raman spectroscopy. Raman spectroscopy gives the chemical composition based on the vibration modes of the molecules. Quantitative analysis of Mn/Mx content calculated from Raman spectra allowed us to distinguish between healthy and genetically modified rat bone groups. We have presented the results by averaging the Mn/Mx ratios. Thus, the most significant result is the finding that mineral to matrix content is higher in bone in which the specific genetic bone growth factor was downregulated by disabling the gene. This higher mineral to matrix content in abnormal bones may indicate that this genetic factor primarily influences the growth of bone matrix, which gives the bone its toughness and flexibility.

Table of Content

List of Illustrations

Figure Page

List of Tables

Chapter 1 Introduction

1.1 Motivation

Our main aim in this thesis was to determine the difference in mineral to matrix (Mn/Mx) content between normal and abnormal rat bones using Raman spectroscopy. This project is a part of research in the Texas Scottish Rite Children's Hospital. The research is related to the etiology of clubfoot in humans. The Follistatin-like 5 (FSTL 5) gene is associated with this disorder. So, the project aims to check whether the advanced materials characterization techniques are helpful in distinguishing between normal and abnormal rat bones. According to the hypothesis, due to the disability of FSTL5, the abnormal rat bones should have a higher mineral to matrix content than normal rat bones.

1.2 Summary of Data and Results

This thesis is about distinguishing between the normal (healthy wild-type [WT]) and abnormal (knockout [KO], FSTL5 disabled) rat bones. We measured leg bones from normal and genetically altered Sprague-Dawley rats using Raman laser spectroscopy. This research is unique because it is for the first time when measurement of Mn/Mx ratio of normal rat bone and the specific type of genetically modified rat bone (FSTL5 disabled) is compared. The genetically modified rats were produced in a research project at UT Southwestern and Texas Scottish Rite Children's Hospital; the project explored the causes of clubfoot and other bone disorders in humans. We obtained a total of 27 female rat samples with five different age groups. Among them, we used 18 samples for the analysis of the outer shell (periosteum) and a total of 15 samples for the analysis of cortical bone. The data from these groups are presented separately below.

From the Raman spectra, we calculated the Mn/Mx ratio using a standard technique accepted in the biomedical literature based on the ratio of two characteristic

peak heights. To obtain correlating information on the structure of the bone tissues, we also carried out images and element mappings of the bone microstructure using scanning electron microscopy (SEM) with energy-dispersive spectroscopy (EDS).

We developed and refined our experimental technique to ensure measurements reflected an accurate average over the heterogeneous micro regions of the bone tissue. After doing this, we found a significantly higher mineral to matrix content in the genetically modified rats. Although this difference could be useful in explaining the etiology of certain bone disorders, such as clubfoot, our focus was only on the mineral to matrix ratios and how accurately they could be determined using Raman spectroscopy.

The imaging and element mapping showed that the bone is composed of heterogeneous regions with differing mineral content. The spectra can reflect only a highly variable local mineral content because the laser spot size (3.1 microns) is smaller than the observed bone tissue domains. It is necessary to take an average of many laser spot Raman spectral readings to obtain an accurate overall measure of mineral to matrix ratio. In the sections below, we describe briefly: (1) the biomedical significance and motivation based on bone disorders, (2) the structure and anatomy of the bone, and (3) the theory and experimental basis for the characterization methods.

In the remaining sections, the complete data sets obtained are given, with an explanation of how the final experimental protocol was developed and tested. The Raman spectral data for individual laser spot measurements are shown and compared with the final results based on an average over a range of spots. For that, we scanned over a localized bone region, which is large, relative to the microscopic heterogeneous variations in bone structure. The final groups of average scanned results are more consistent and representative of the overall bone mineral content.

We conclude that when using the relatively novel laser spot technique, care must be taken to consider the effects of laser spot size and positioning. Many of the previous techniques used to obtain the Mn/Mx ratio were done by grinding up the bone and mixing it with infrared transparent salts to get the Raman spectrum. The newer Raman laser instrumentation has the potential to measure bone directly without disruption of microstructure, and with much greater efficiency and flexibility of measurement. The SEM and EDS results revealed interesting details of the different anatomical bone growth regions and bone microstructure, which may be useful in future work in collaboration with biomedical investigators, but an exploration was beyond the scope of this work.

Thus, the most significant result is the finding that mineral content is higher in bone in which the specific genetic bone growth factor was downregulated. This higher mineral to matrix content in abnormal bones may indicate that this genetic factor primarily influences the growth of bone matrix, which gives bone its toughness and flexibility.

Among all advanced materials characterization techniques, we focused on Raman spectroscopy, SEM and EDS. Concentrating on the cortical bone of tibia, we found some significant differences. The analysis of these two techniques strengthens the data of Raman.

1.3 Mn/Mx Ratio in Clubfoot

The FSTL5 is implicated in the variation of Mn/Mx ratio and with many disorders, including clubfoot. Clubfoot (congenital talipes equinovarus) is a birth disorder associated with bone growth. According to a study, it occurs one per one 1,000 births [1]. The disorder causes one or both lower limbs to stay in a mild or rigid rotational state at birth as shown in Figure 1-1 [2]. The etiology of this disorder is still an area of interest for researchers. Although it is a somewhat common congenital disorder, there is a very poor understanding of its genotype. Using a genome-wide association approach, the

researchers of Texas Scottish Rite Hospital identified a significantly associated locus within FSTL5. Unlike early regulators of limb specification and development previously implicated in limb malformations, they showed that FSTL5 is expressed during later stages of distal limb development with expression restricted to the condensing cartilage growth destined to form the limb skeleton.

Figure 1-1 Image showing normal foot and clubfoot

Chapter 2 Background

Bone is the part of the body that sustains the outer stress coming to the body and transports it to other parts [3]. The natural structure and mechanical properties of bone allow the function of the regular routines of the body. It is essential to understand the basic composition and the structure of bone for the context of this study.

2.1 Bone Composition and its Function

There are two main phases present in the bone: (1) mineral and (2) matrix. Bone is a type of composite material, 65% of which consists an inorganic mineral compound in the form of hydroxyapatite and 25% of which is the matrix comprised of the organic compound. The remaining 10% is made up of water [4]. The inorganic compound is composed of phosphate, calcium, and carbonate. The matrix consists mainly of organic compounds, including Collagen I (90%), and the remainder is made up of different kinds of proteins. The mixture of all the mechanical properties, like strength, stiffness, toughness, and flexibility, depends on the amount of the mineral and matrix phases. The minerals contribute to providing better stiffness as well as tensile strength up to a certain extent, but excessive quantity may lead to brittleness in the bone [5] [6] [7] [8]. The size, orientation, and stoichiometry of the minerals also decide the mechanical properties [9]. The matrix portion provides the flexibility and toughness [5] [7] [10] [11]. Toughness is a fundamental mechanical property, defined as the ability of the material to absorb energy and plastically deform without fracture. The amount of collagen and its fiber orientation also control the mechanical properties. Figure 2-1 shows how minerals and matrix phases are present in the bone. Note that the brittle mineral is surrounded by the organic matrix to produce a tough composite structure.

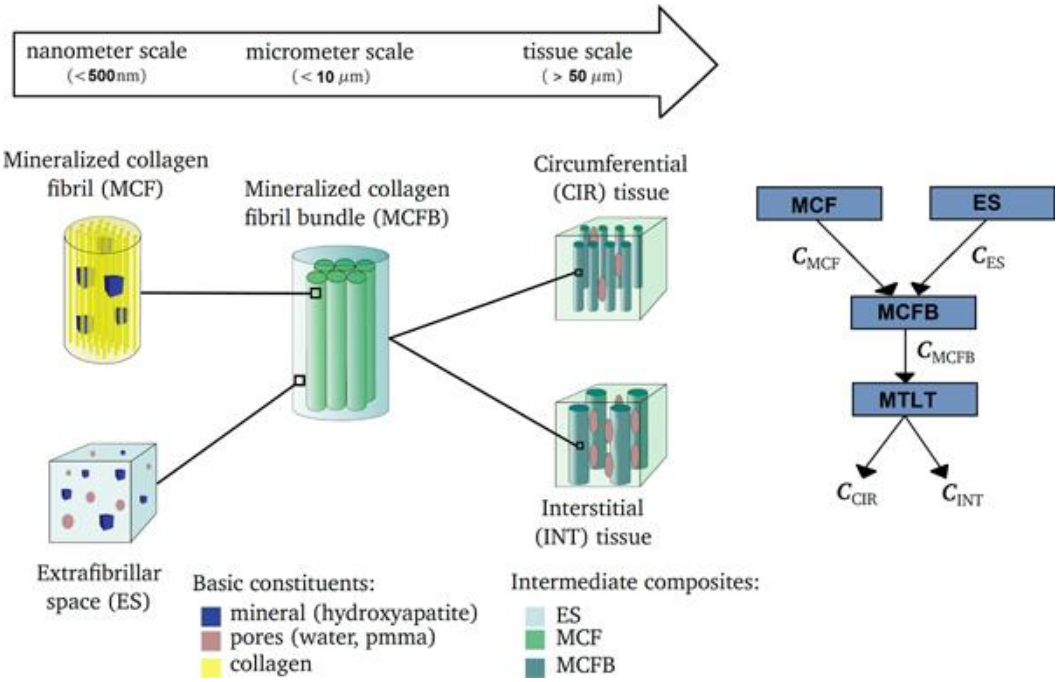

Figure 2-1 Arrangement of minerals and matrix in bone

2.2 Bone Structure

A body contains five different types of bones, including long, short, flat, irregular, and sesamoid. We focused our study on the long bones, which are called the femur and tibia. Figure 2-2 shows part of a femur bone. It represents the typical bone structure and its arrangement. The outer layer is called periosteum (membrane covering the bone). After removal of the outer shell, the longitudinal cut showing in the image describes different areas in the bone. The cortical bone and the cancellous bone are two different main portions. Our primary focus of the study was on the cortical bone of the tibia. The cortical bones contain mainly minerals, whereas spongy bone contains the majority of matrix content.

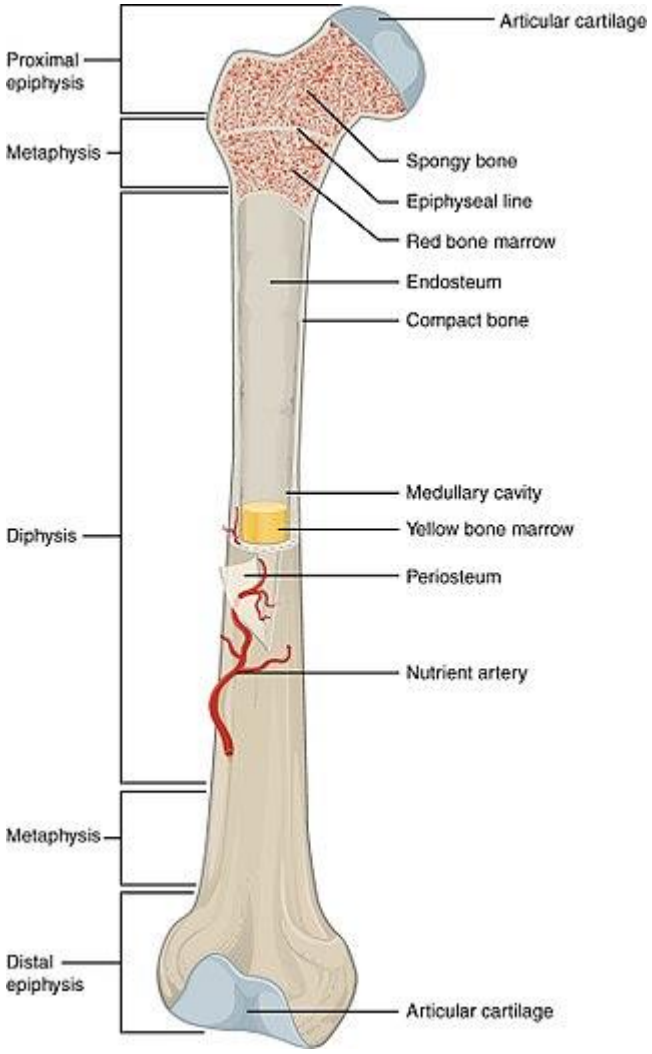

Figure 2-2 Image showing the structure of bone

Chapter 3 Characterization Techniques

We used Raman spectroscopy for this study as a leading technique for the characterization. Raman spectroscopy by scattered light gives information regarding the minerals and matrix content present in the bone. To strengthen the data obtained from Raman spectroscopy, we used SEM and EDS. This chapter describes the operation and mechanism behind these techniques.

3.1 Introduction to Raman Spectroscopy

Like in the past, the use of Raman spectroscopy is not limited to chemistry only. It is an expanding technique in biomechanics and the biomedical field because it is nondestructive and requires simple sample preparation. This chapter will provide information on the basics of Raman spectroscopy, which we used to find the Mn/Mx ratio. The Mn/Mx ratio is used to analyze a disorder of bone and correlate it with the strength of bone.

There are two different ways to explain the Raman effect in the material, which is related to molecular structure. Classical theory gives a clear but incomplete description of the interaction of molecules with light. Complete understanding requires the knowledge of quantum theory as well. This chapter will cover both approaches to understand the Raman effect, which will be very helpful in understanding the bone chemistry later.

Classical electrodynamic theory applied to Raman spectroscopy describes the interaction of light with chemical bonds in the material. As shown in Figure 3-1, bombarding the incident light on the substance creates an interaction with the molecules of the material and emits light with the same or a different frequency.

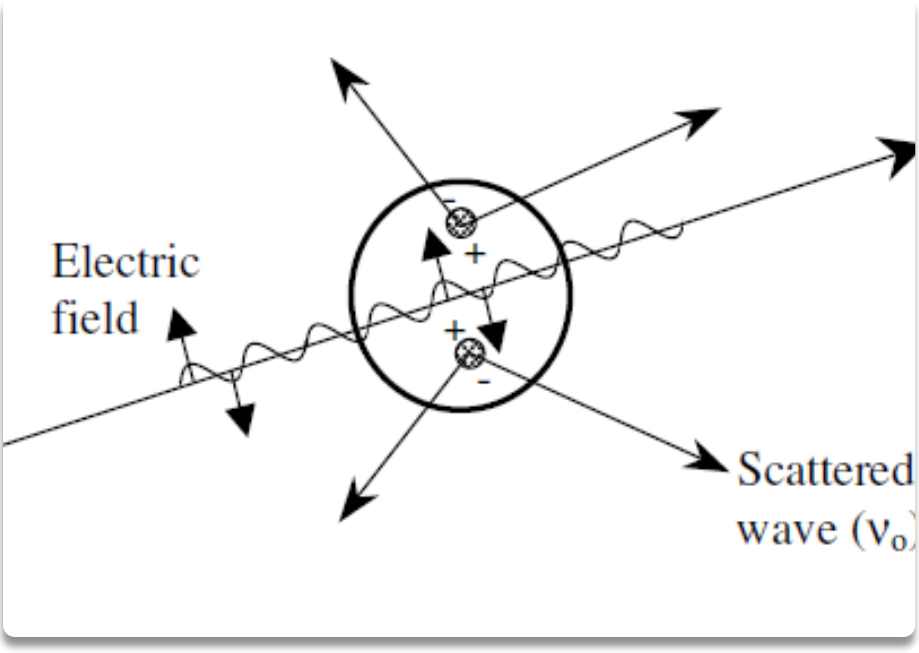

Figure 3-1 Image explaining the interaction of monochromatic light with the molecule

This frequency difference is due to molecular vibrations. When incident light interacts with the molecules, it induces a dipole moment. This dipole moment is strongly dependent on the polarizability of the material. In simple terms, polarizability is the ease with which the electron density distribution is distorted in an electric field. The following equation expresses this relation in mathematical terms:

$$\vec{P} = \tilde{\alpha}\ \overrightarrow{E}$$

Here, P is induced dipole moment, and α and E are polarizability and induced electric field, respectively. P and E are vectors, α is a tensor. Electromagnetic radiation creates an oscillating electric field that results in an oscillating dipole moment. So, the new electric field is given by the following equation:

$$E = E_0 \cos(2\pi\nu t)$$

Here, E_0 is a static electric field. So, the formula for a static dipole moment occurring due to the sinusoidal electric field is given as follows:

$$P = \alpha E_0 \cos(2\pi v t)$$

where *v* is the frequency of incident light while striking the substance. The polarizability of molecules can be described as Taylor' s expansion as follows:

$$\alpha = \alpha_0 + \frac{\partial \alpha}{\partial Q} Q + \cdots$$

So, the above equation consists of static polarizability (α_0) as well as the effect of different modes of vibration of molecules, where Q is the vibrational coordinate. Here, Q also varies sinusoidally with some molecular vibrational frequency, V_{vib}, which is given by

$$Q = Q_0 \cos (2\pi V_{vib} t)$$

Q_0 is the maximum value of Q. So, by solving all these equations, we get the following equation:

$$P = \alpha_o E_0 \cos (2\pi v t) + \frac{\partial \alpha}{\partial Q} {}_{Q_0 E_0/2} \; [\cos 2\pi(v - v_{vib})t) + \cos (2\pi(v + v_{vib}))$$

The first term indicates that the scattered light has the same frequency as the incident light. This elastic scattering is called Rayleigh scattering. The second term indicates that scattered light has a different frequency than the incident light. This inelastic is called Raman scattering. In Raman, scattering can result in a lower or higher frequency. These modes are called Stokes and anti-Stokes. It is quite clear from the equation that Stokes light has a lower frequency than incident light as it transfers some of its energy to molecules of the material. On the other hand, anti-Stokes light has a higher frequency than the incident light; the molecules transfer some energy to the scattered light.

Quantum mechanics theory can help give a clear idea of Raman spectroscopy. The inelastic scattering of light was discovered by Indian scientist Sir Chandrasekhara Venkata Raman, who was working with Rayleigh. When the incident photon of light

strikes the material, it makes the molecule change its energy state from ground to a virtual excited state. A second photon is scattered from the virtual energy level as the molecule returns to one of its allowed vibrational states. Here, the scattered photon can either have same quantum energy as the incident or can have different quantum energy than the incident. If both the energies are equal, then this type of scattering is called an elastic scattering or Rayleigh scattering. But If the photon coming from the virtual state has lower or higher energy, then this scattering is called inelastic scattering. It is clear from Figure 3-2 that if the scattered photon has lower quantum energy than the incident, it is called Raman Stokes scattering, whereas if it has higher energy than the incident, it is called Raman anti-Stokes scattering. The chances of an inelastic scattering are one in a billion.

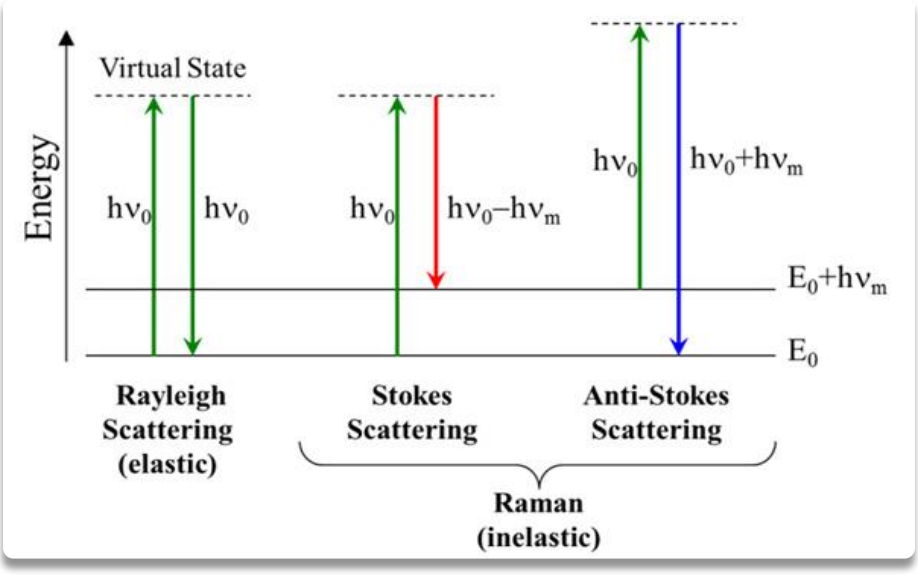

Figure 3-2 Image explaining Rayleigh and Raman scattering

In Figure 3-2, all the arrows going upward indicate the incident light. All the arrows coming downward indicate scattered light. The Figure shows that Rayleigh scattered light has the same energy state for both incident and scattered light, whereas

Stokes and anti-Stokes have lower and higher energy than incident light, respectively [12].

3.2 Scanning Electron Microscopy

SEM is a compelling technique for the characterization of materials such as bone. SEM is used to observe the microstructure of the sample at the macro/micro level, which can provide information regarding the surface morphology. Here, the electron beam is used as a source of energy for detection. When the electron beam strikes the sample surface, it interacts with the atoms on the surface and gives different kinds of signals. Most useful signals are secondary electrons and backscattered electrons. Other signals are augur electrons and X-rays. Before using the SEM, we need to know what information it gives based on these different signals. The following sections explain secondary and backscattered electron imaging modes.

3.2.1 Secondary Electron Imaging (SEI)

When the inelastic interaction between incident electrons and electrons of the atom occurs, the signals emitted are known as secondary electrons, which are detected by a positively biased detector. These scattered secondary electrons are collected and focused to form an image. Generally, the energy of the secondary electrons is lower compared to other electrons. The number of electrons scattered from holes or vacancies is smaller than from the defect-free surfaces. These regions with vacancies result in darker contrast, with less energy. But if there is a hill-like morphology on the surface, a higher number of electrons are scattered, resulting in a brighter contrast for that region. Thus, this is a useful technique in understanding the morphology of the sample surface.

3.2.2 Backscattered Electron Imaging (BEI)

Elastic events occur when the incident beam of electrons interacts with an atom nucleus. Thus, if the elastically scattered electrons reflect from the atoms, then these

electrons are termed “backscattered electrons.” BEI is highly dependent on the atomic number of the material. The materials having higher atomic numbers will give a greater number of backscattered electrons, whereas the materials having lower atomic numbers give a smaller number of backscattered electrons. So, the higher atomic number materials will show the brighter area on the screen. With this method, we can easily distinguish the different type of phase/materials present on the sample surface. When the sample is an alloy, BSE mode gives the better result.

For our research in rat bones, we used SEI mode, which requires material to be conductive. Bone is a nonconductive material, so it is difficult to operate with SEI mode unless we make it conductive. We coated the bone with silver and used SEI mode for the detection. We used the sputtering method for the coating of silver.

3.3 Raman Spectroscopy of Bone

Some of the reasons for increased use of Raman spectroscopy in biology are its lack of interference with water and that little or no sample preparation is required. Without the use of labeling, Raman microscopy can provide structure and biochemical information [13]. Raman spectroscopy is a potent technique in understanding the changes occurring in the tissue-level bone mechanical properties. This spectroscopy technique can provide information regarding the effects of matrix proteins on bone mechanical properties as well as the content of mineral and matrix components [14].

Previous studies of the cortical bone, including the chemical perturbations, resulting due to the application of mechanical loading in mice and bovine [15] [16] [17] [18]. The bones of rats, mice, and humans have also been the subjects of study of age-related changes [19] [20] [21]. In general, all of the studies state that with the increase in age, there is also an increase in mineral crystallinity, the degree of mineralization, and the degree of carbonate ions replacing the phosphate ions. One study has already

mapped the spatial distribution of mineral and protein in developing as well as in mature human cortical bones with the help of hyperspectral Raman imaging [22]. Raman spectroscopy has played an essential role in understanding the chemical changes of the cortical bone in conditions like osteogenesis imperfecta, early onset osteoarthritis, lead exposure, and also postmenopausal osteoporosis [23] [24] [25] [26].

While using Raman spectroscopy, it is very important to choose the right laser wavelength to strike. Because Raman scattering is an event with very low probability, it is easy for other signals to obscure the Raman signal from appearing. These other signals are generally considered as fluorescence. Tissue fluorescence efficiency of excitation is much higher than the Raman scattering, so there is a need to suppress those fluorescence efficiencies that obscure Raman signals. To lessen this issue, it is always preferred to work in the diagnostic window, which is 600 nm to 1100 nm [9]. Hence, we have used 780 nm for the best possible results.

Figure 3-3 is a standard Raman spectrum of bone (deproteinized), which represents the inorganic and organic substances present in the bone. Different peaks are the characteristics of various forms of bond such as phosphate, carbonate, amides, proline. They all are either organic substances or inorganic substances. Amide I contains most of the bone matrix assignments. Most of the peaks fall into the range of 400 cm^{-1} to 1700 cm^{-1}, which includes the peaks defining mineral and matrix content. The C-H and N-H bonds are missing in this region, which can be found in the 2900 cm^{-1} to 3300 cm^{-1} range. However, these peaks give little information, which is difficult to find in the lower wavenumber region [14].

Here, the most intense peak is the phosphate peak (PO_4^{2-}) at 959 cm^{-1}. There are some factors that can alter the peak position for a few wavenumbers, such as mineral carbonate (CO_3^{2-}) and monohydrogen phosphate (HPO_4^{2-}). An increase in HPO_4^{2-} may

result in the peak shift toward the lower wavenumber, which can be seen in newly deposited minerals [27] [28]. There is not only one peak that is occupied by phosphate, but there are some subpeaks as well, resulting in an intense but broader peak. The v2 and v4 as seen in Figure 3-3 are substitute peaks of the phosphate, and one more substitute peak of phosphate is obtained at 1076 cm^{-1}, which is called v3. Another mineral band is the carbonate v1 symmetric stretch (C-O stretch) at 1070 cm^{-1}. This small difference in wavenumbers of these peaks (v3 and v1) leads them to overlap each other. Care must be taken in the process of peak fitting for accurate measurements [29]. Similarly, like minerals, there are different peaks for the matrix as well. Among all matrix peaks, the most widely used bands are proline and hydroxyproline, which fall at 855 cm^{-1} and 875 cm^{-1}, respectively [9]. These peaks represent collagen.

Unlike the spectra of less treated bone with high protein, this spectrum has a very flat baseline. Later, we will look at the distortion that arises when protein is present. The protein indicator is the peak at 1450 cm^{-1} wavenumber, which shows the CH_2 scissoring mode. Amide III (C-N stretches and N-H bends) at 1250 cm^{-1} and amide I at 1660 cm^{-1} (C = O stretch) are the collagen backbone vibrations [9]. Raman measurements are usually taken as ratios because in a complex phase like bone, it is challenging to take absolute measurements [14].

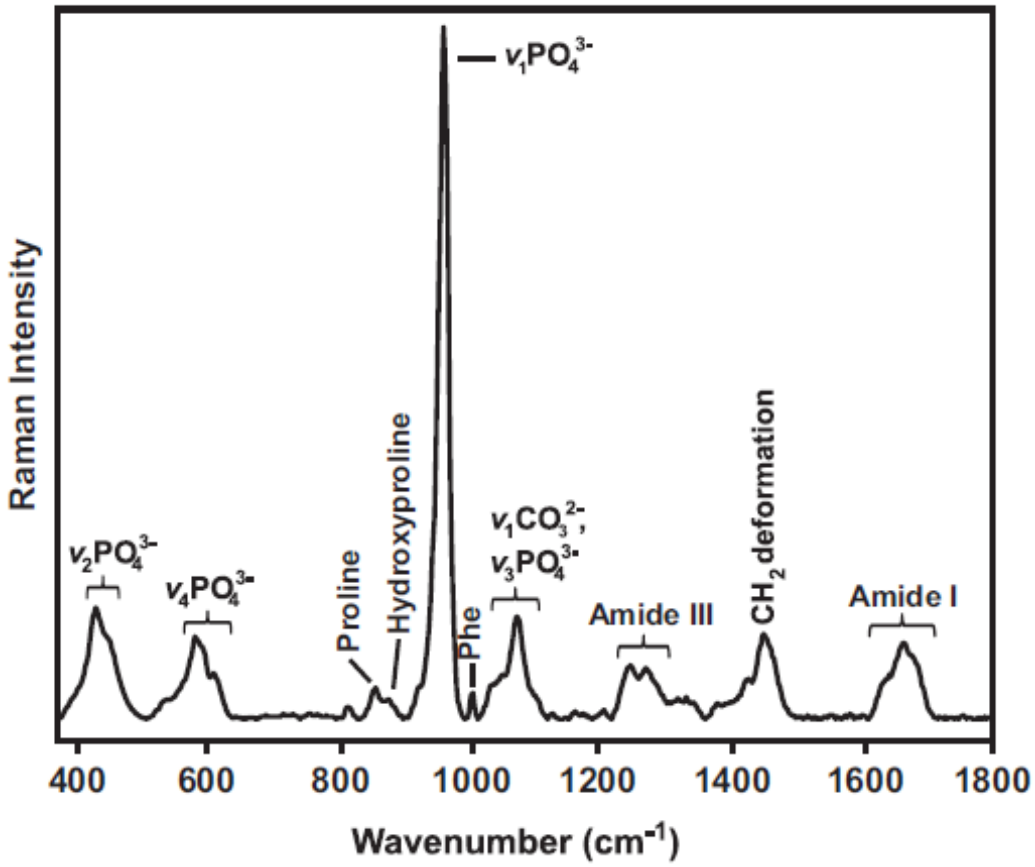

Figure 3-3 Standard Raman spectrum of bone

The four most common ratios calculated for the different measurements of the bone are (1) mineral to matrix ratio, (2) carbonate to phosphate ratio, (3) collagen-cross link ratio, and (4) crystallinity. Among all of these, the first three ratios can be calculated using the height and the area ratios of different peaks. According to one study, it has been proven that height ratio gives more accurate measurements than the area ratio [30] as it contains fewer errors when calculated from the baseline. In our research, we have focused on the mineral to matrix ratio, which was calculated using the height ratio.

The ratio of the phosphate and amide I peak gives a mineral to matrix ratio. The

phosphate peak is universally accepted as the measure of mineral. However, there are some disagreements over the amide I peak as the measure of matrix content. The competitors for the amide I peak are proline, hydroxyproline, amide III, and the CH_2 deformation peak [14]. Some studies suggest hydroxyproline peak for the measure of a matrix due to less stretching frequency and intensity compared to the amide I and the change in the secondary structure of collagen [31]. However, we have taken amide I as the measure of a matrix, and we have calculated the different ratio. This ratio defines the mineral content as proportional to ash weight [32]. The carbonate to phosphate ratio directly relates to the carbonate substitution [33] [29]. The study shows the increase in carbonate substitution, with an increase in mineral aging [34]. Table 3-1 shows general ratios used for different measurements.

Table 3-1 Important Raman Ratios

Most-Used Raman Ratios	Calculations
Mineral to matrix	(959-to-Pro, Hyp or 959-to-amide I) a measure of mineral content
Carbonate to phosphate	(1070-to-959) a measure of carbonate substitution in apatitic lattice
Crystallinity	(inverse width 959) a measure of crystal size and/or perfection
Collagen cross-link	(1685-to-1665) a measure of collagen fibril maturity

Chapter 4 Experimental Techniques and Methods

Our research majorly contains work done using Raman spectroscopy to find the mineral to matrix ratio in two different kinds of rat bone. We used SEM and EDS to get additional information. We used a Thermo Digital X-ray radiogrammetry (DXR) Raman microscope for our study. Figures 4-1 and 4-2 show the instrument and its schematic diagram, respectively. The monochromatic laser is used for characterization as seen in Figure 4-2. The laser cleaning filter is placed right next to the laser source, and the monochromatic laser then strikes the sample, which gives back different types of signals. In the end, there is a laser blocking filter that allows Raman signals to pass and prevents other signals.

Figure 4-1 DXR Raman microscope

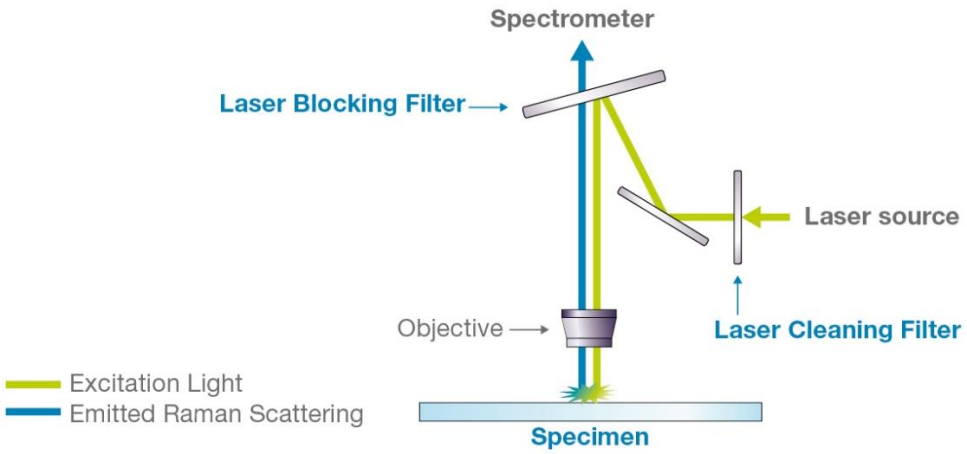

Figure 4-2 Schematic Diagram of Raman microscope

We practiced different samples such as hand gloves, cartilage, elk antlers, and mouse skin to get hands-on experience. After the completion of baseline materials, we exposed rat bones to the Raman laser. We carried out our work from two different regions of the bone: (1) the outer layer of the bone (periosteum) and (2) an edge after the longitudinal cut (cortical bone).

Figure 4-3 shows the spectrum, which is consistent with any of the clear bone positions, especially the femur and tibia. This spectrum resembles all spectra taken from the DXR Raman microscope, which are the same in wavenumber but different in intensity. Table 4-1 shows the important peak assignments. The highlighted rows show the peaks that we used as a measurement of Mn/Mx content.

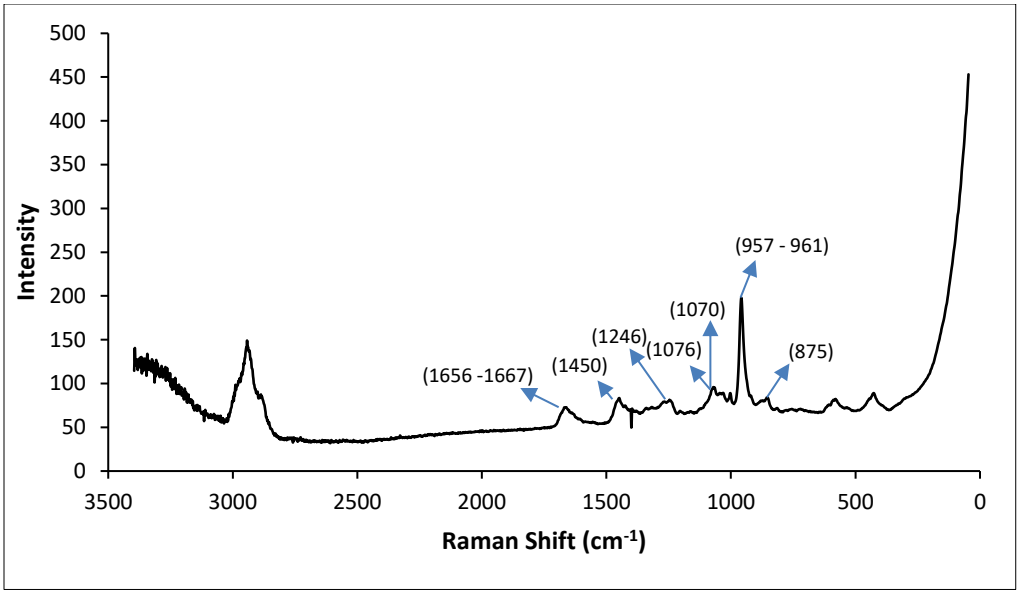

Figure 4-3 Standard Raman spectrum of rat bone from DXR Raman Microscope

Table 4-1 Important Raman Peaks from Rat Bone

Component	Wavenumber
Hydroxyproline	875 cm^{-1}
Phosphate (PO_4^{3-}) v1	957–961 cm^{-1}
Carbonate (CO_3^{2-})	1070 cm^{-1}
Phosphate (PO_4^{3-})	1076 cm^{-1}
Amide III	1246 cm^{-1}
(CH_2) deformation	1450 cm^{-1}
Amide I	1656 -1667 cm^{-1}

These spectra obtained from the DXR Raman microscope differ from the standard spectrum (Figure 3-3) in terms of wavenumber order (arrangement of wavenumber on X-axis). The standard spectrum shown in Figure 3-3 starts with the lowest wavenumber and ends with the highest wavenumber (ascending order), whereas

the spectra obtained from the DXR Raman microscope start with the highest wavenumbers and end the lowest wavenumbers (descending order). Due to this mismatch, the spectrum appears to be different at first sight, but the peaks are obtained at similar wavenumbers.

The reason for the baseline not being parallel to the x-axis is the interference of fluorescence. According to research, fluorescence comes from the matrix portion of the bone [35]. The deproteination of bone is one of the methods to get rid of the fluorescence in the spectra. But this process removes the organic phase from the bone, which consists of matrix, and our work is focused on the mineral to matrix ratio of the bone. Hence this method was not useful for our research. The standard Raman spectrum of bone does not show fluorescence. It was difficult for us to remove the fluorescence entirely. Another method to reduce the fluorescence is photobleaching the sample. Photobleaching is the process of making the molecules in such a way that they never fluoresce again. To avoid the fluorescence, we used photobleaching time for 2.5 minutes, but we could not suppress the fluorescence entirely. Excessive photobleaching may lead to the removal of organic phase entirely, which was not desirable for our study. Thus, with some expense of organic phase, we subtracted fluorescence as much as possible. We used Origin Lab software for baseline subtraction method to get the correct height of the different peaks. Figure 4-4a shows the image of baseline subtraction method.

After subtracting baseline, we have an exact measure of the height of different peaks. As shown in Figure 4-4a, we selected 25 points to subtract the baseline using the Origin Lab software. As shown in Figure 4-4b, after subtracting the baseline, we get a spectrum that is very similar to the standard one, showing less noise and with less effect of the fluorescence.

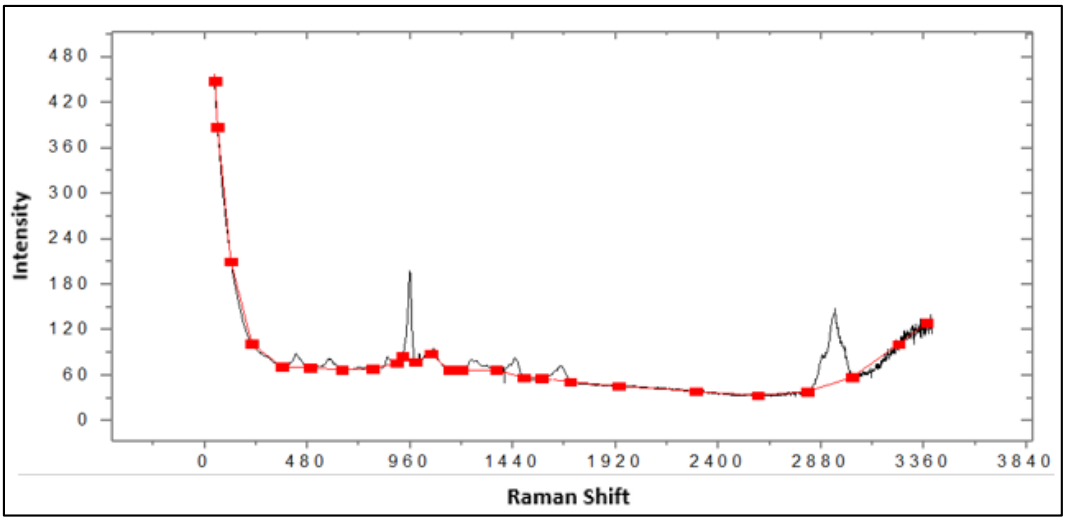

Figure 4-4 (a) Baseline subtraction method using Origin Lab for each rat bone spectrum

The result with some noise (Figure 4-4b) is closer to the standard spectrum. A cleaner match is obtainable if maximum possible spots are selected precisely. As shown in Figure 4-4c, the heights of peaks will be accurate enough by keeping precision in choosing correct points around the peaks that we need. That gives sufficiently accurate values of height or area, with the elimination of work to obtain clean spectra.

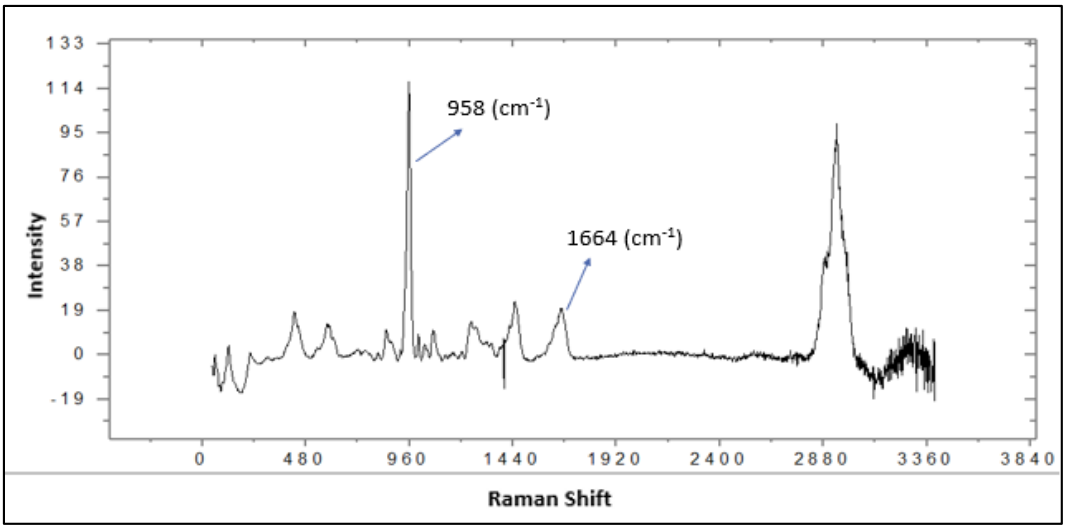

Figure 4-4 (b) Rat bone spectrum after baseline subtraction

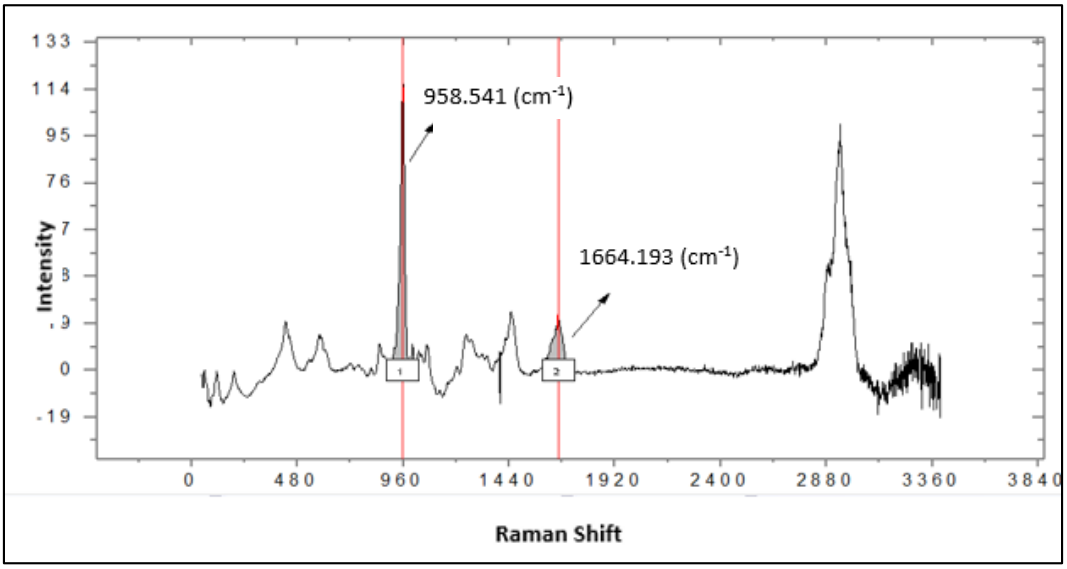

Figure 4-4 (c) Rat bone spectrum showing area under the curve

Chapter 5 Experimental Results

This chapter shows the Raman spectral data obtained from leg bones of WT, KO, and mixed HET Sprague-Dawley rats. Each spectral plot is displayed, along with a graph of the Mn/Mx ratio calculated from the spectra using the methodology explained previously in chapter 3 and 4.

As summarized in section 4, we first gathered data of the bones with the outer membrane in place (the periosteum—see section 2.2 and Figure 4-3). We measured bone slices to obtain spectra of the cortical bone without the periosteum. We wanted to determine whether useful Raman spectra could be obtained with minimal and nondestructive sample preparation; if the periosteum did not introduce significant interference in the spectral components for mineral and matrix, it would allow the possibility for the eventual use of Raman laser microscope spectroscopy with fiber optics in live animal studies and potentially in medicine for diagnostics and to guide surgery.

Also, as samples were limited, we followed a very conservative path in analyzing the bones so that in each step we could preserve the material for further analysis. The bones came from a group of carefully bred genetic rats.

For the periosteum measurements, spectra were obtained from dissected bones of WT, KO, and heterogeneous (HET). Because no significant differences were found between WT and HET spectra, the cortical measurements for sliced bone were taken from WT and KO only.

5.1 Intact Bones with Periosteum

For the periosteum study, we had a set of 18 samples containing WT, KO, and HET. HET is a mixture of WT and KO. WT is a healthy mouse whereas KO is deficient in the Follistatin-like 5 ($FSTL5^{-/-}$) gene. All the 18 samples were from the hind legs (HL) of

female rats. The following table shows the data of the samples. The sample IDs here are given according to their birth dates in table 5-1.

Table 5-1 Sample list and their type for periosteum femur

Sample ID	Bone Type
1-23-17 1F HL	HET
1-23-17 3F HL	HET
1-23-17 5F HL	WT
1-23-17 7F HL	HET
1-23-17 9F HL	KO
1-23-17 11F HL	KO
3-10-17 1F HL	WT
3-10-17 3F HL	KO
3-10-17 5F HL	HET
3-10-17 7F HL	WT
3-10-17 8F HL	HET
3-10-17 9F HL	HET
3-10-17 10F HL	HET
3-10-17 11F HL	WT
3-10-17 12F HL	WT
3-13-17 2F HL	WT
3-13-17 4F HL	WT
3-13-17 6F HL	HET

These bones are divided into three groups according to age. We started collecting the spectra from the outer shell of the bone as shown in Figure 5-1. We took eight spectra from each sample on five different positions as shown in the Figure below.

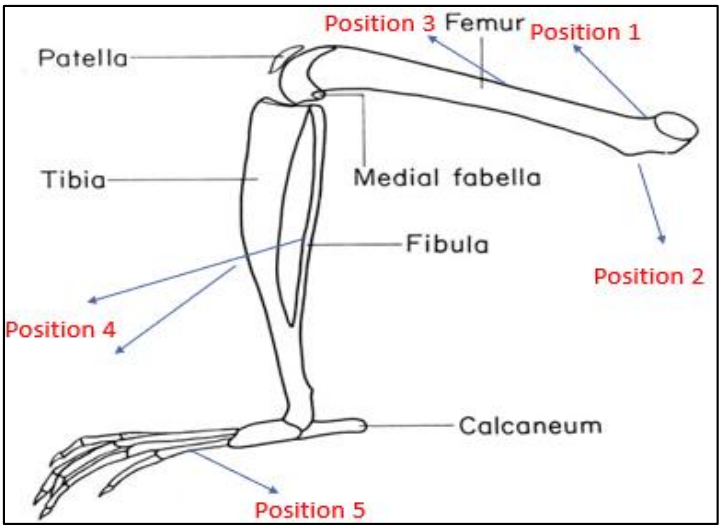

Figure 5-1 Different portions on the hind leg of the rat

We have used the height of the phosphate peak to the height of the amide I peak as a measurement of the Mn/Mx ratio. The following sections will show the different spectra taken from the periosteum portion of the bone and the cortical bone. Each page contains two Figures, which are (a) Raman spectra collected from the different positions of the bone and (b) bar charts showing the Mn/Mx ratio for the same positions. The comparison of average Mn/Mx ratio of WT/HET/KO is shown. The positions from where the spectra were obtained from periosteum portions are shown in Figure 5-2.

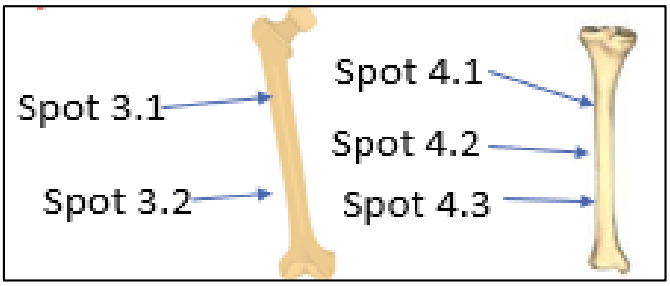

Figure 5-2 Positions of femur and tibia

5.1.1 Raman Spectra and Mn/Mx Ratio of the Periosteum Femur

This section contains the spectra obtained from the periosteum femur of a single sample but from different positions (Figure 5-2), along with a graph showing the Mn/Mx ratio for those positions for all WT/KO/HET rat bones.

(1) Wild-type samples

Here, Figure 5-3a shows the detectable Raman signals from the bone. The difference in the Mn/Mx ratio (Figure 5-3b) between two positions shows the heterogeneity present in the bone structure.

(i) 1-23-17 5F HL femur

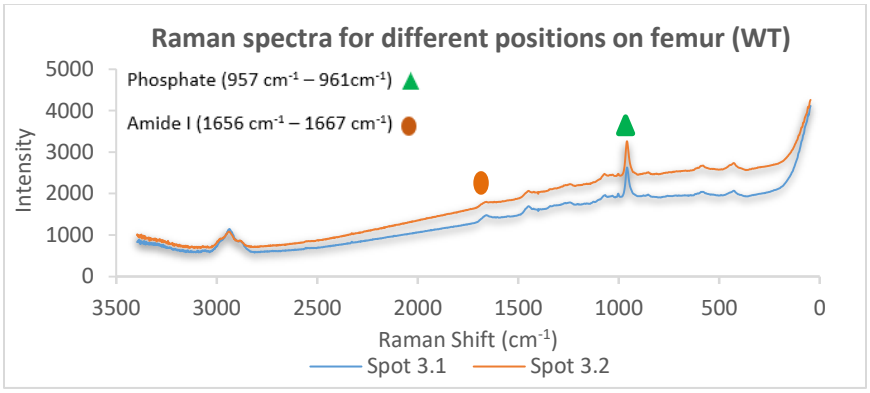

(a)

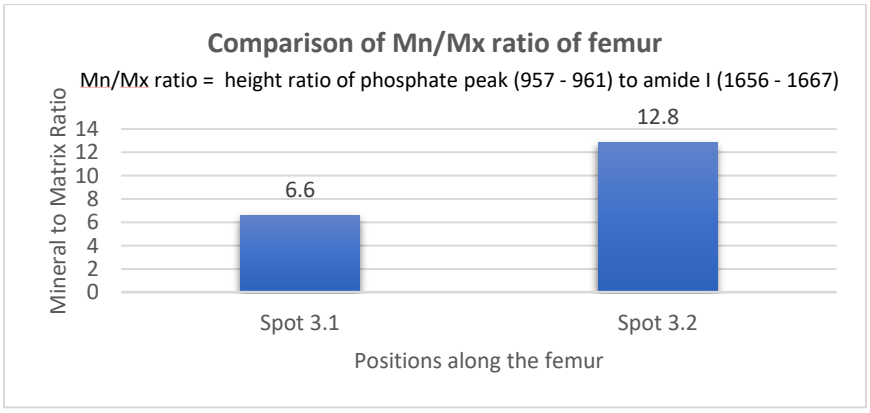

(b)

Figure 5-3 Periosteum femur—1-23-17 5F HL (WT) (a) Raman spectra (b) Mn/Mx ratio

(ii) 3-10-17 1F HL Femur

Figure 5-4a shows the consistency in the Raman signal for two different positions. The phosphate and amide I peak of both the spots overlap each other with less variation in the intensity. However, the comparison of the ratio indicates a noticeable difference in minerals and matrix content between two points as shown in Figure 5-4b.

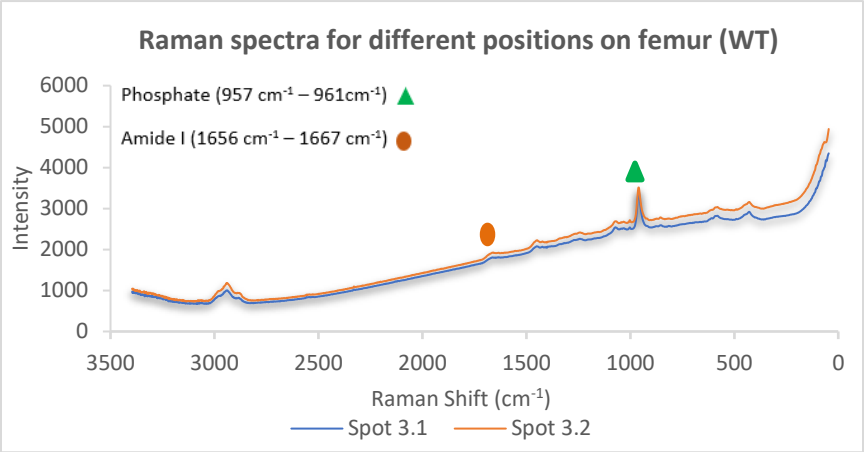

(a)

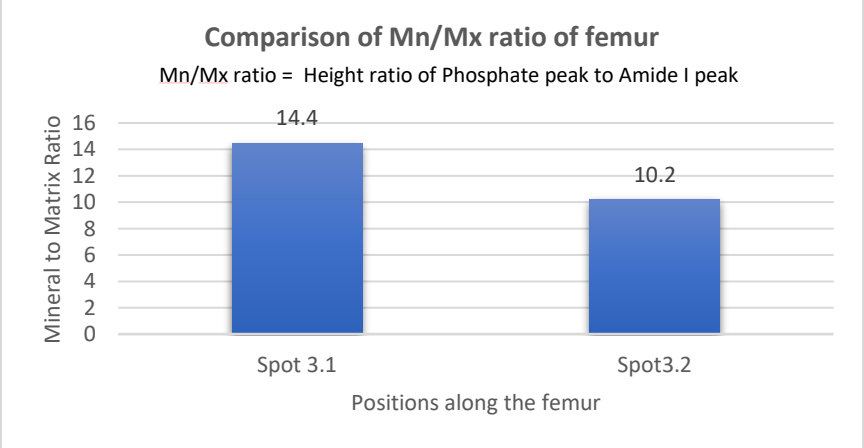

(b)

Figure 5-4 Periosteum femur—3-10-17 1F 5F HL (WT) (a) Raman spectra (b) Mn/Mx ratio

(iii) 3-10-17 7F HL

From Figure 5-5a, it is observed that spot 3.2 gives a clearer and more intense peak of amide I as well as a less intense peak of phosphate than spot 1. As a result, there is a huge difference in the Mn/Mx ratio of the bone as show in Figure 5-5b, which emphasizes the inhomogeneous structure of the bone.

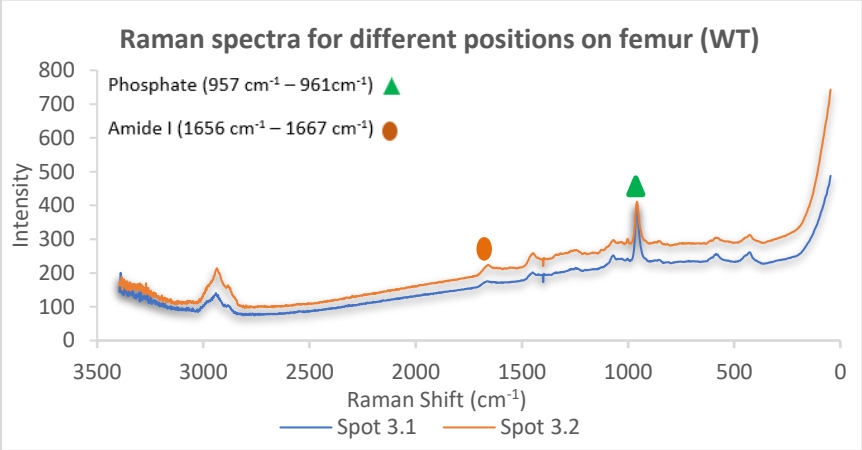

(a)

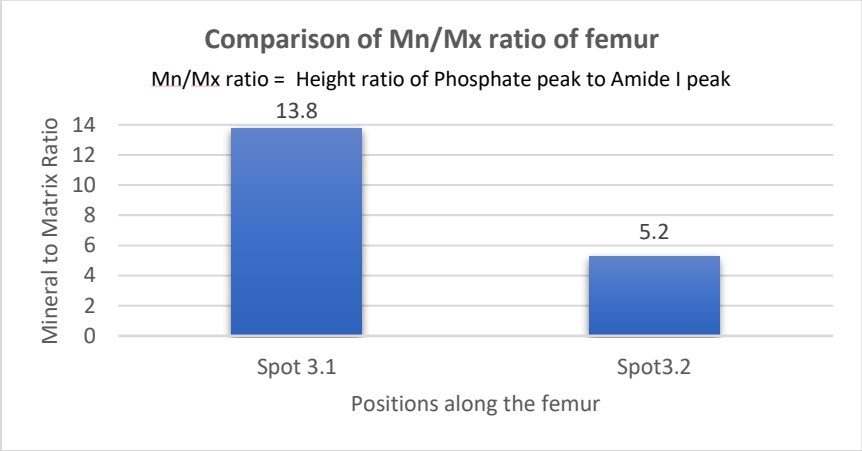

(b)

Figure 5-5 Periosteum femur—3-10-17 7F HL (WT) (a) Raman spectra (b) Mn/Mx ratio

(iv) 3-10-17 11F HL

Figure 5-6a indicates that spot 3.2 has lower intensity for all the peaks than spot 3.1. As shown in Figure 5-6b, the ratio of both positions is higher than the standard ratio found in the literature for different rat bones. These ratios indicate an excessive amount of minerals present in the bone.

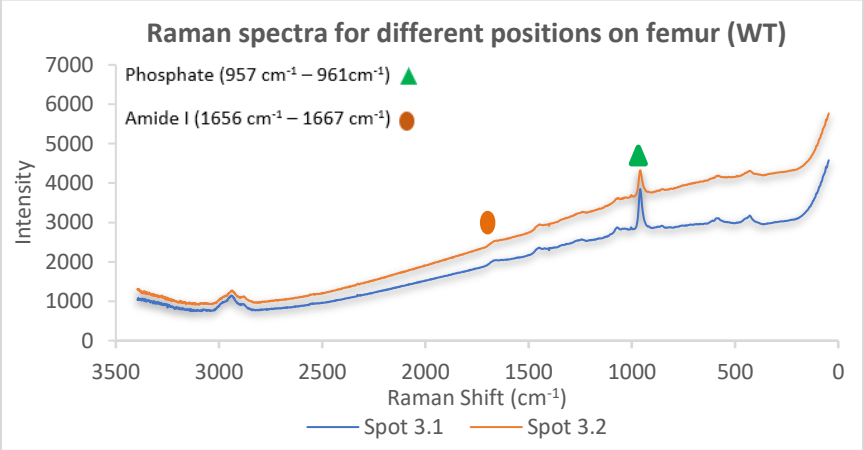

(a)

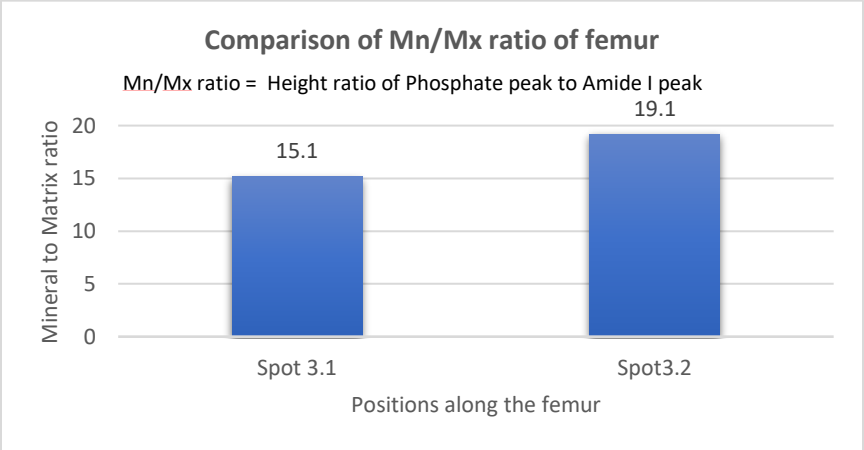

(b)

Figure 5-6 Periosteum femur—3-10-17 11F HL (WT) (a) Raman spectra (b) Mn/Mx ratio

(v) 3-10-17 12F HL

Here, direct observation of the spectra (Figure 5-7a) does not give an idea about the ratios. The obtained amide I peak shows less height for both positions. The Origin Lab software gives a better explanation of those peaks. Here, the height of phosphate peaks for both positions is less compared to the previous results, which is the reason for lower Mn/Mx ratio as shown in Figure 5-7b.

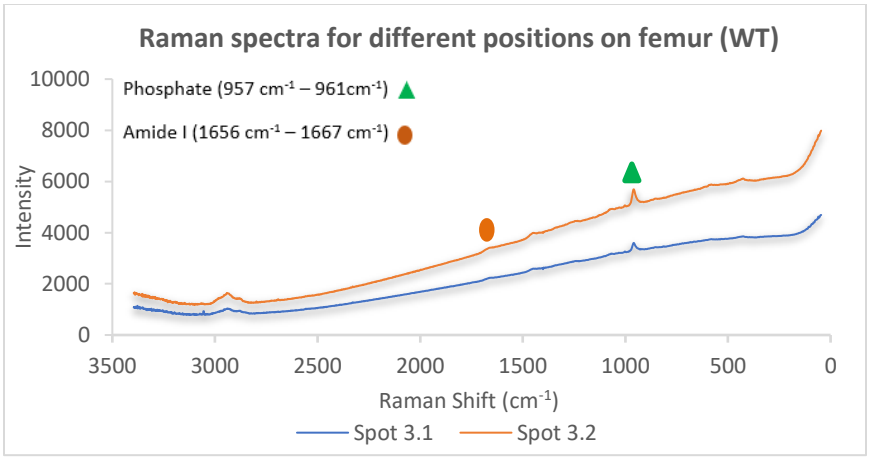

(a)

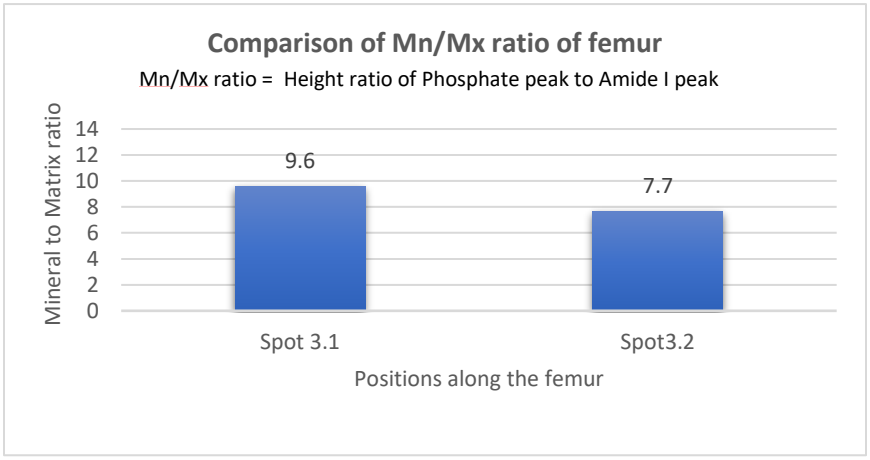

(b)

Figure 5-7 Periosteum femur—3-10-17 12F HL (WT) (a) Raman spectra (b) Mn/Mx ratio

(vi) 3-13-17 2F HL

For this sample, the Raman spectra for both the positions are very clear and give distinguishable peaks as shown in Figure 5-8a. The Mn/Mx ratio proves the consistency of chemical compositions for the different positions of the bone as shown in Figure 5-8b.

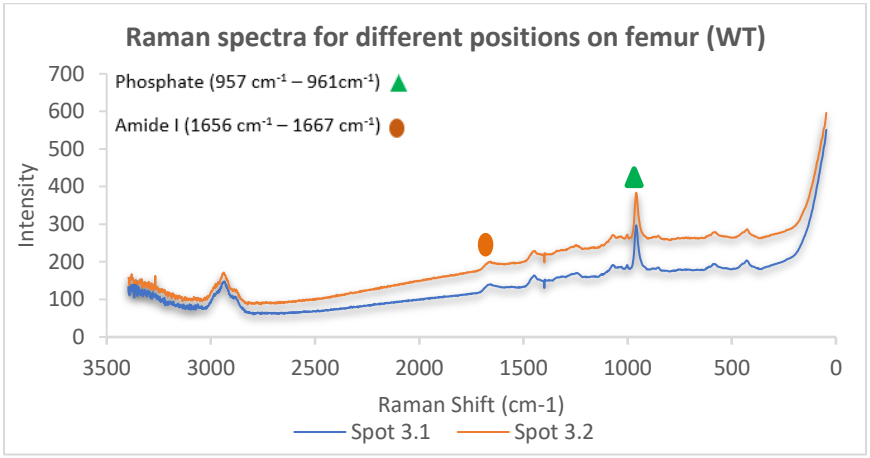

(a)

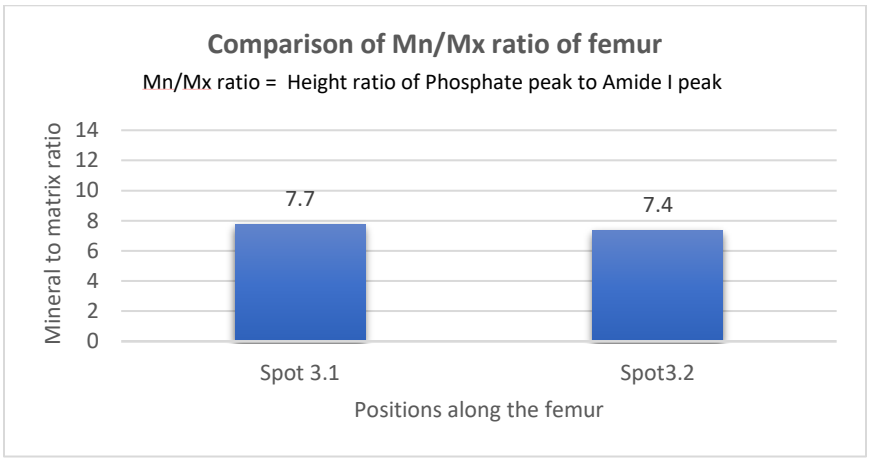

(b)

Figure 5-8 Periosteum femur—3-13-17 2F HL (WT) (a) Raman spectra (b) Mn/Mx ratio

(vii) 3-13-17 4F HL

As shown in Figure 5-9a, as in the previous sample, the spectra are clear. There is a high variance between the Mn/Mx ratio of two different positions as shown in Figure 5-9b. Position 3.1 shows much higher ratio than the standard range where all ratios fall.

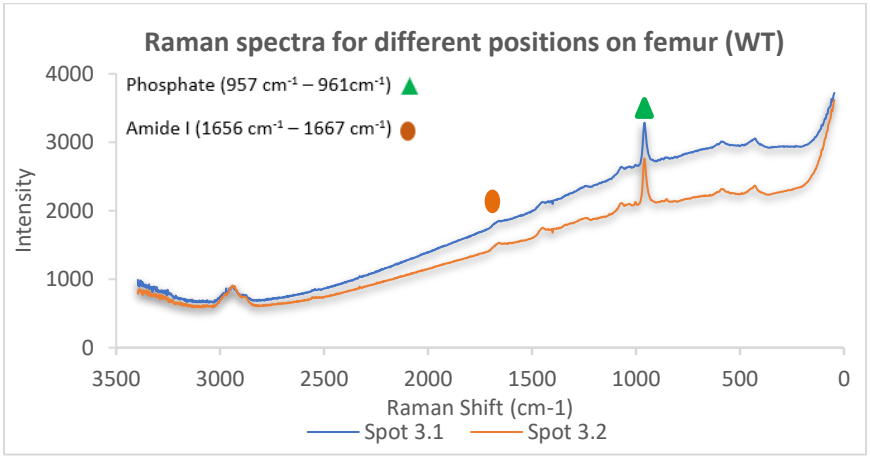

(a)

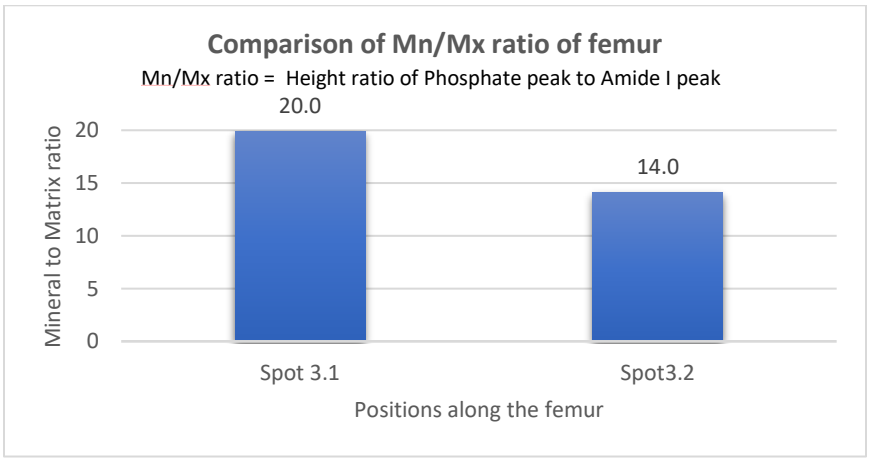

(b)

Figure 5-9 Periosteum femur—3-13-17 4F HL (WT) (a) Raman spectra (b) Mn/Mx ratio

(2) Knockout sample

(i)1-23-17 9F HL

As shown in Figure 5-10a, the lower presence of minerals at spot 3.2 does not give a good and intense peak of phosphate, which results in a very low Mn/Mx ratio as shown in Figure 5-10b. Both spots show the spectra having distinguishable peaks as shown in Figure 5-10b.

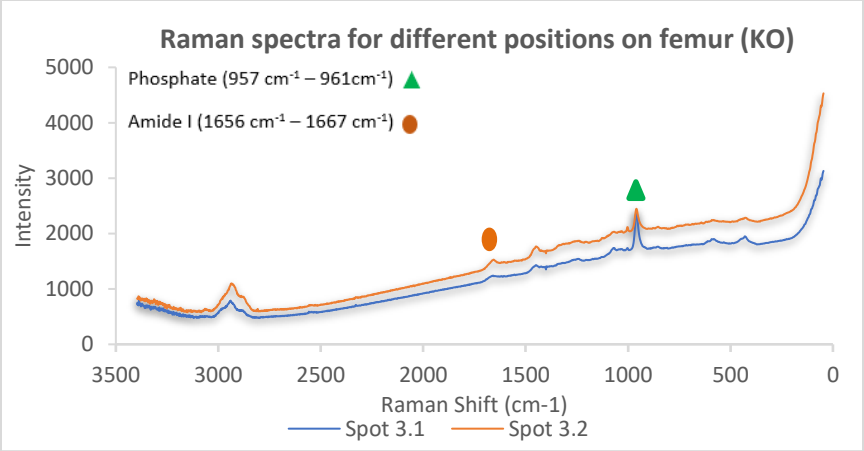

(a)

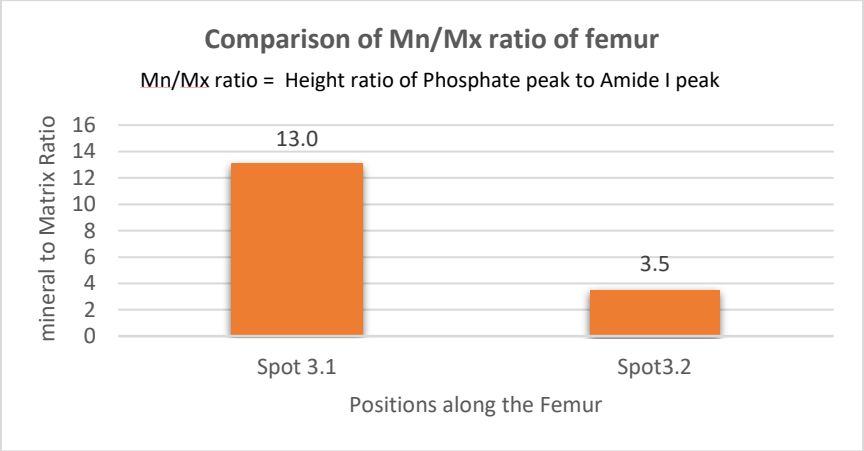

(b)

Figure 5-10 Periosteum femur—1-23-17 9F HL (KO) (a) Raman spectra (b) Mn/Mx ratio

(ii) 1-23-17 11F HL

Compared to the previous sample results, the amide I peak has a higher height as shown in Figure 5-11a, which leads to samples with lower Mn/Mx ratios as shown in Figure 5-11b. For both positions, the Mn/Mx ratio is less. In every spectrum, there is a down peak seen at the wavenumber around 1400 cm^{-1}, which does not represent any vibrational mode or any other molecular information. It was an instrument error that we observed for every spectrum run.

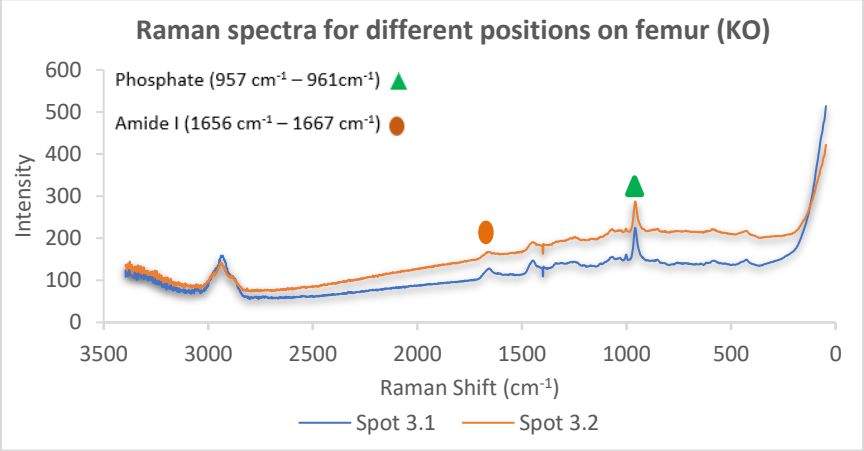

(a)

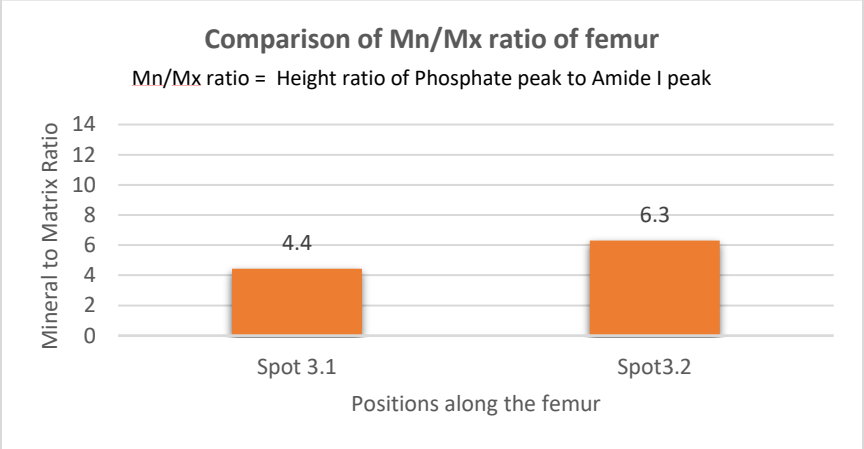

(b)

Figure 5-11 Periosteum femur—1-23-17 11F HL (KO) (a) Raman spectra (b) Mn/Mx ratio

(3) Heterogeneous Samples

(i) 1-23-17 1F HL Femur

As shown in Figure 5-12a, both positions give clean and consistent spectra, which results in an ideal Mn/Mx ratio for both the positions as shown in Figure 5-12b. The literature shows the ratio in the same range.

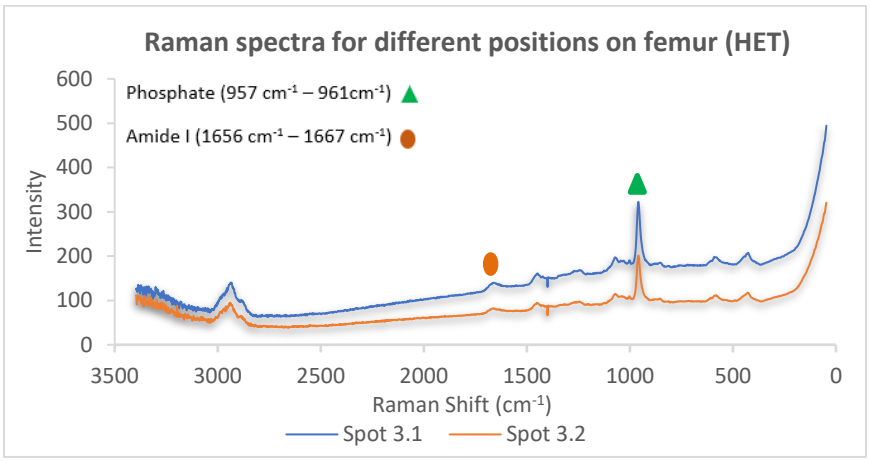

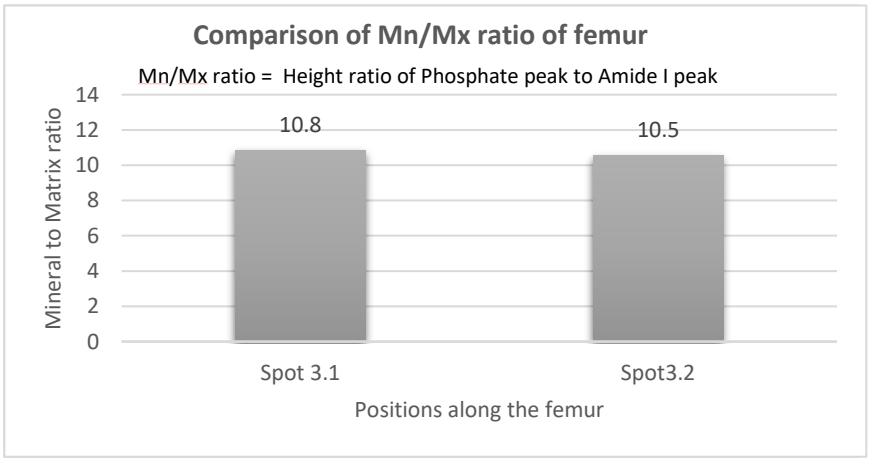

(b)

Figure 5-12 Periosteum femur—1-23-17 1F HL (HET) (a) Raman spectra (b) Mn/Mx ratio

(ii) 1-23-17 3F HL Femur

As shown in Figure 5-13a, the baseline of the spectra is much more distorted compared to the other samples due to the high fluorescence. The spectra show a clear peak for the phosphate, but the height of amide I is low, which in turn results in the higher ratio shown in Figure 5-13b.

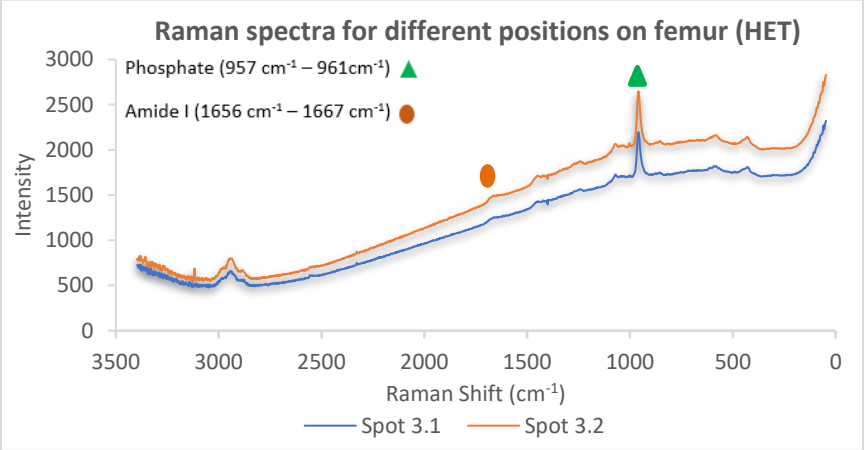

(a)

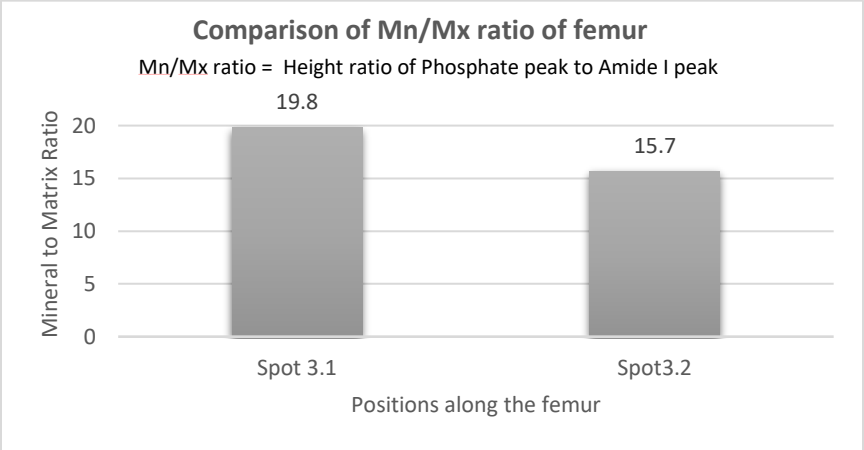

(b)

Figure 5-13 Periosteum femur—1-23-17 3F HL (HET) (a) Raman spectra (b) Mn/Mx ratio

.

(iii) 1-23-17 7F HL Femur

Because the baselines of both the spectra overlap, the amide I peak for spot 3.2 as shown in Figure 5-14a is not clear. There is not much difference found in the Mn/Mx ratio between these two points as represented in the Figure 5-14b.

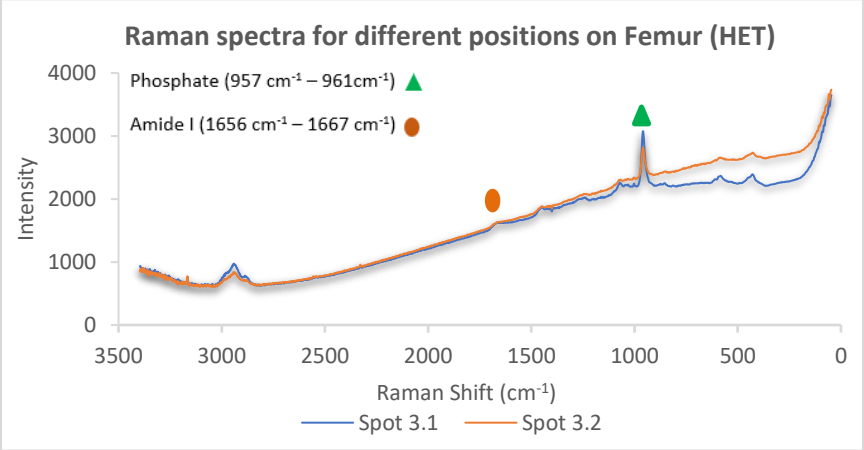

(a)

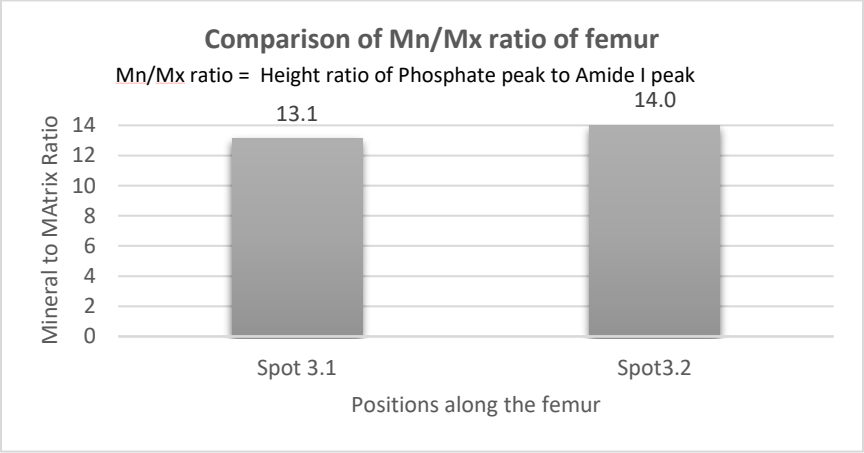

(b)

Figure 5-14 Periosteum femur—1-23-17 7F HL (HET) (a) Raman spectra (b) Mn/Mx ratio

(iv) 3-10-17 5F HL

Compared to the spectra in other samples, these spectra do not show clear peaks for phosphate and amide I as shown in Figure 5-15a. Spot 3.1 shows a higher ratio whereas spot 3.2 shows a ratio in range as shown in Figure 5-15b.

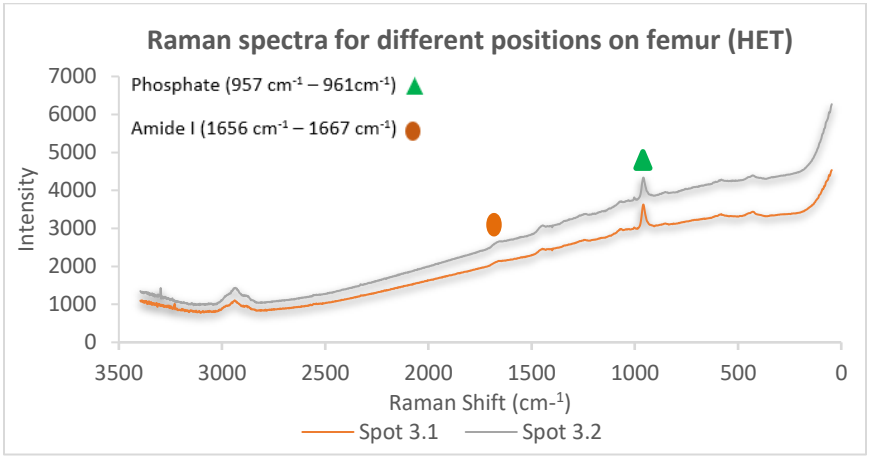

(a)

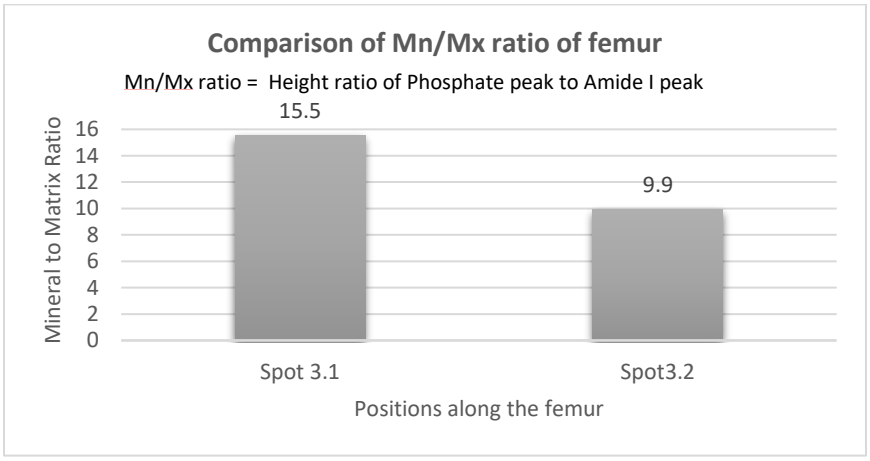

(b)

Figure 5-15 Periosteum femur—3-10-17 5F HL (HET) (a) Raman spectra (b) Mn/Mx ratio

(v) 3-10-17 8F HL

Figure 5-16a shows that the spectra from both positions are reproducible. However, because of a low peak height of amide I on spot 3.1, the ratio is higher than on spot 3.2 as shown in Figure 5-16b.

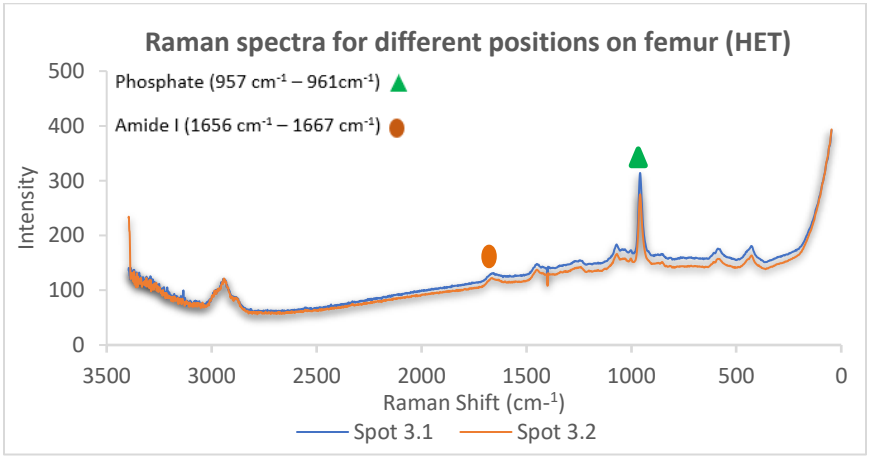

(a)

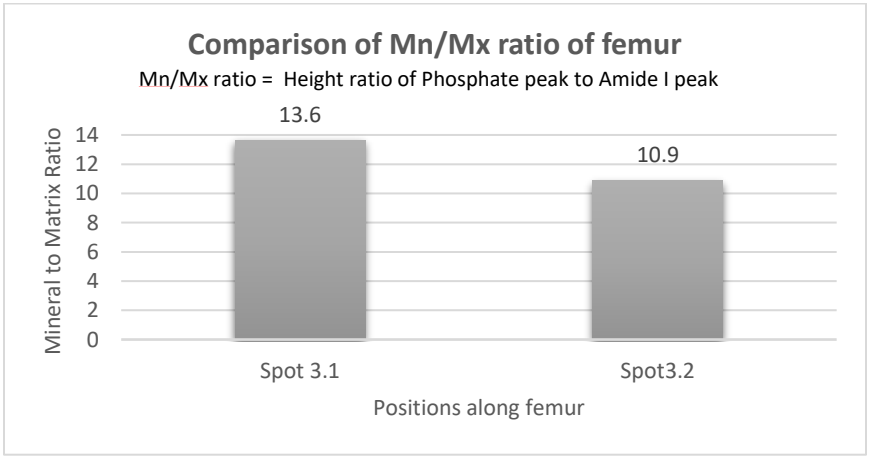

(b)

Figure 5-16 Periosteum femur—3-10-17 8F HL (HET) (a) Raman spectra (b) Mn/Mx ratio

(vi) 3-10-17 9F HL

Like the previous sample, this sample also shows spectra similar to each other for both positions (as shown in Figure 5-17a). However, Figure 5-17b shows a difference in the Mn/Mx ratio.

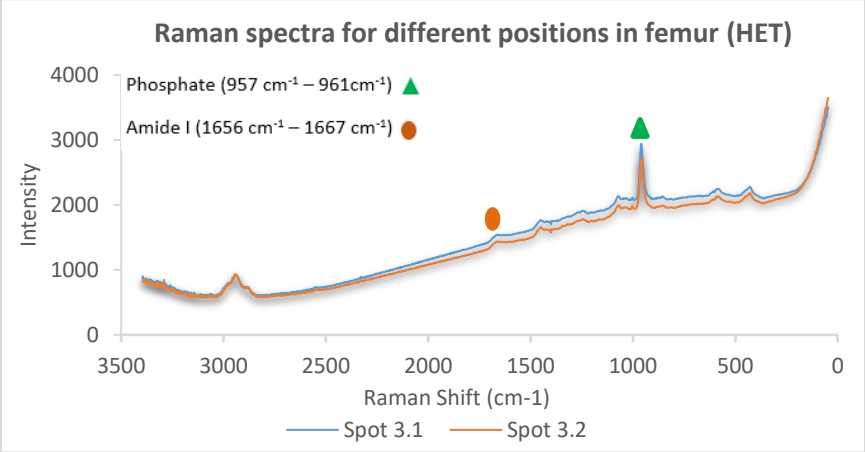

(a)

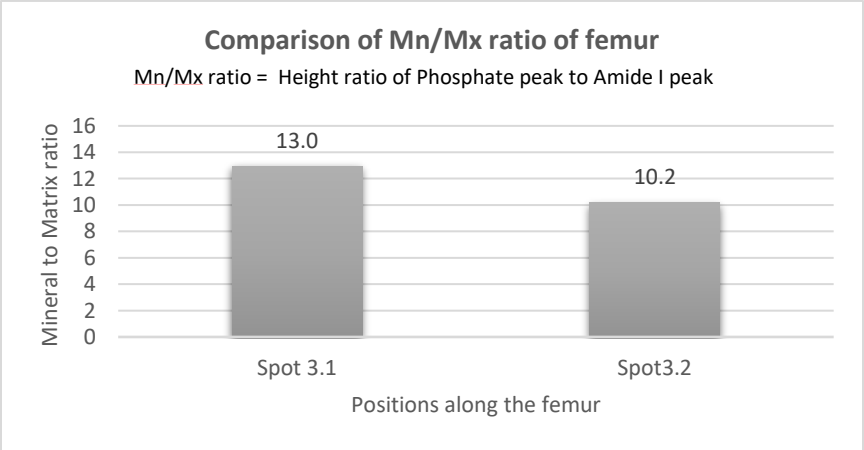

(b)

Figure 5-17 Periosteum femur—3-10-17 9F HL (HET) (a) Raman spectra (b) Mn/Mx ratio

.

(vii) 3-10-17 10F HL

Figure 5-18a indicates that spot 3.2 shows a higher fluorescence compared to spot 3.1. But both the spectra show clear signals for all the peaks. Spot 3.1 shows a higher Mn/Mx ratio than spot 3.1 (Figure 5-18b).

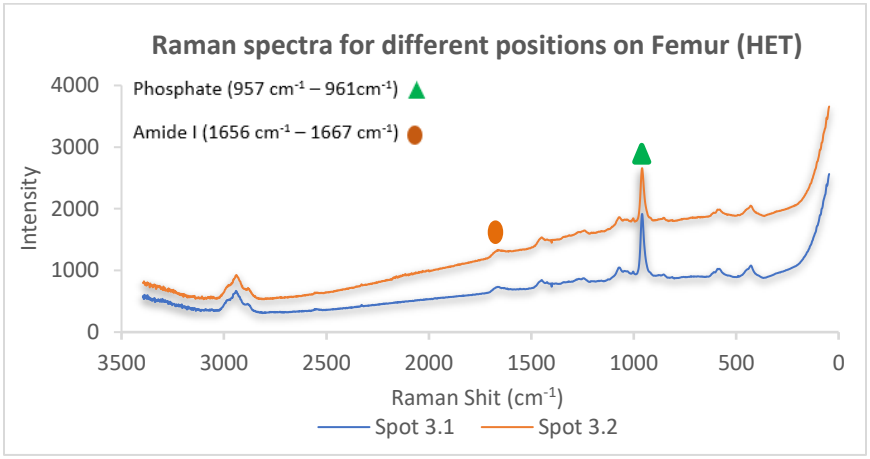

(a)

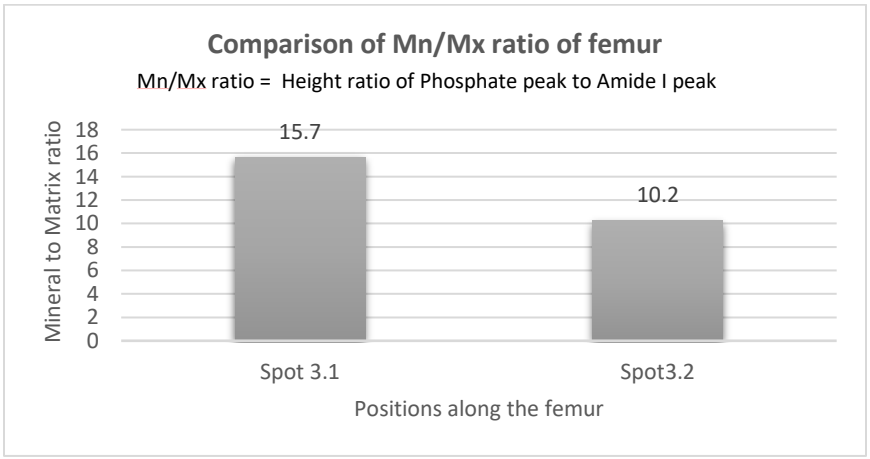

(b)

Figure 5-18 Periosteum femur—3-10-17 10F HL (HET) (a) Raman spectra (b) Mn/Mx ratio

(viii) 3-13-17 6F HL

Here, Figure 5-19a shows that both the positions do not show a clear peak for amide I. Figure 5-19b shows a large difference in the Mn/Mx ratios of the both positions.

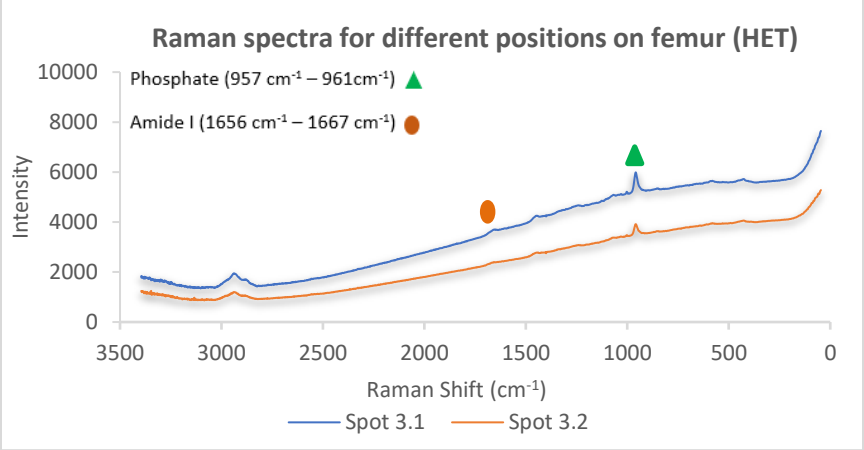

(a)

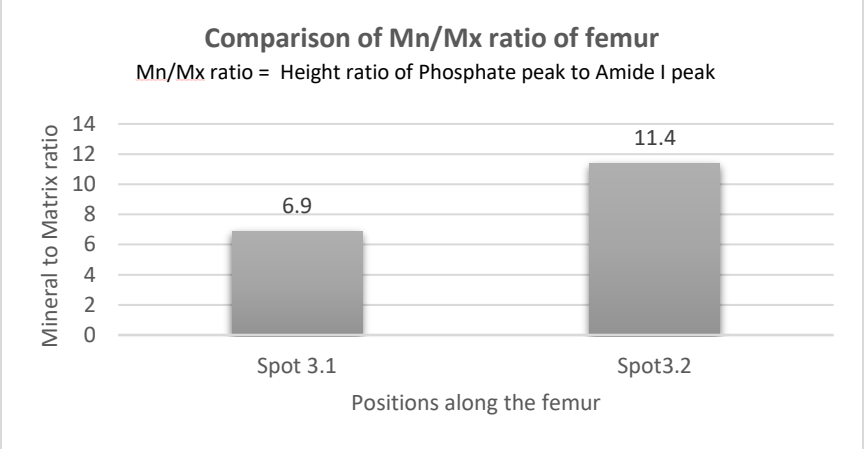

(b)

Figure 5-19 Periosteum femur—3-13-17 6F HL (HET) (a) Raman spectra (b) Mn/Mx ratio

5.1.2 Results and Discussion of Periosteum Femur

As we had multiple rat samples to analyze, we started comparing those by finding averages according to their genotype to see the overall difference. We used the lens of 10X magnification in the Raman, where the laser spot size covers a length of 3.1 µm. At this spot size, each reading gives a very small portion of the heterogeneous surface morphology of bone, so we cannot know whether the laser is focusing on mineral-rich areas or matrix-rich areas. That is the reason it is difficult to rely on just one spectrum from the particular spot. To average out all would be a way to compensate for variation in morphology. Figure 5-20 represents the average of Mn/Mx ratios of periosteum femur from all samples. Spots 3.1 and 3.2 show much higher average ratio in WT than in KO. These results are different from the hypothesis we made earlier. HET samples present an even higher average Mn/Mx ratio than in WT. It is difficult to predict the dependency of the average results of femur as we only had three samples of knockout compared to seven WT and eight HET.

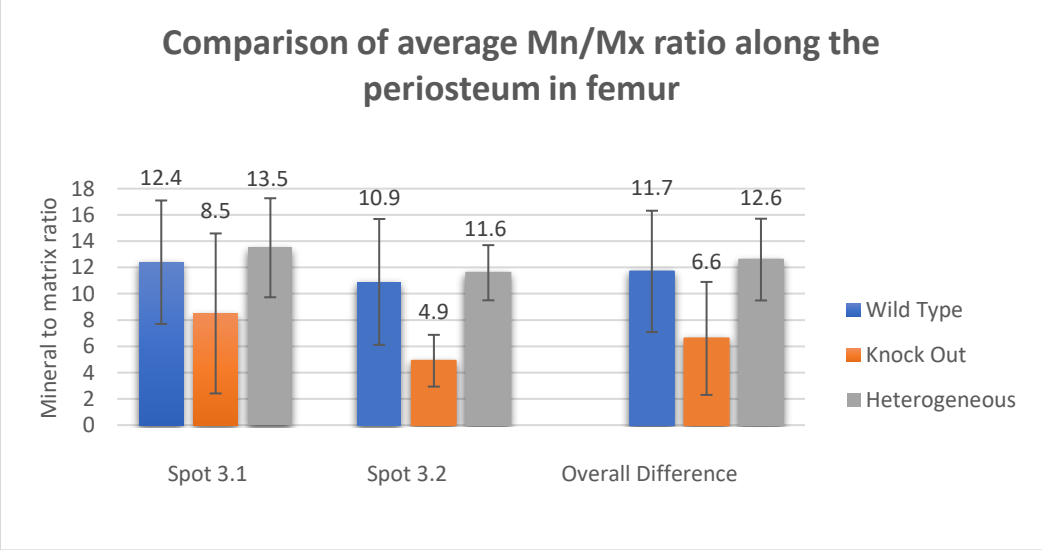

Figure 5-20 Average Mn/Mx ratio from periosteum femur for all samples

5.1.3 Raman Spectra and Ratio of Periosteum Tibia

This section contains the spectra obtained from a periosteum tibia of a single sample but different positions (Figure 5-2), along with the graph showing a Mn/Mx ratio for those positions for all WT/KO/HET rat bones.

(1) Wild-type samples

(i) 1-23-17 5F HL

As shown in the Figure 5-21a, all three positions show very clear signals for all peaks. However, like every other spectrum, they also show fluorescence. Figure 5-21b indicates that there is no high variation in Mn/Mx ratio among all the spots.

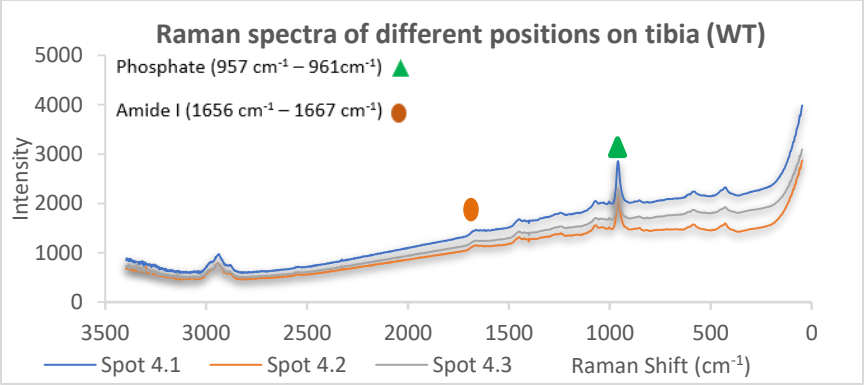

(a)

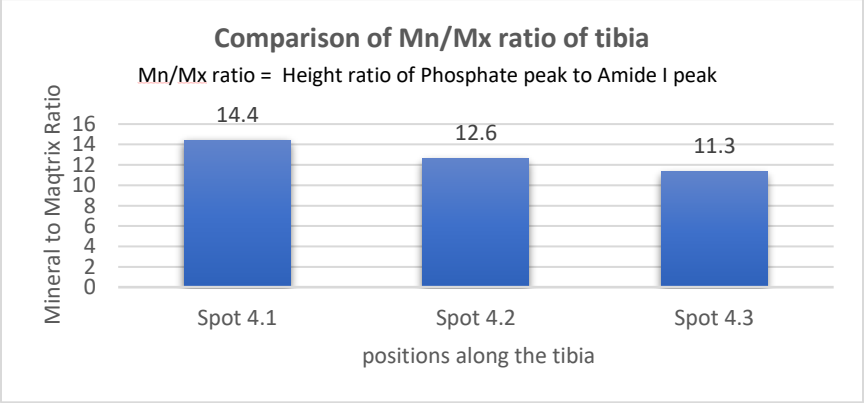

(b)

Figure 5-21 Periosteum tibia—1-23-17 5F HL (WT) (a) Raman spectra (b) Mn/Mx ratio

(ii) 3-10-17 1F HL

Figure 5-22 shows the consistent spectra obtained from different positions. The bar chart shows an increase in the Mn/Mx ratio from the top to bottom ends of the tibia. However, compared to spot 4.1 and spot 4.2, spot 4.3 shows a higher Mn/Mx ratio (Figure 5-22b).

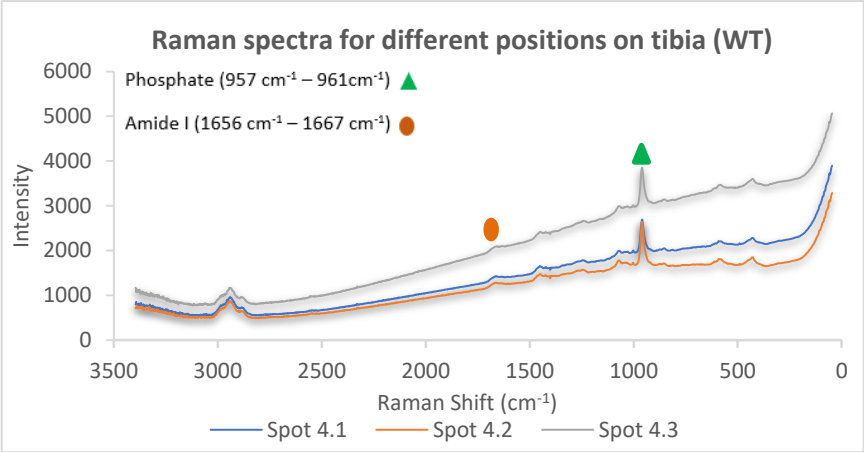

(a)

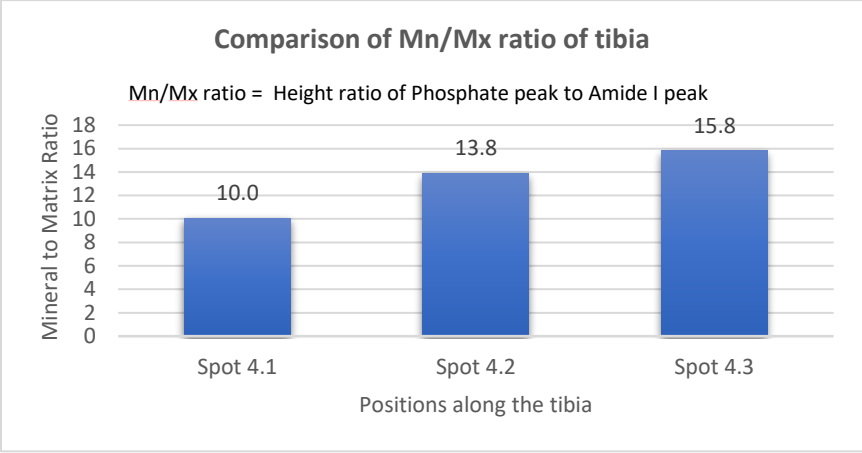

(b)

Figure 5-22 Periosteum tibia—3-10-17 1F HL (WT) (a) Raman spectra (b) Mn/Mx ratio

(iii) 3-10-17 7F HL

Figures 5-23a and 5-23b indicate the consistency of minerals and matrix composition for all positions of the tibia for this particular sample. However, the intensity of the peaks is low compared to the other samples.

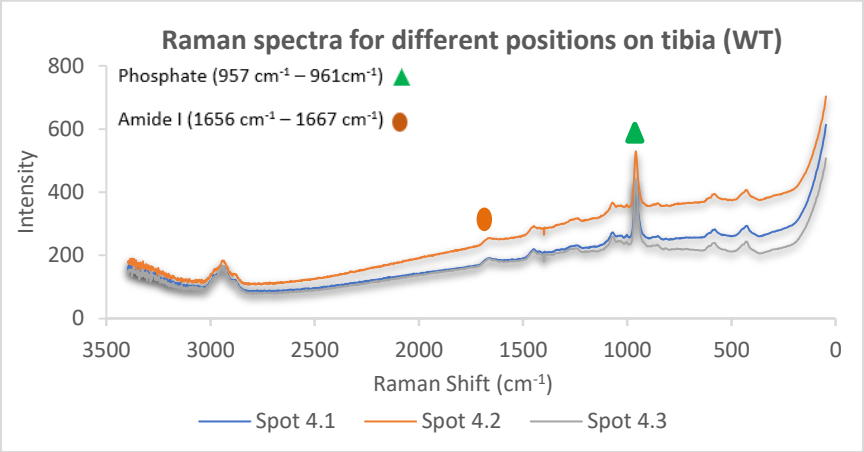

(a)

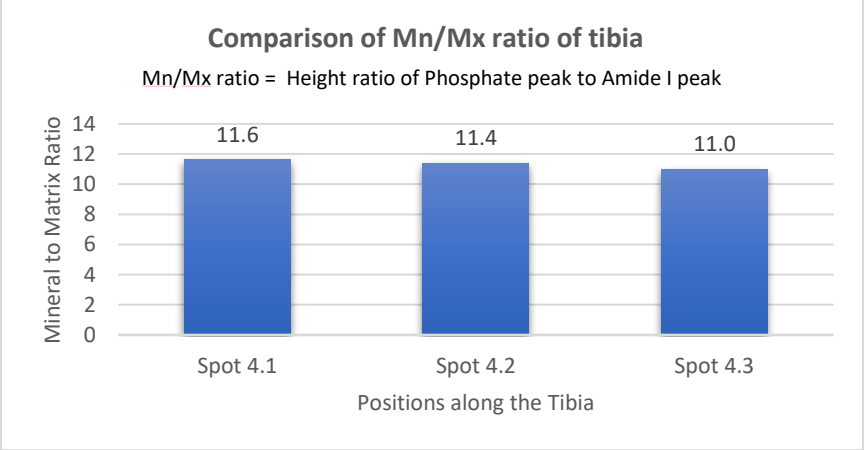

(b)

Figure 5-23 Periosteum tibia 3-10-17 7F HL (WT) (a) Raman spectra (b) Mn/Mx ratio

(iv) 3-10-17 11F HL

Figure 5-24a shows consistency in the spectra for all the positions, but as spot 4.1 shows a higher Mn/Mx ratio than the other two spots (Figure 5-24b), the amount of minerals and matrix is not evenly distributed in the sample.

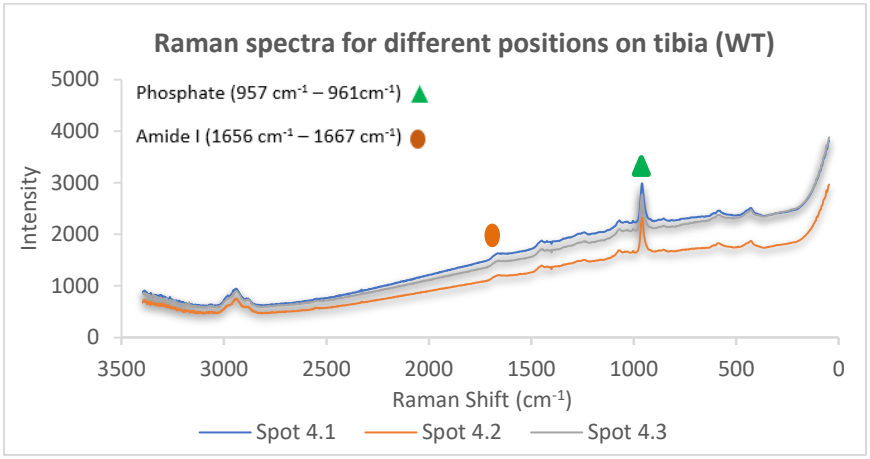

(a)

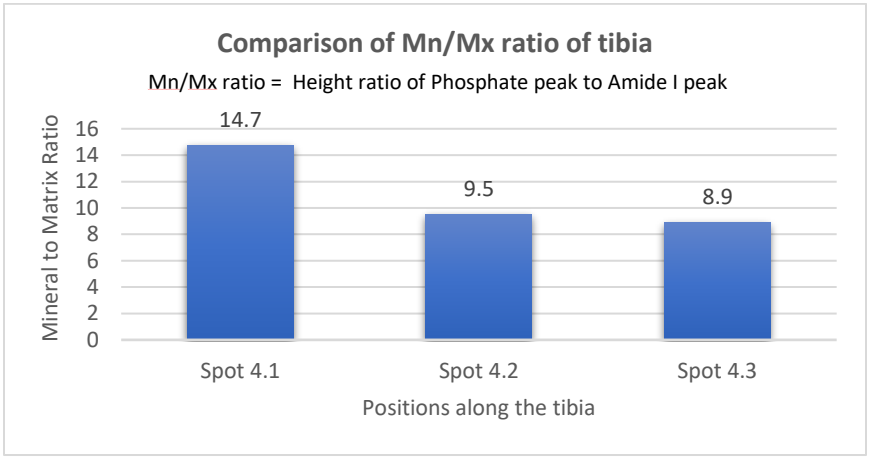

(b)

Figure 5-24 Periosteum tibia—3-10-17 11F HL (WT) (a) Raman spectra (b) Mn/Mx ratio

(v) 3-10-17 12F HL

Figure 5-25a shows overlapping spectra for all the positions. However, the ratio drastically drops for the positions from top to bottom as show in Figure 5-25b.

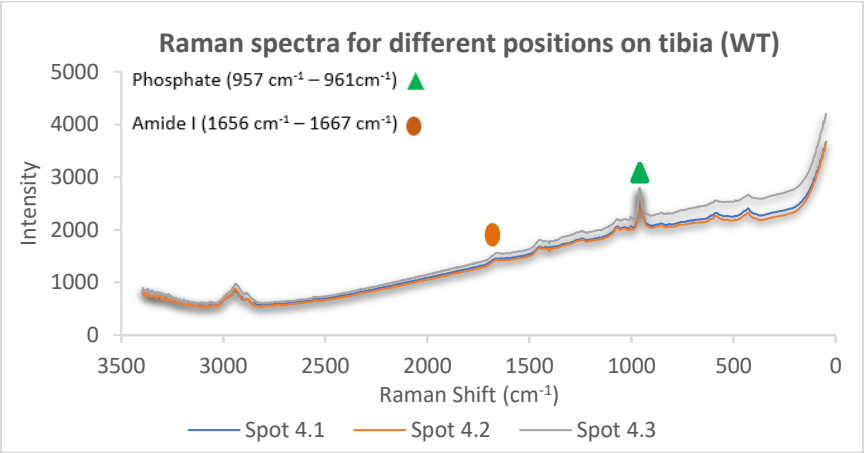

(a)

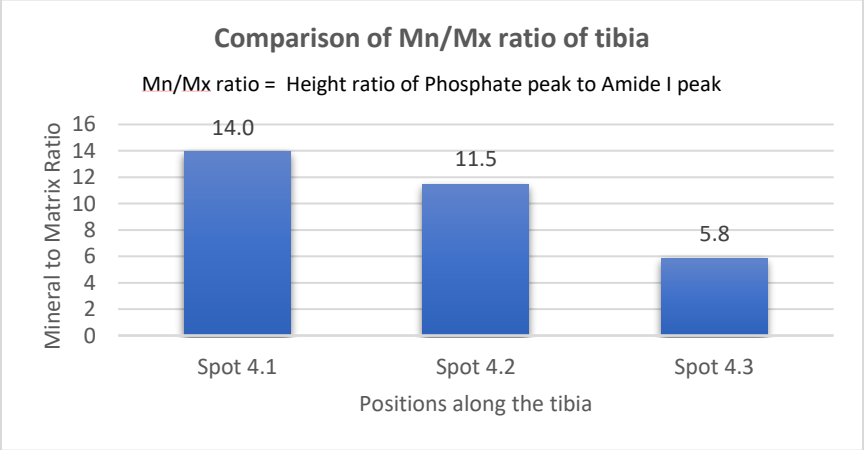

(b)

Figure 5-25 Periosteum tibia—3-10-17 12F HL (WT) (a) Raman spectra (b) Mn/Mx ratio

(vi) 3-13-17 2F HL

Spots 4.1 and 4.2 show the clear spectra as shown in the Figure 5-26a. However, spot 4.3 does not give a regular spectrum. Both phosphate and amide peaks are observed in the Origin. However, due to an excessive amount of matrix phase, the Mn/Mx ratio is very low as shown in the Figure 5-26b.

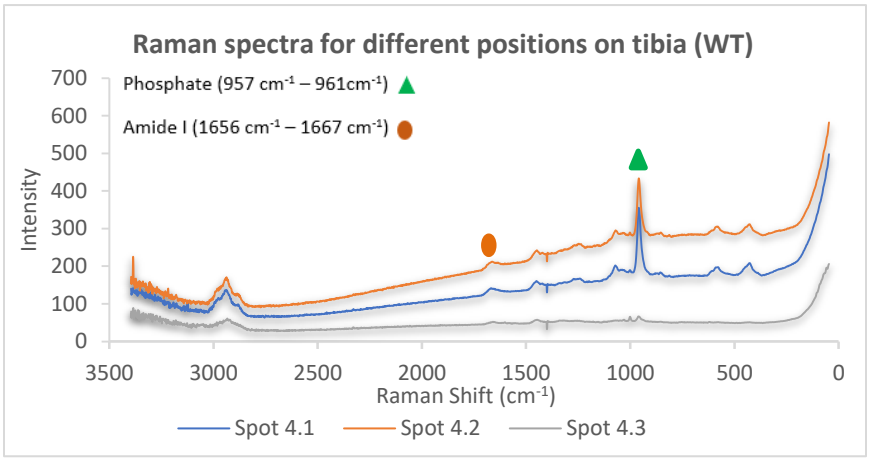

(a)

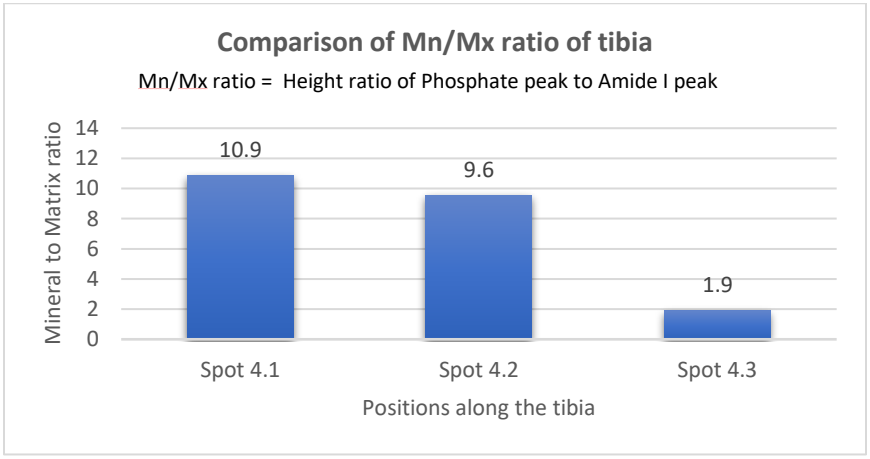

(b)

Figure 5-26 Periosteum tibia—3-13-17 2F HL (WT) (a) Raman spectra (b) Mn/Mx ratio

(vii) 3-13-17 4F HL

As shown in Figures 5-27a and 5-27b, overall spectra for all the positions of tibia are similar, and the Mn/Mx ratios are also similar to each other.

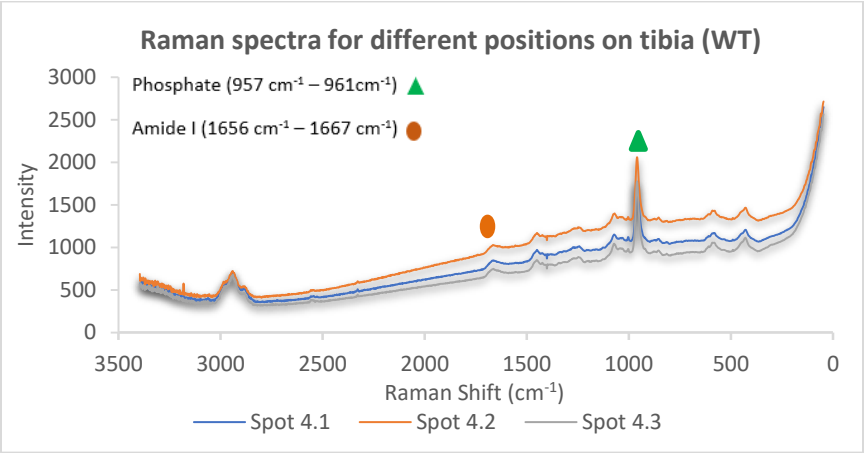

(a)

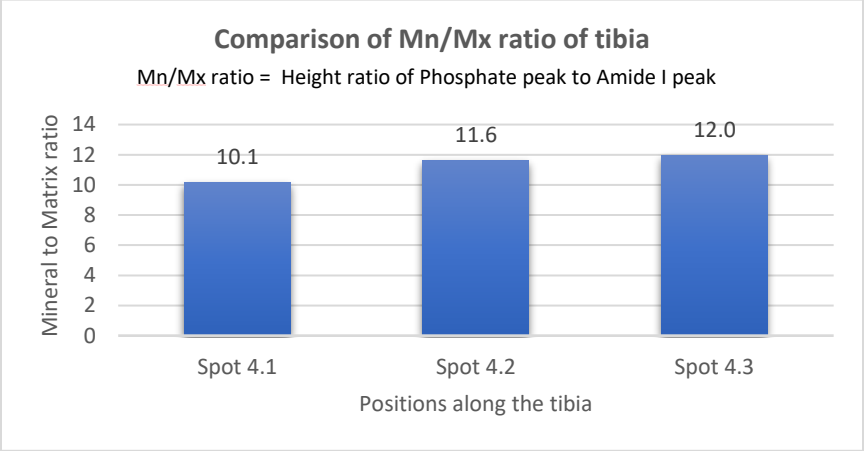

(b)

Figure 5-27 Periosteum tibia—3-13-17 4F HL (WT) (a) Raman spectra (b) Mn/Mx ratio

(2) Knockout samples:

(i) 1-23-17 9F HL

Figure 5-28a shows the overlapping spectra for positions 4.2 and 4.3. There is not much difference in Mn/Mx ratios as shown in the Figure 5-28b. However, due to a lower height of the phosphate peak for spot 4.1, the ratio is also less.

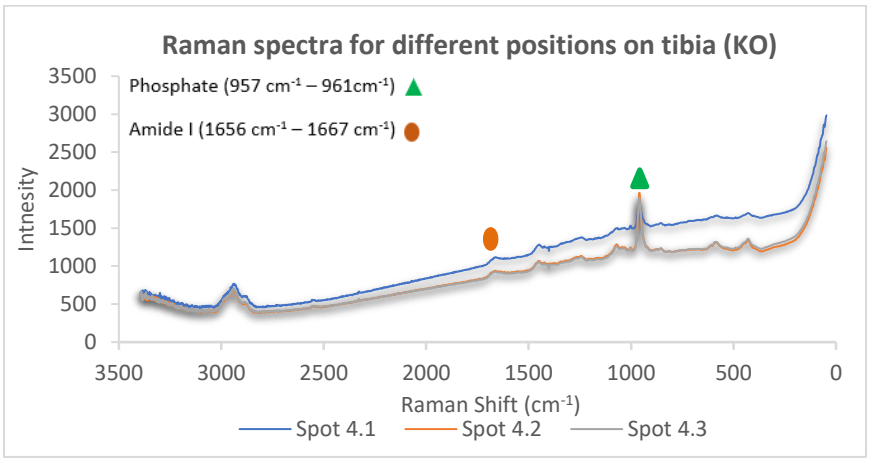

(a)

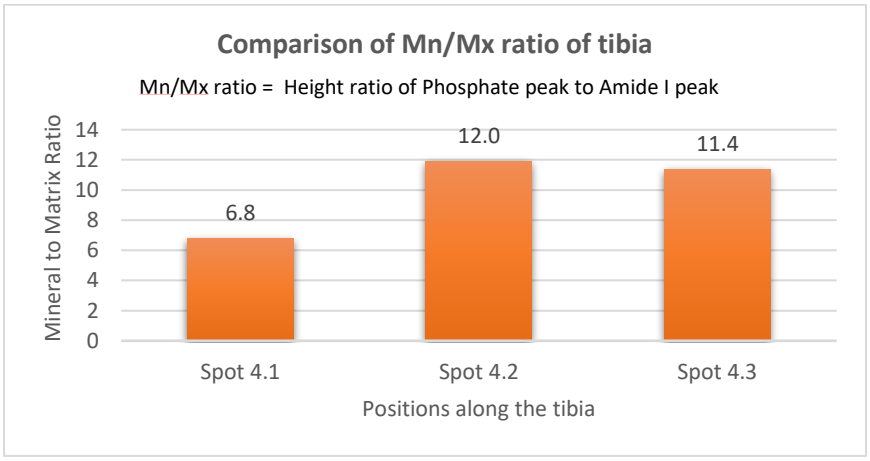

(b)

Figure 5-28 Periosteum tibia—1-23-17 9F HL (KO) (a) Raman spectra (b) Mn/Mx ratio

(ii) 1-23-17 11F HL

Figure 5-29a shows all the spectra, which are similar to each other. However, Figure 5-29b shows variation in Mn/Mx ratios on different spots.

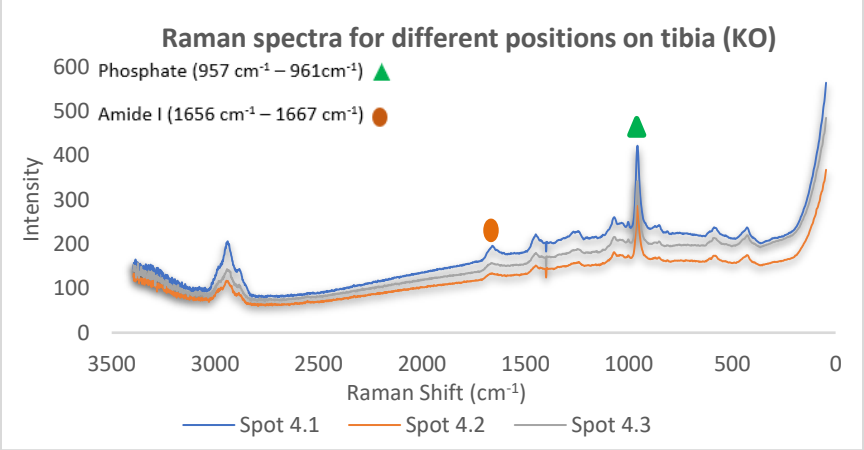

(a)

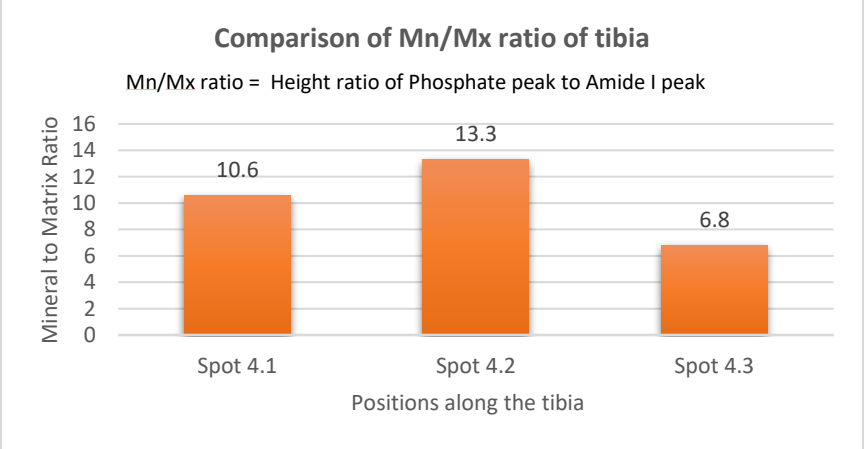

(b)

Figure 5-29 Periosteum tibia—1-23-17 11F HL (KO) (a) Raman spectra (b) Mn/Mx ratio

(iii) 3-10-17 3F HL

It is shown clearly in Figure 5-30a that there is not a good signal of phosphate for spot 4.2. Besides phosphate, it was very difficult to identify the amide I, which is the reason why no Mn/Mx ratio is presented in Figure 5-30b for spot 4.2.

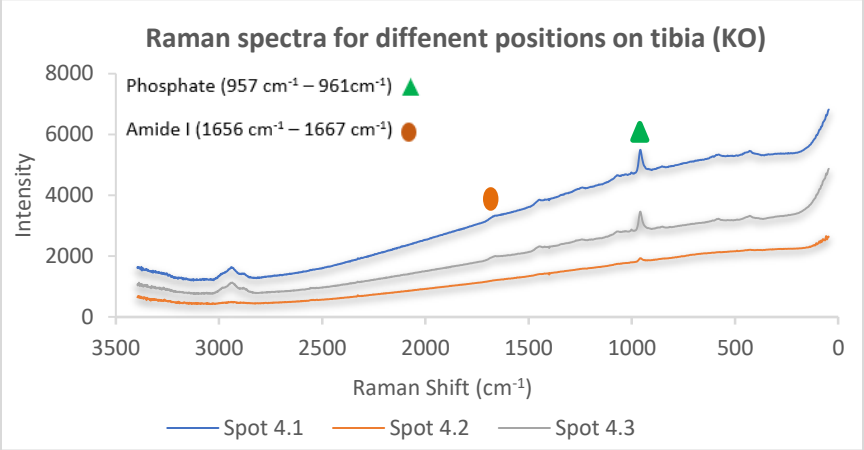

(a)

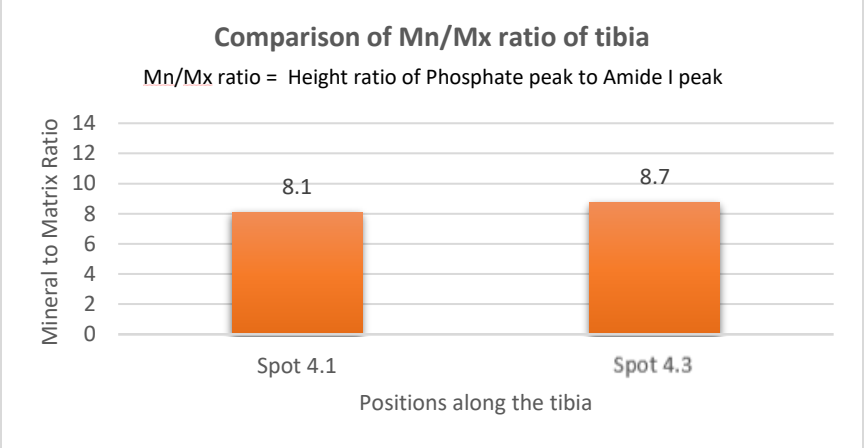

(b)

Figure 5-30 Periosteum tibia—3-10-17 3F HL (KO) (a) Raman spectra (b) Mn/Mx ratio

(3) Heterogeneous samples

(i) 1-23-17 1F HL

The overlapping spectra (Figure 5-31a) shows much variation in the Mn/Mx ratio (Figure 5-31 b).

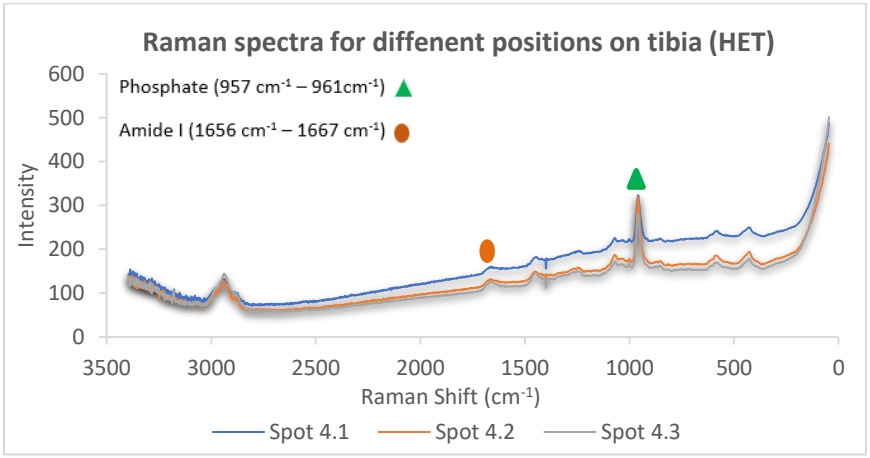

(a)

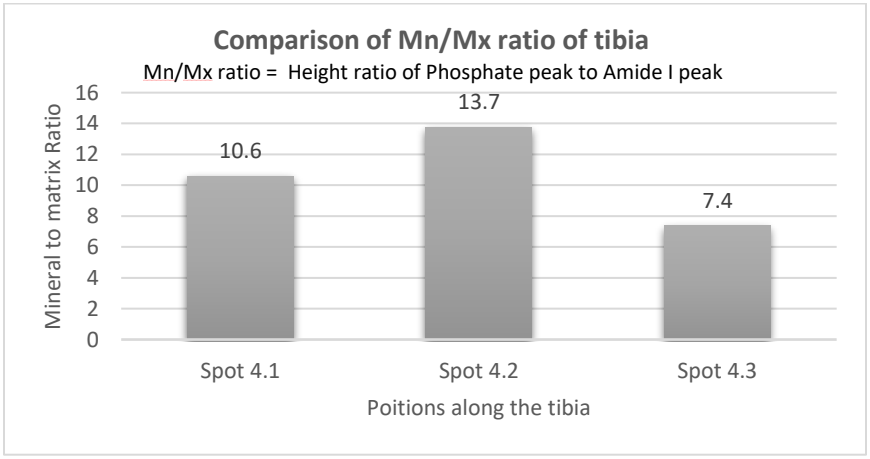

(b)

Figure 5-31 Periosteum tibia—1-23-17 1F HL (HET) (a) Raman spectra (b) Mn/Mx ratio

(ii) 1-23-17 3F HL

Here, as shown in the Figure 5-32b, the spectra do not show a noticeable difference in the Mn/Mx ratio of two different spots. However, the reason for missing the third spectrum in Figure 5-32a is the unclear area detection, which means interference of other substances is present on the periosteum portion.

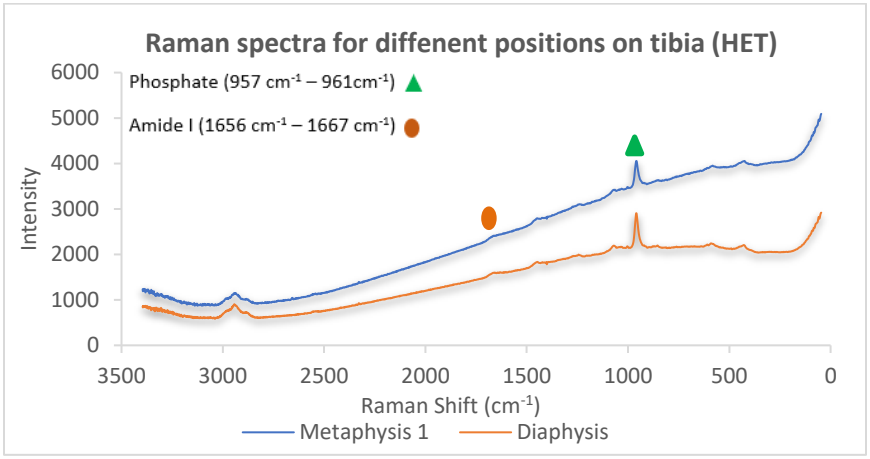

(a)

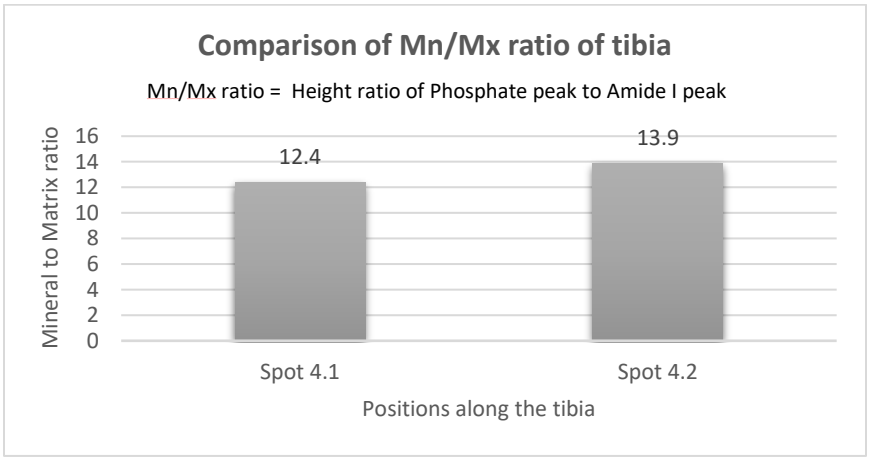

(b)

Figure 5-32 Periosteum tibia—1-23-17 3F HL (HET) (a) Raman spectra (b) Mn/Mx ratio

(iii) 1-23-17 7F HL

Spot 4.1 does not show any kind of amide I peak (a peak with very low height observable in Origin), but the other two positions give clear spectra as shown in Figure 5-33a. The sample is showing a variation in Mn/Mx ratios for all the different positions of the bone as shown in the Figure 5-33b.

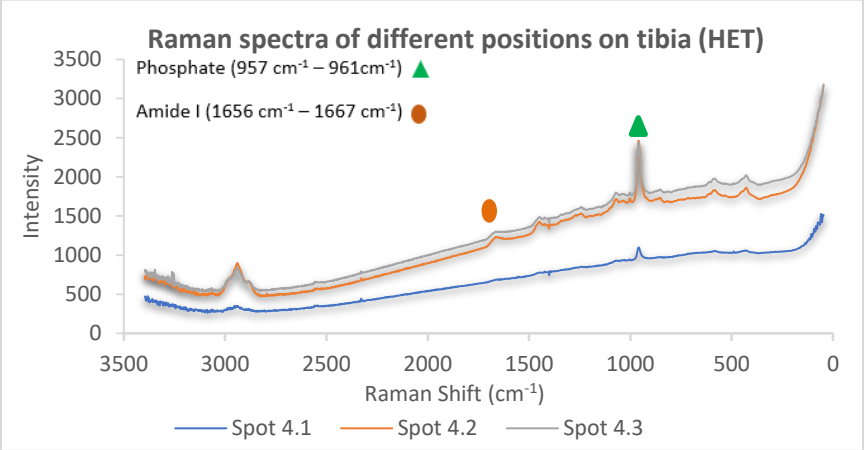

(a)

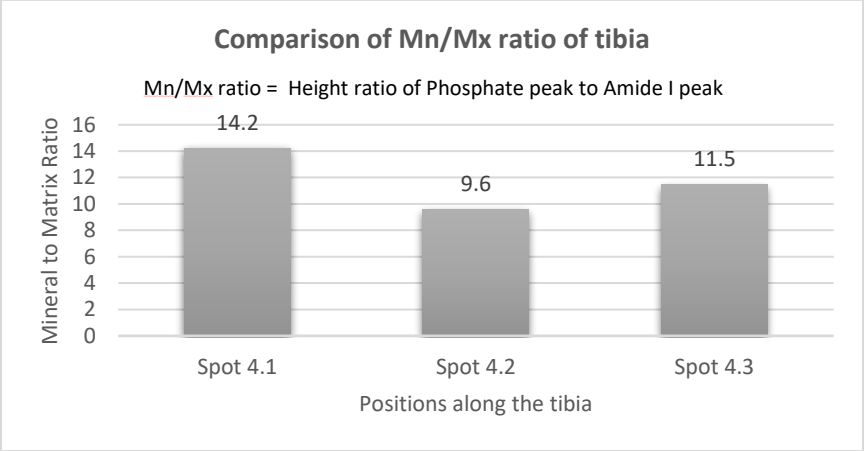

(b)

Figure 5-33 Periosteum tibia—1-23-17 7F HL (HET) (a) Raman spectra (b) Mn/Mx ratio

(iv) 3-10-17 5F HL

Likewise, Figures 5-34a and 5-34b show consistency in the spectra and in Mn/Mx ratios for different positions.

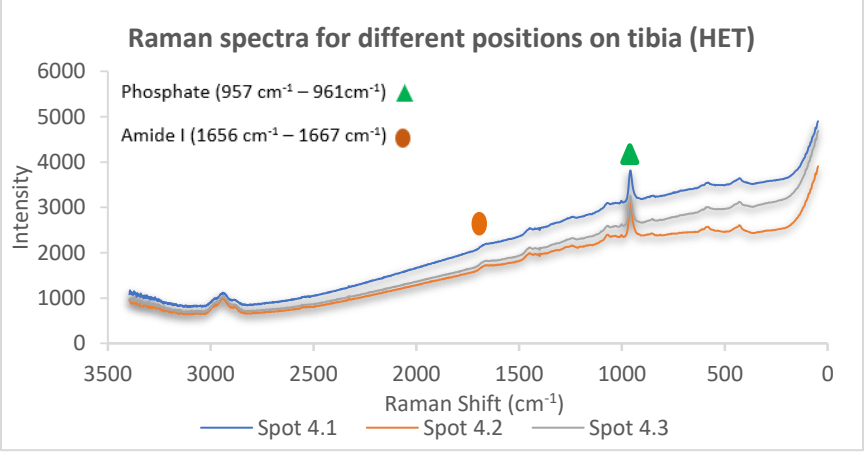

(a)

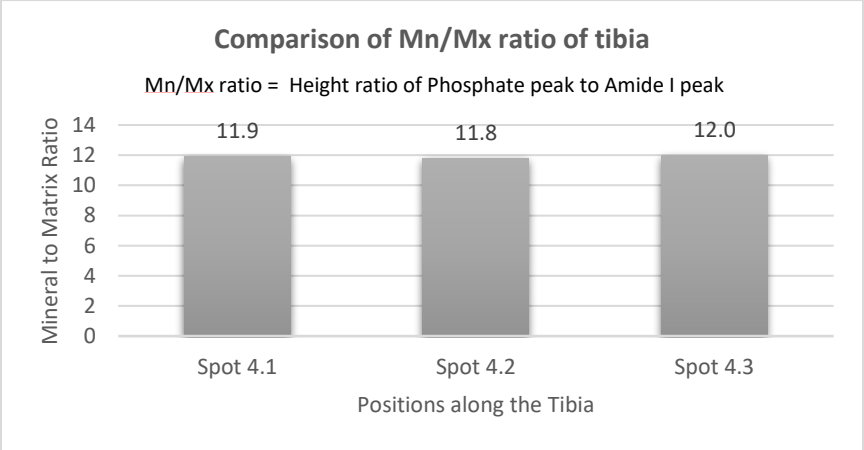

(b)

Figure 5-34 Periosteum tibia—3-10-17 5F HL (HET) (a) Raman spectra (b) Mn/Mx ratio

(v) 3-10-17 8F HL

Compared to other samples, this sample shows much less effect of fluorescence as shown in Figure 5-35a. There is considerable variation in Mn/Mx ratios between two different positions as shown in Figure 5-35b. The excessive presence of protein/organic materials may lead to a very low ratio for that particular position.

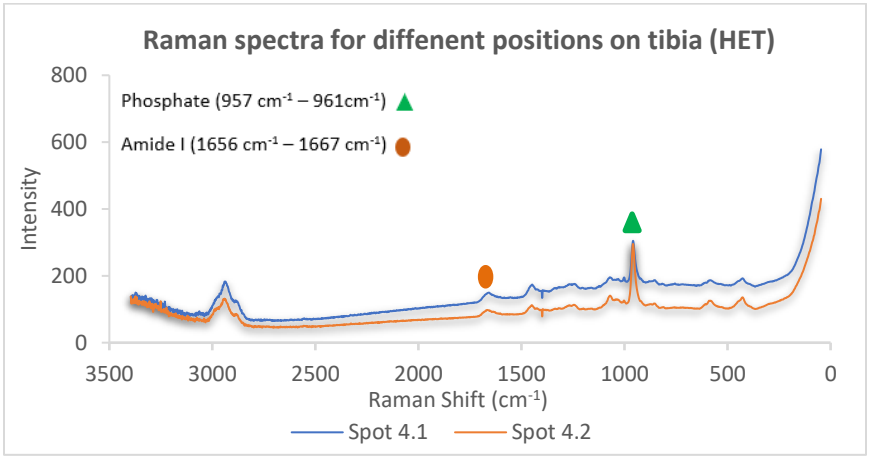

(a)

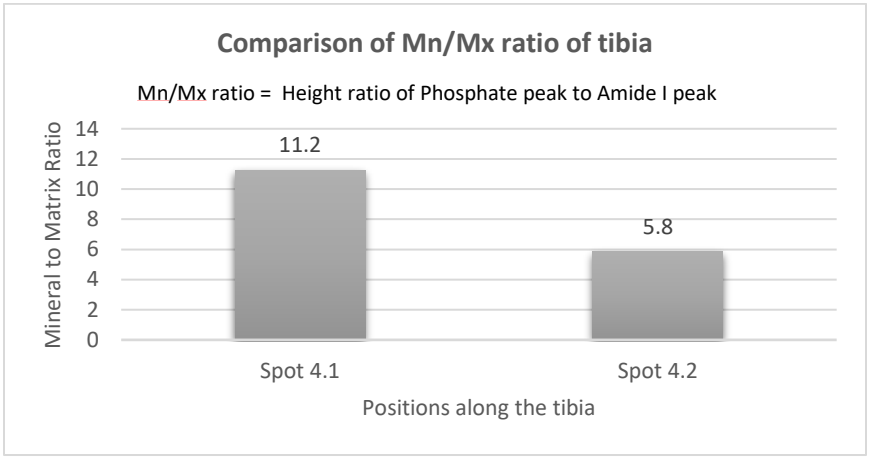

(b)

Figure 5-35 Periosteum tibia—3-10-17 8F HL (HET) (a) Raman spectra (b) Mn/Mx ratio

(vi) 3-10-17 9F HL

As shown in Figure 5-36a, spot 4.1 and spot 4.3 overlap each other. Still, there is a large difference in Mn/Mx ratios between both positions as shown in Figure 5-36b.

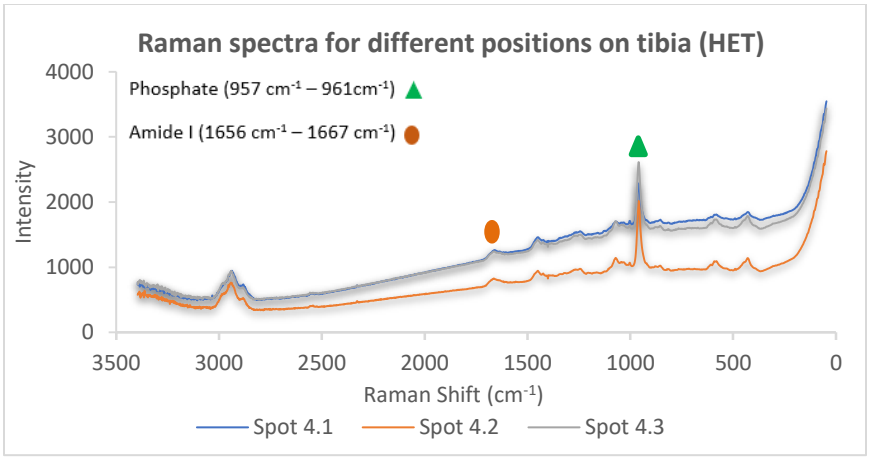

(a)

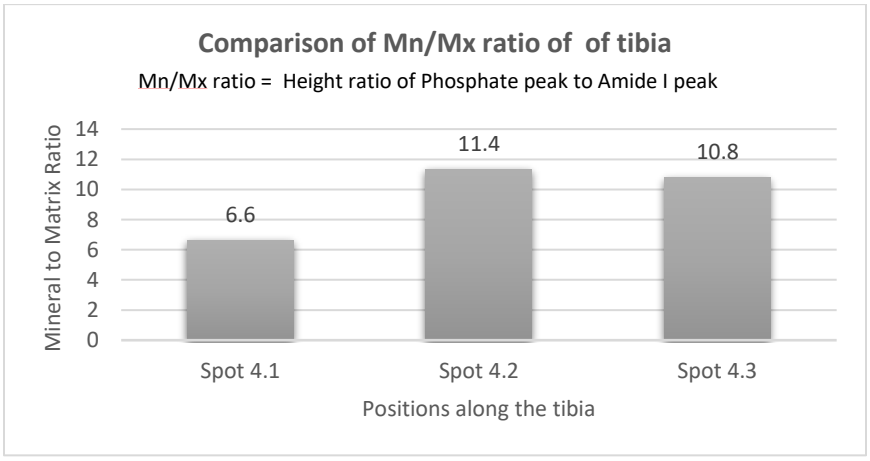

(b)

Figure 5-36 Periosteum tibia—3-10-17-17 9F HL (HET) (a) Raman spectra (b) Mn/Mx ratio

(vii) 3-10-17 10F HL

The sample shows a decrease in Mn/Mx ratio from the top to the bottom of the tibia (Figure 5-37b). However, Figure 5-37a indicates that the Raman signals are detectable for all positions.

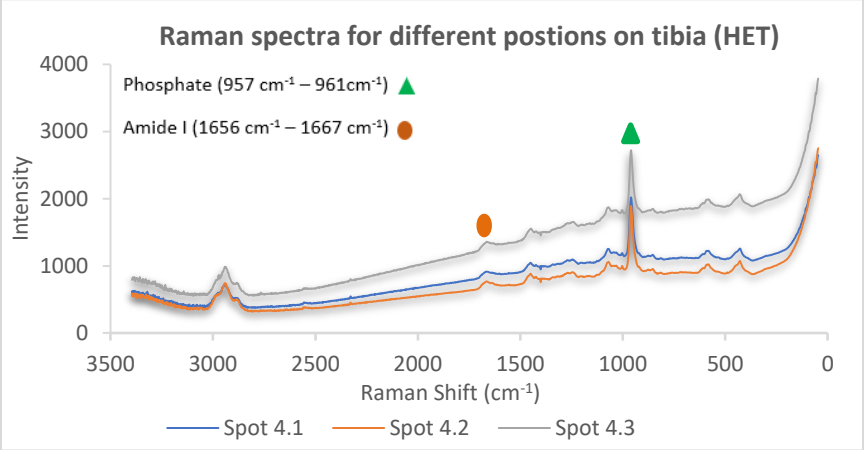

(a)

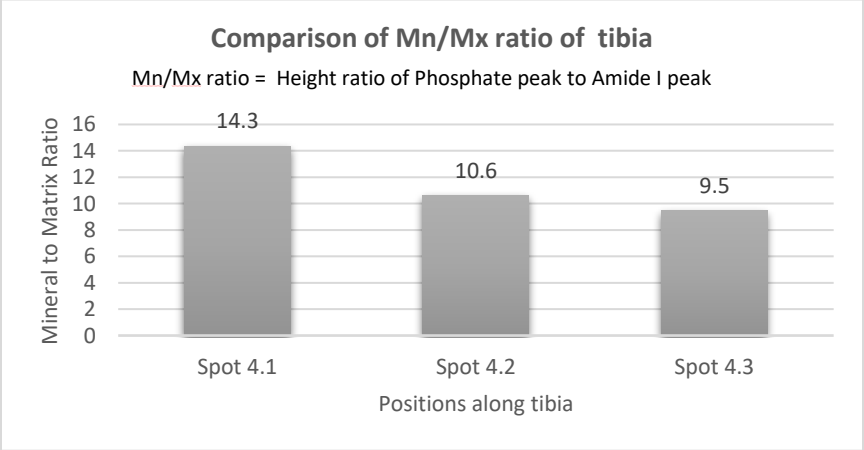

(b)

Figure 5-37 Periosteum tibia—3-10-17-17 10F HL (HET) (a) Raman spectra (b) Mn/Mx ratio

(viii) 3-13-17 6F HL

Figure 5-38a indicates that the height of the phosphate peak is relatively lower compared to the other samples. As shown in Figure 5-38b, spot 4.1 consists of much higher mineral content than the other two points. Spot 4.2 and Spot 4.3 show nearly equal Mn/Mx ratios, which is very close to the typical range in the literature.

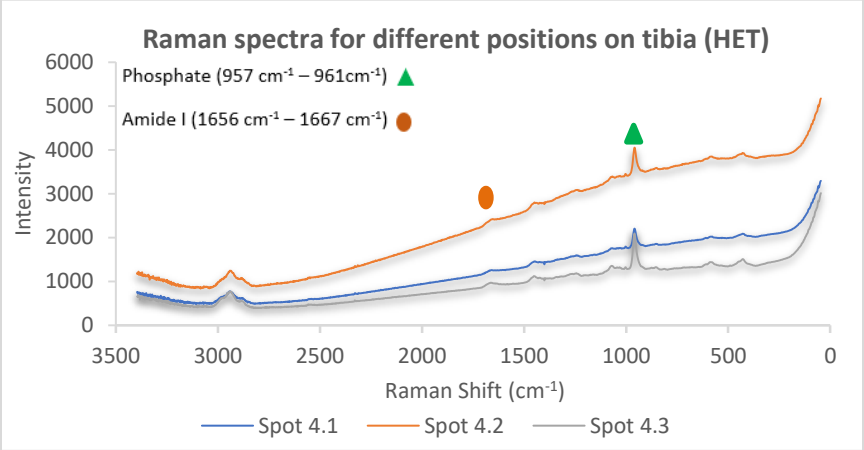

(a)

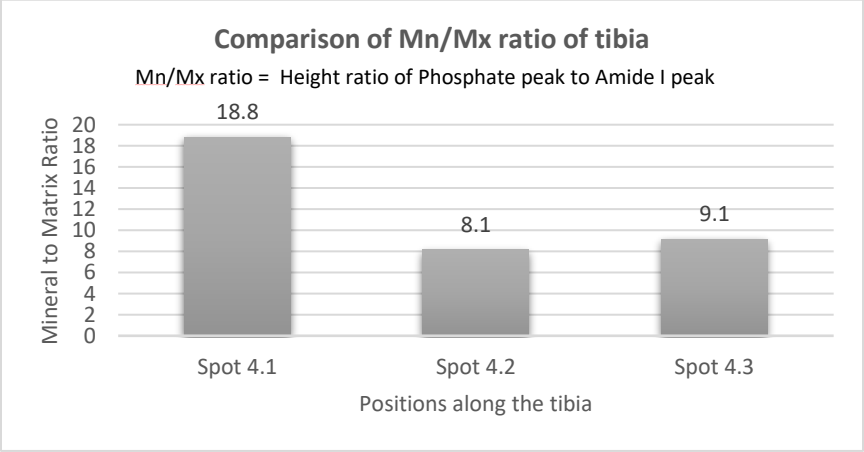

(b)

Figure 5-38 Periosteum tibia—3 -13-17 5F HL (HET) (a) Raman spectra (b) Mn/Mx ratio

5.1.4 Results and Discussion of Periosteum Tibia

Compared to the femur, the tibia shows a higher Mn/Mx ratio in KO (Figure 5-39). In comparison to WT and HET, it remains lower. Unlike the femur portion, WT and HET show a very small overall difference in Mn/Mx ratio. It is essential to take in consideration that the samples (i) 3-10-17 3F HL, (ii) 1-23-17 3F HL, and (iii) 3-10-17 8F HL are represented with just two spectra rather than three due to the interference of the other substances on the area to be detected. Thus, due to the deficiency of the cleanness of the sample, it became difficult to maintain the three spots for these samples. By comparing the femur and tibia, we can consider that the tibia is affected more due to the disability of the FSTL5 gene than the femur. The averages showing in Figure below consist of seven WT, three KO and eight HET samples.

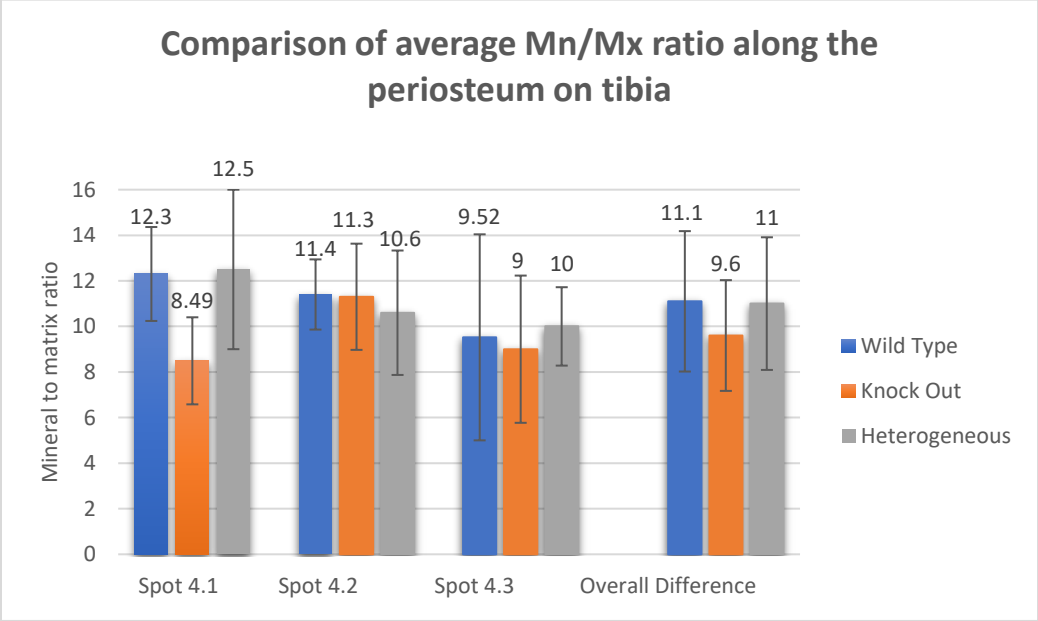

Figure 5-39 Average Mn/Mx ratio from periosteum tibia for all samples

5.2 Cortical Bone from Slide Sections (WT and KO)

Further, we concentrated on the measurement of mineral to matrix content from cortical bone. To get the longitudinal cut, we used a conventional bone cutter machine. Figure 5-40 represents the sample images after the longitudinal cut. We collected three spectra from each femur and tibia (two from metaphysis region, one from diaphysis) as shown in Figure 5-41. Table 5-2 is listed with the samples that we used for the cortical bone study.

Table 5-2 Sample ID and their type used for cortical bone

Sample ID	Sample Type
1-23-17 5F HL	WT
1-23-17 9F HL	KO
1-23-17 11F HL	KO
3-10-17 1F HL	WT
3-10-17 3F HL	KO
3-10-17 7F HL	WT
3-10-17 11F HL	WT
3-10-17 12F HL	WT
3-13-17 2F HL	WT
3-13-17 4F HL	WT
3-8-17 1F HL	WT
3-8-17 5F HL	WT
4-7-17 1F HL	KO
4-7-17 2F HL	KO
4-7-17 7F HL	KO

From the initial samples, we removed all HET and concentrated on WT and KO. From 10 samples, we had seven WT and three KO. Additionally, we received five extra rat bone samples containing two WT and three KO bones. For the study of cortical rat bones, we had a total of 15 samples, of which nine samples were WT and six were KO. Figures 5-40a and b clearly show the difference of surface before and after cleaning. We used the scaffold to remove excessive blood and marrow.

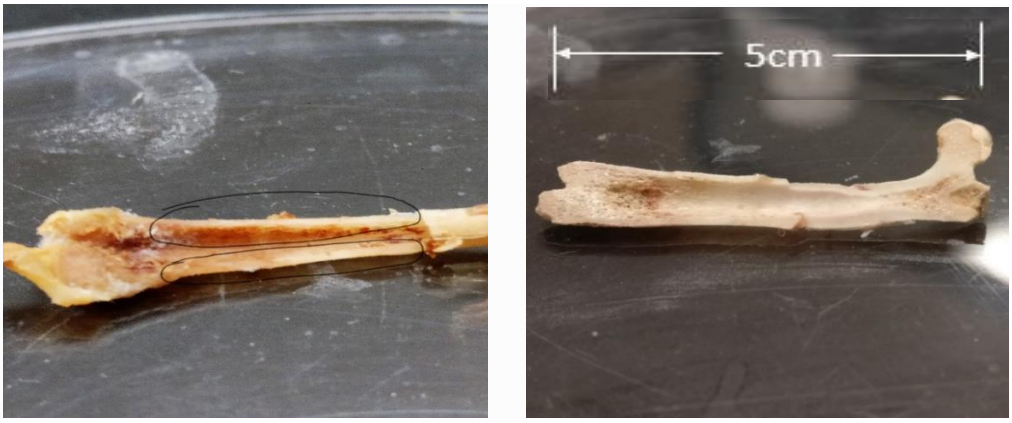

Figure 5-40 Longitudinal cut of femur sample (a) before cleaning (b) after cleaning

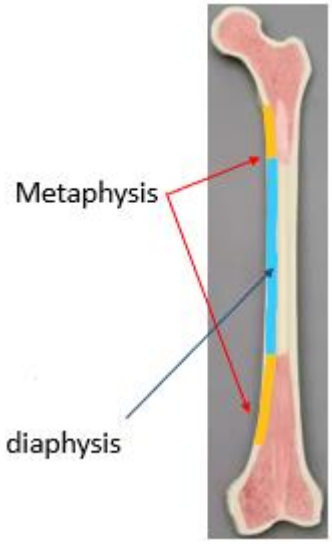

Figure 5-41 Image showing different positions along the cortical bone

5.2.1 Raman Spectra and Ratio of Cortical Bone of Femur

This section contains the spectra obtained from a cortical bone femur of a single sample but from different positions (Figure 5-41), along with the graph showing Mn/Mx ratios for those positions for all WT/KO rat bones.

(1) Wild-type samples

(i) 1-23-17 5F HL

Figure 5-42a shows the spectra taken from different positions. Compared to the other regions, diaphysis shows higher Mn/Mx ratios (Figure 5-42b).

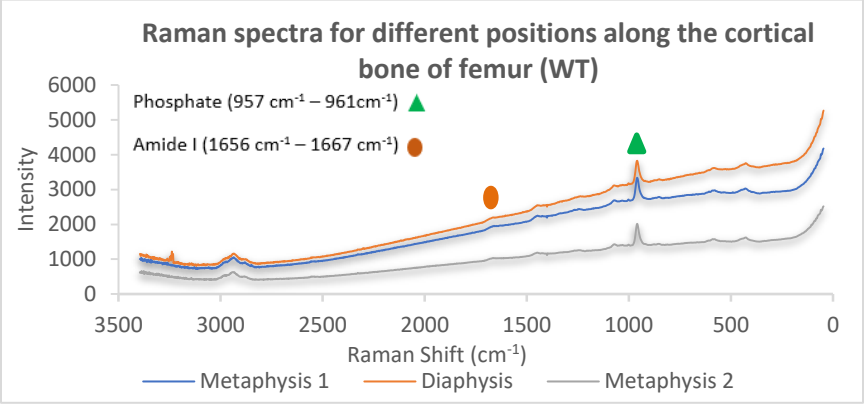

(a)

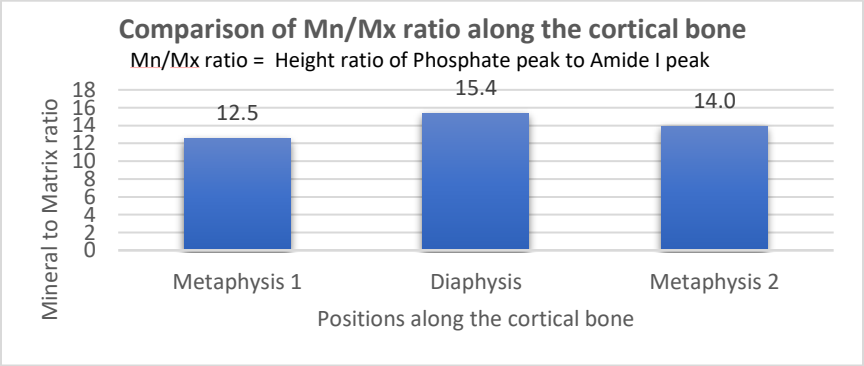

(b)

Figure 5-42 Cortical bone femur—1-23-17 5F HL (WT) (a) Raman spectra (b) Mn/Mx ratio

(ii) 3-10-17 1F HL

Figures 5-43a and b also show the consistency in the results. Although the ratio is consistent among all three spots, it is higher compared to the standard range.

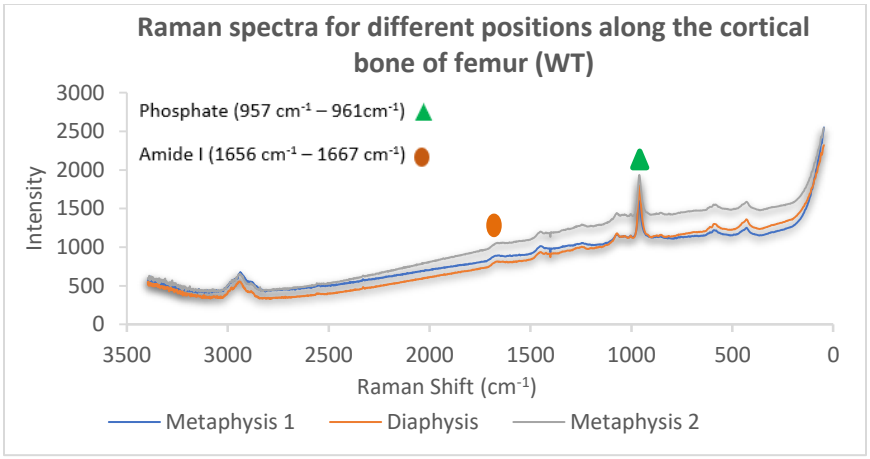

(a)

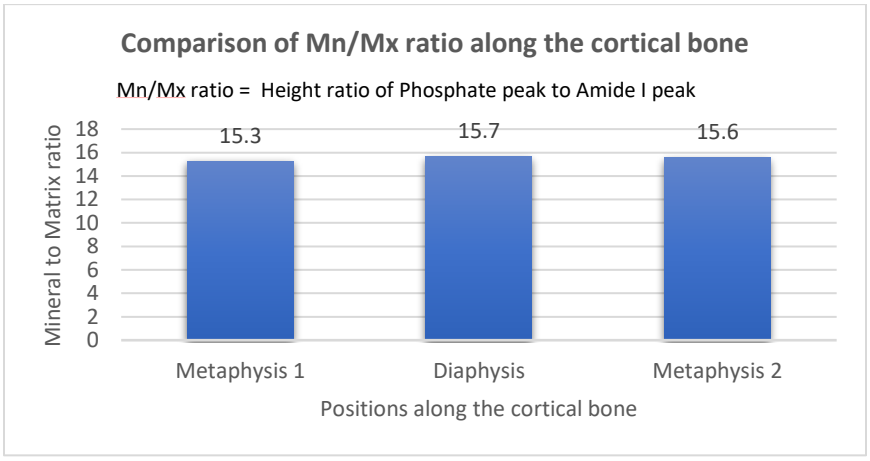

(b)

Figure 5-43 Cortical bone femur—3-10-17 1F HL (WT) (a) Raman spectra (b) Mn/Mx ratio

(iii) 3-10-17 7F HL

There is no sign of the amide I peak in all of the spectra as shown in the Figure 5-44a. However, analyzing the spectra with the help of Origin indicates a higher Mn/Mx ratio in a diaphysis portion (Figure 5-44b).

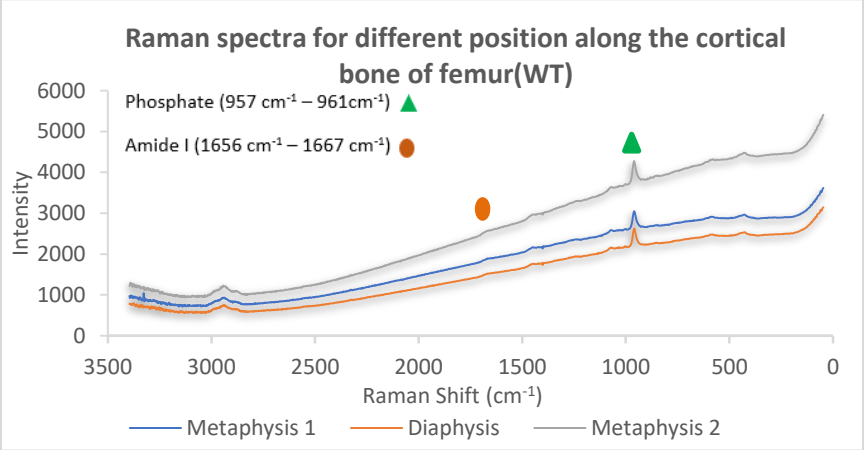

(a)

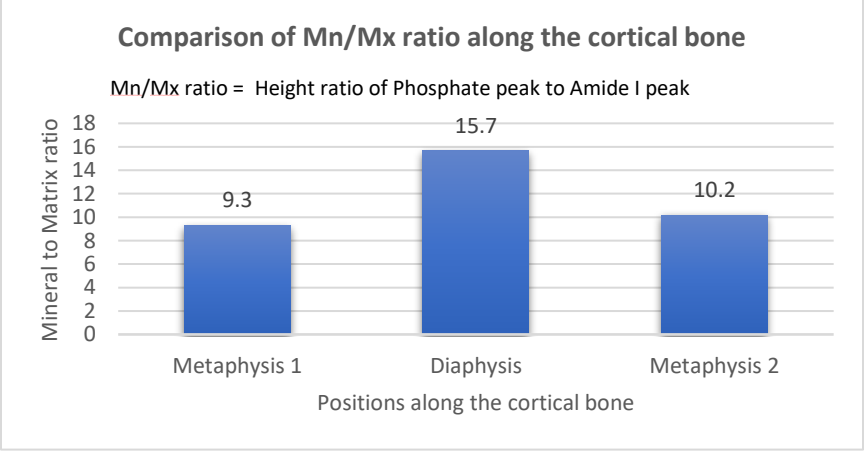

(b)

Figure 5-44 Cortical bone femur—3-10-17 7F HL (WT) (a) Raman spectra (b) Mn/Mx ratio

(iv) 3-10-17 11F HL

The sample does not show amide I peak with a proper peak height as shown in Figure 5-45a. Calculating the Mn/Mx ratio indicates a similar ratio for metaphysis 1 and diaphysis as shown in Figure 5-45b. But diaphysis 2 shows smaller Mn/Mx ratios.

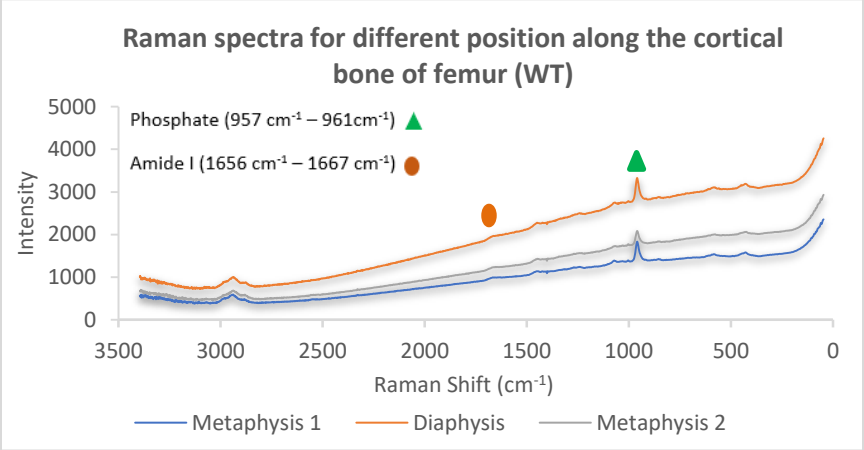

(a)

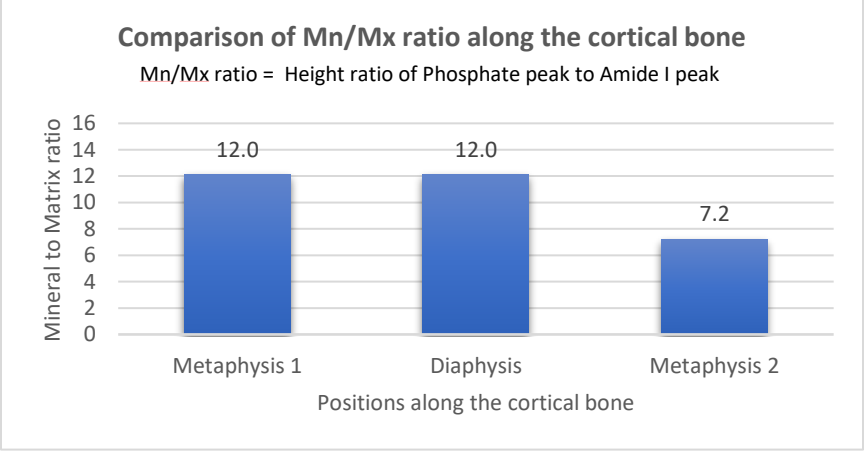

(b)

Figure 5-45 Cortical bone femur—3-10-17 11F HL (WT) (a) Raman spectra (b) Mn/Mx ratio

(v) 3-10-17 12F HL

Figure 5-46 shows the spectra obtained from two positions only. Sometimes while cutting the bone longitudinally, we faced an irregular cut because the particular portion was chipping away from the surface. So, this loss in the area caused loss in the spectrum for that position. But the obtained spectra are consistent in the Mn/Mx ratio as shown in Figure 5-46b.

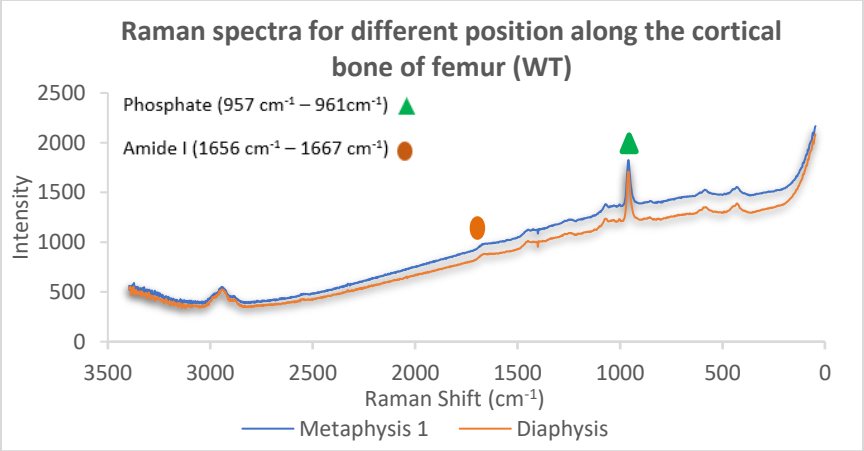

(a)

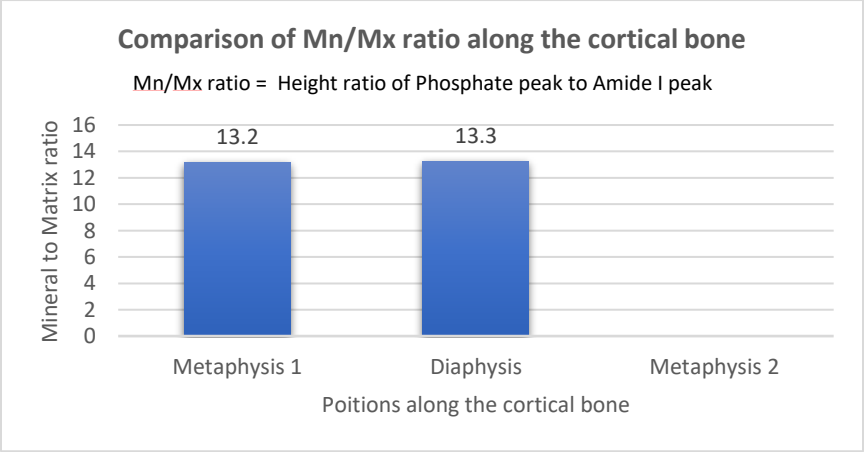

(b)

Figure 5-46 Cortical bone femur—3-10-17 12F HL (WT) (a) Raman spectra (b) Mn/Mx ratio

(vi) 3-13-17 2F HL

Unlike the previous cortical bone samples, this shows a higher Mn/Mx ratio on the two metaphysis ends than on the diaphysis as shown in the Figure 5-47b. Still, the graph shows a low variance among all these spots (Figure 5-47a).

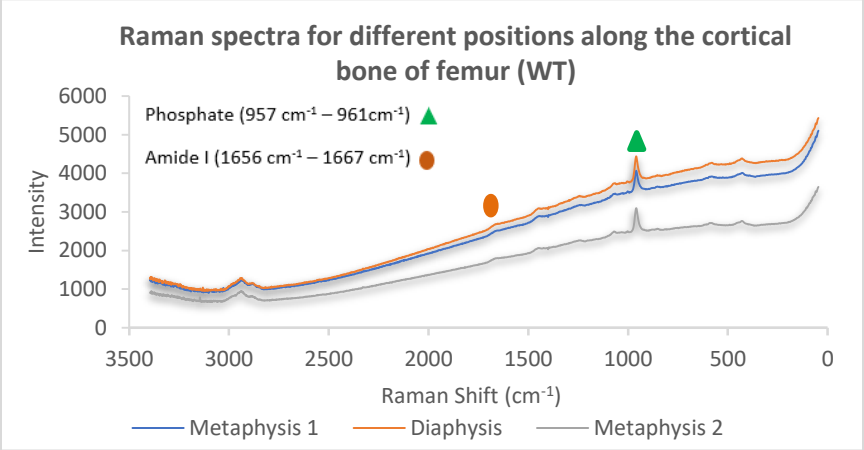

(a)

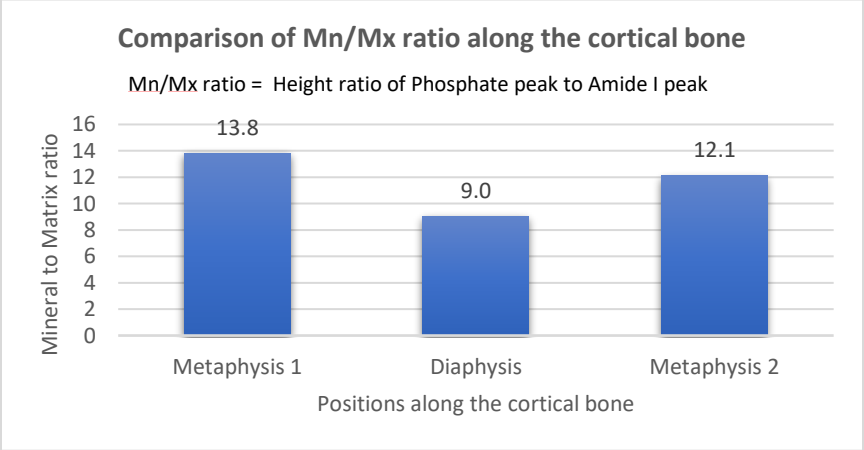

(b)

Figure 5-47 Cortical bone femur—3-13-17 2F HL (WT) (a) Raman spectra (b) Mn/Mx ratio

(vii) 3-13-17 4F HL

The spectra from the diaphysis and the metaphysis positions overlap each other as shown in Figure 5-48a. Again, like the last spectrum, the diaphysis shows lower Mn/Mx ratios than the two metaphysis ends as shown in Figure 5-48b.

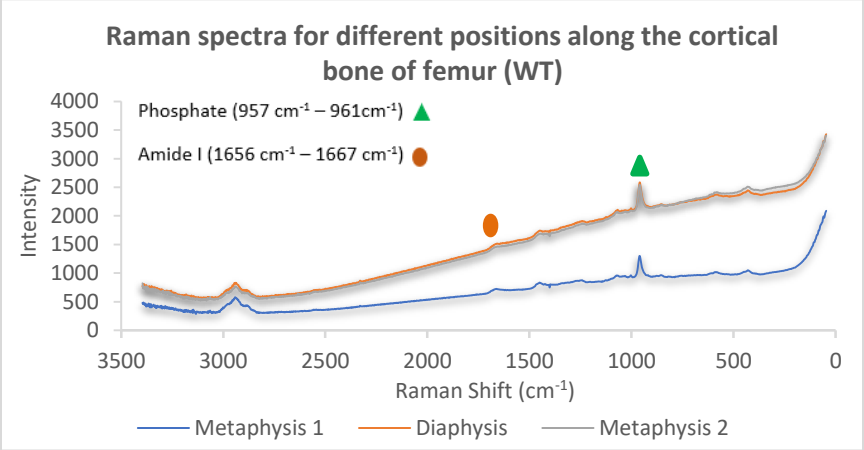

(a)

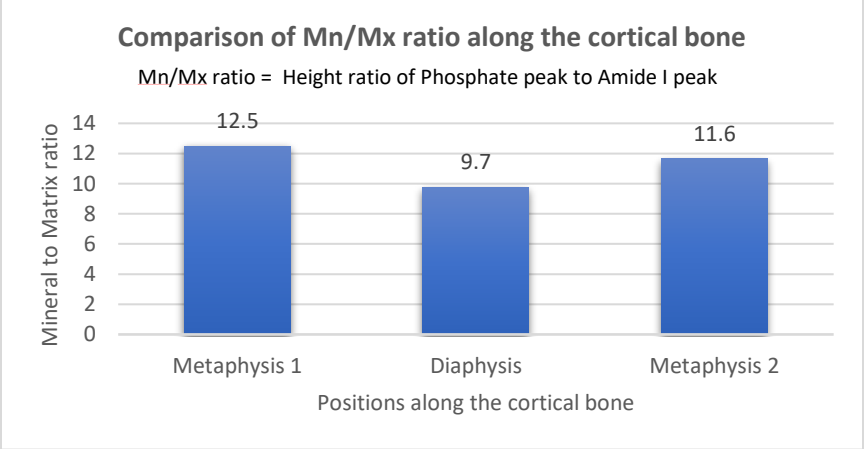

(b)

Figure 5-48 Cortical bone femur—3-13-17 4F HL (WT) (a) Raman spectra (b) Mn/Mx ratio

(viii) 3-8-17 1F HL

Figure 5-49a shows the spectra ranging from wavenumber 2000 to 500 cm^{-1}. We compared our full spectral range study (4000 to 200 cm^{-1}) to this confined spectral range (2000 to 500 cm^{-1}) study. We observed that confining the spectral range gives a wider understanding of the peaks' behavior. In the further study, we have used both the spectral ranges for our experimental run. Figure 4-49b shows the fall in Mn/Mx ratio.

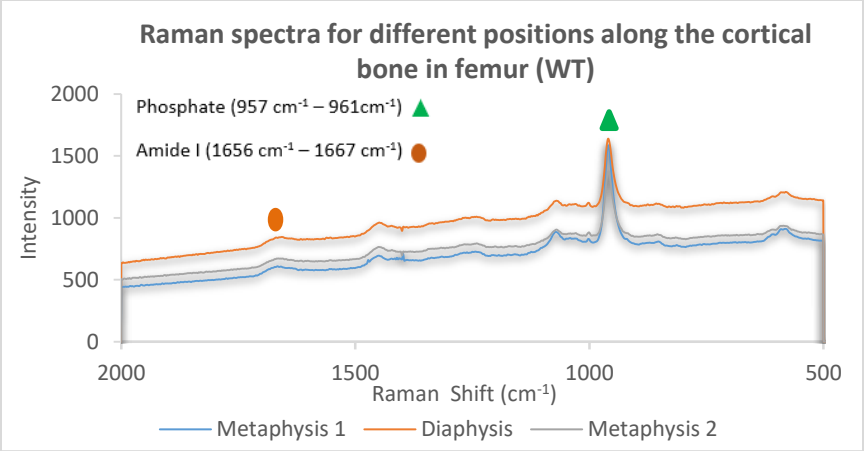

(a)

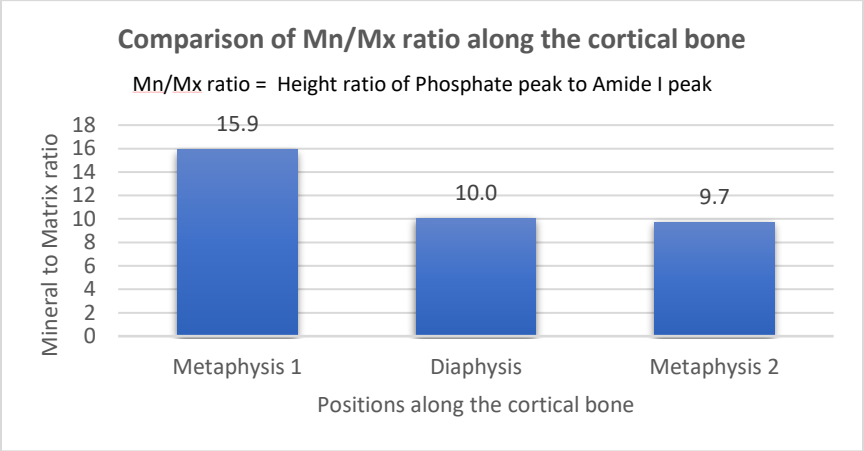

(b)

Figure 5-49 Cortical bone femur—3-8-17-17 1F HL (WT) (a) Raman spectra (b) Mn/Mx ratio

(ix) 3-8-17 5F HL

The spectra obtained for the sample are consistent as shown in Figure 5-50a. The sample shows similar Mn/Mx ratios for the metaphysis end and diaphysis (Figure 5-50b). However, the Mn/Mx ratio is much lower in the lower metaphysis region compared to the other regions.

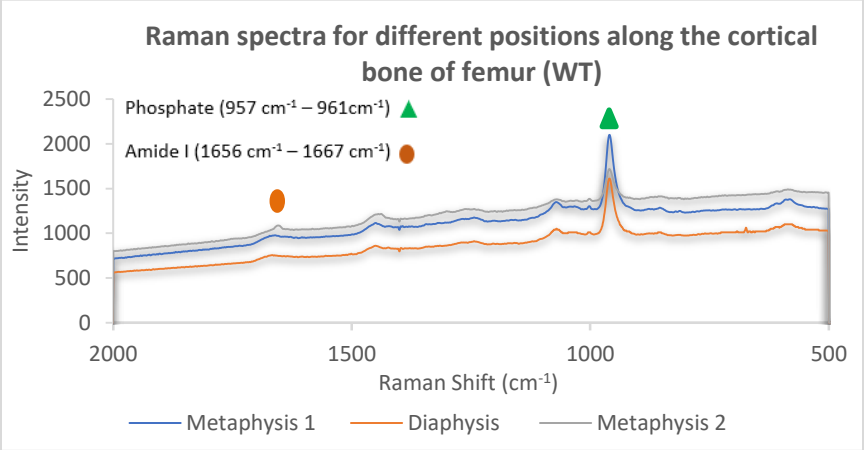

(a)

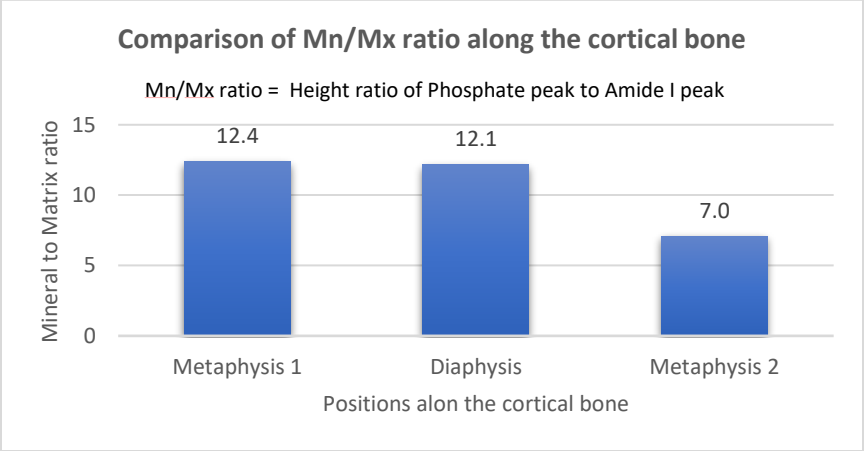

(b)

Figure 5-50 Cortical bone femur—3-8-17 5F HL (WT) (a) Raman spectra (b) Mn/Mx ratio

(2) Knockout samples

(i) 1-23-17 9F HL

Figure 5-51a shows similar spectra for all the positions along the cortical bone. The Mn/Mx ratio is also similar to each other as shown in Figure 5-51b.

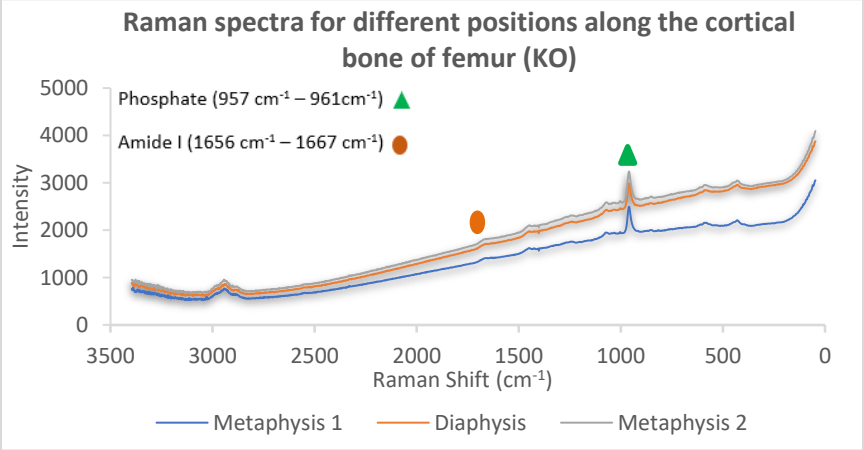

(a)

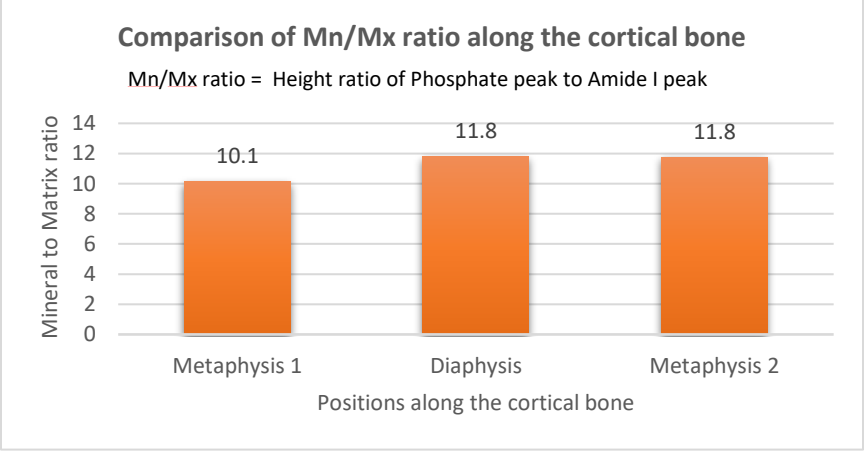

(b)

Figure 5-51 Cortical bone femur—1-23-17 9F HL (KO) (a) Raman spectra (b) Mn/Mx ratio

(ii) 1-23-17 11F HL

The Raman spectra do not give clear signals for the amide I peak shown in Figure 5-52a. It is clear from Figure 5-52b that metaphysis 1 shows a higher Mn/Mx ratio than both the other positions.

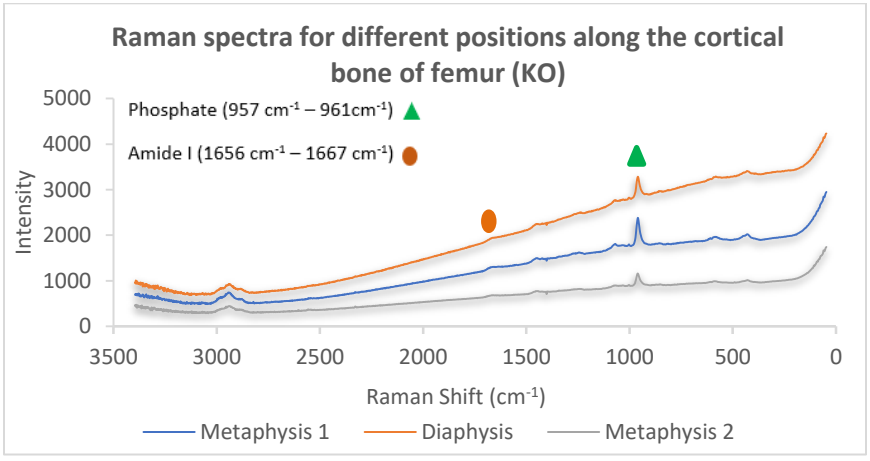

(a)

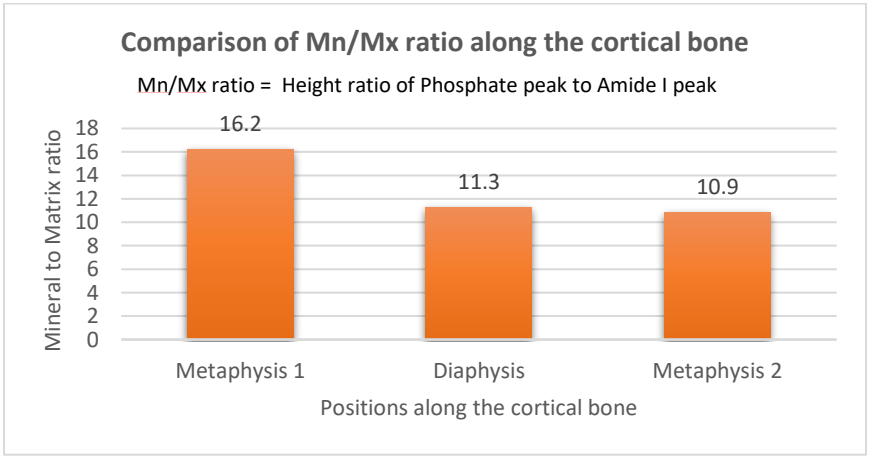

(b)

Figure 5-52 Cortical bone femur—1-23-17 11F HL (KO) (a) Raman spectra (b) Mn/Mx ratio

(iii) 3-10-17 3F HL

The sample shows a decrease in the Mn/Mx ratios from the top to the bottom of the bone (Figure 5-53b). The spectra do not indicate an observable amide I peak as shown in the Figure 5-53a. All the positions show only phosphate peaks with lower peak heights.

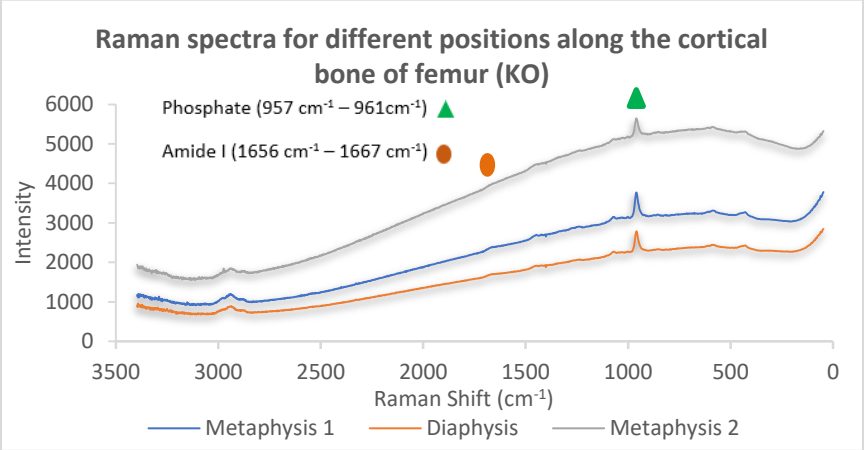

(a)

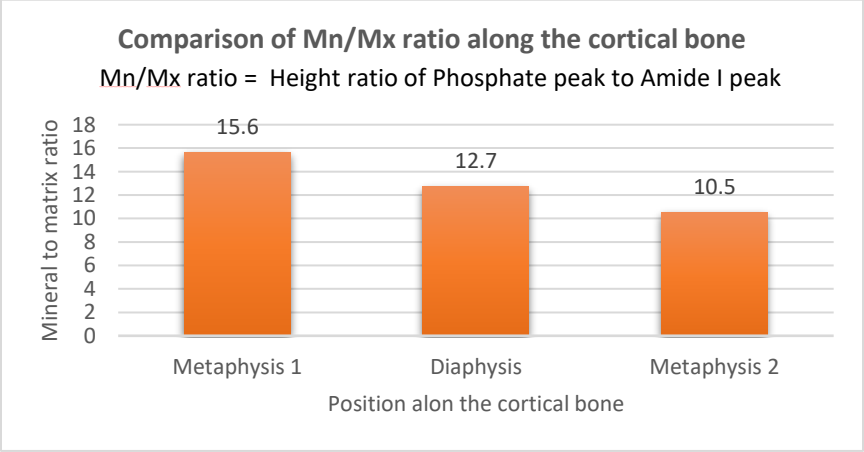

(b)

Figure 5-53 Cortical bone femur—3-10-17 3F HL (KO) (a) Raman spectra (b) Mn/Mx ratio

(iv) 4-7-17 1F HL

As shown in Figure 5-54a, all the spectra show consistency; the Mn/Mx ratio of all the positions is similar. However, there is an increase in Mn/Mx ratios from the top to the bottom of the cortical bone; there is not a high variance in the result as shown in the Figure 5-54b.

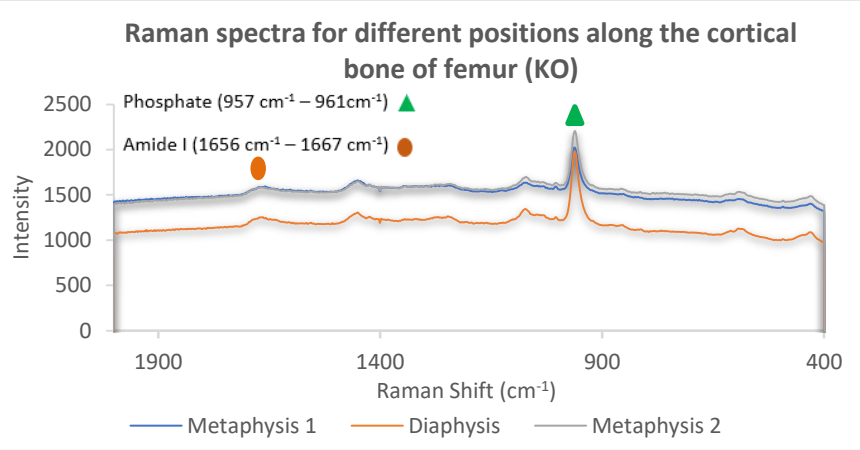

(a)

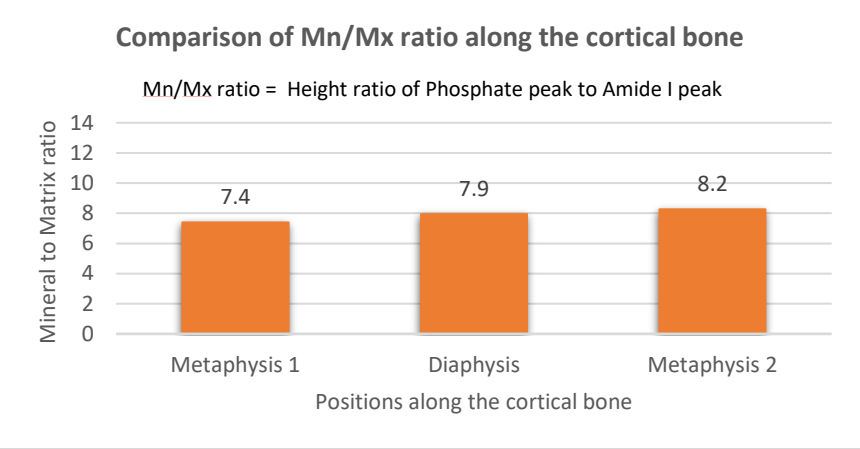

(b)

Figure 5-54 Cortical bone femur—4-7-17 1F HL (KO) (a) Raman spectra (b) Mn/Mx ratio

(v) 4-7-17 2F HL

The spectra show a very intense thin peak at the higher wavenumbers as shown in Figure 5-55a. However, those are part of an instrument error. Showing similarity on Raman spectra, the sample shows a higher Mn/Mx ratio on the diaphysis portion and a much lower ratio at metaphysis 2 as shown in Figure 5-55b.

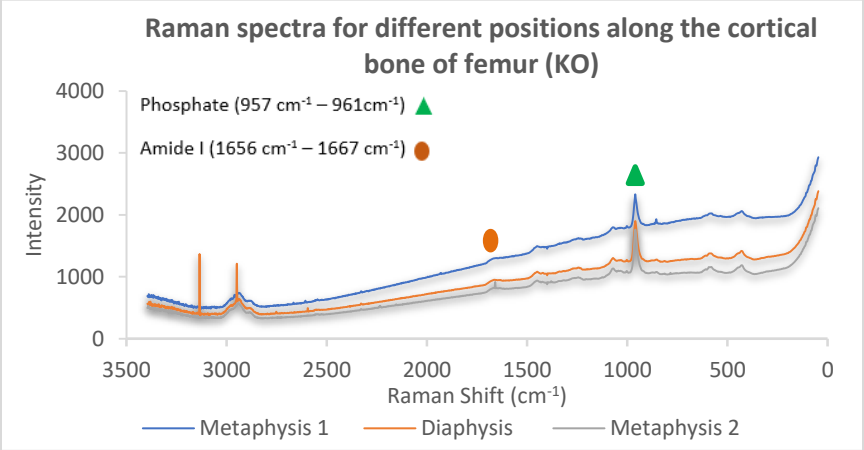

(a)

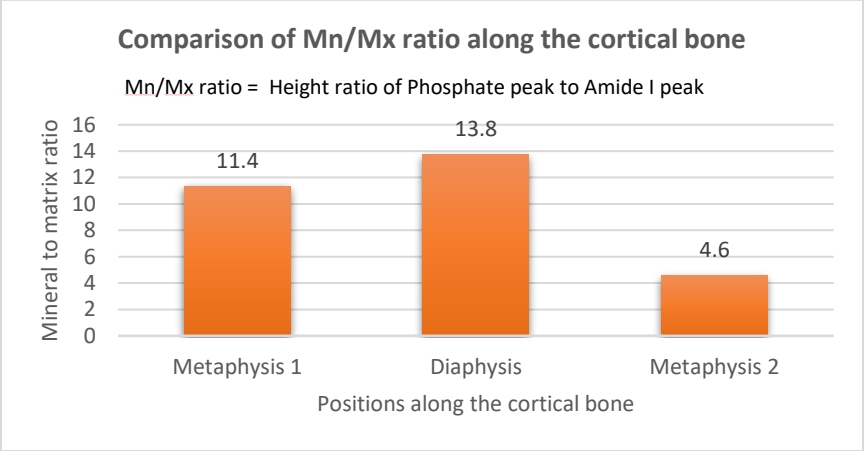

(b)

Figure 5-55 Cortical bone femur—4-7-17-17 2F HL (KO) (a) Raman spectra (b) Mn/Mx ratio

(vi) 4-7-17 7F HL

The sample shows the clear spectra with very low fluorescence as shown in Figure 5-56b. Similarly, like the previous sample, this sample also shows a higher ratio on the diaphysis portion than the other two portions as shown in Figure 5-56b. But the Mn/Mx ratios do not vary much with the positions.

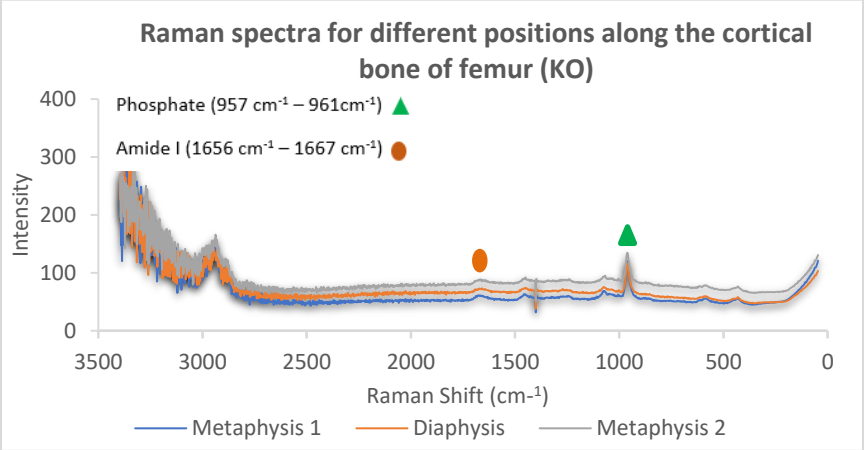

(a)

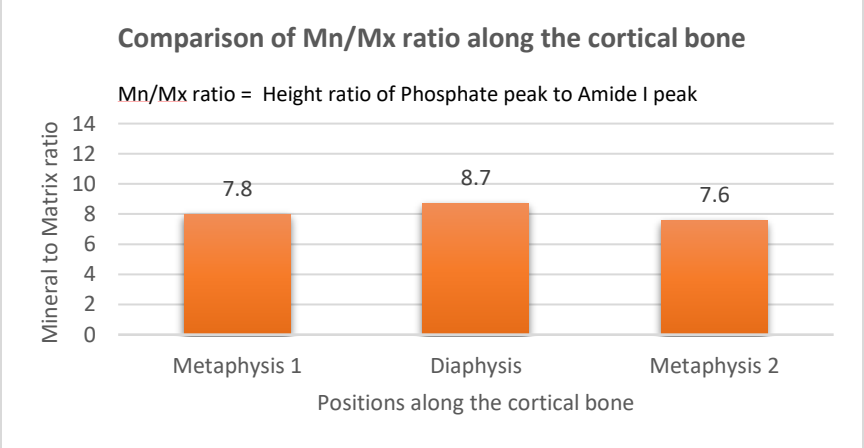

(b)

Figure 5-56 Cortical bone femur—4-7-17 7F HL (KO) (a) Raman spectra (b) Mn/Mx ratio

5.2.2 Results and Discussion of the Cortical Bone Femur

As shown in Figure 5-57, for all positions along the cortical bone, WT rat bones show a higher Mn/Mx ratio than in KO. Unlike the periosteum portion, we had a sufficient amount of the samples to compare. Some of the samples show the results for just two points because there was an unclean area where we could not get the results. Sometimes, there was also human error while cutting the samples longitudinally. Because of some irregular cuts, we lost an area of the detection. Metaphysis 2 positions clearly show an observable difference. Figure 5-57 shows the averages including nine WT and six KO samples.

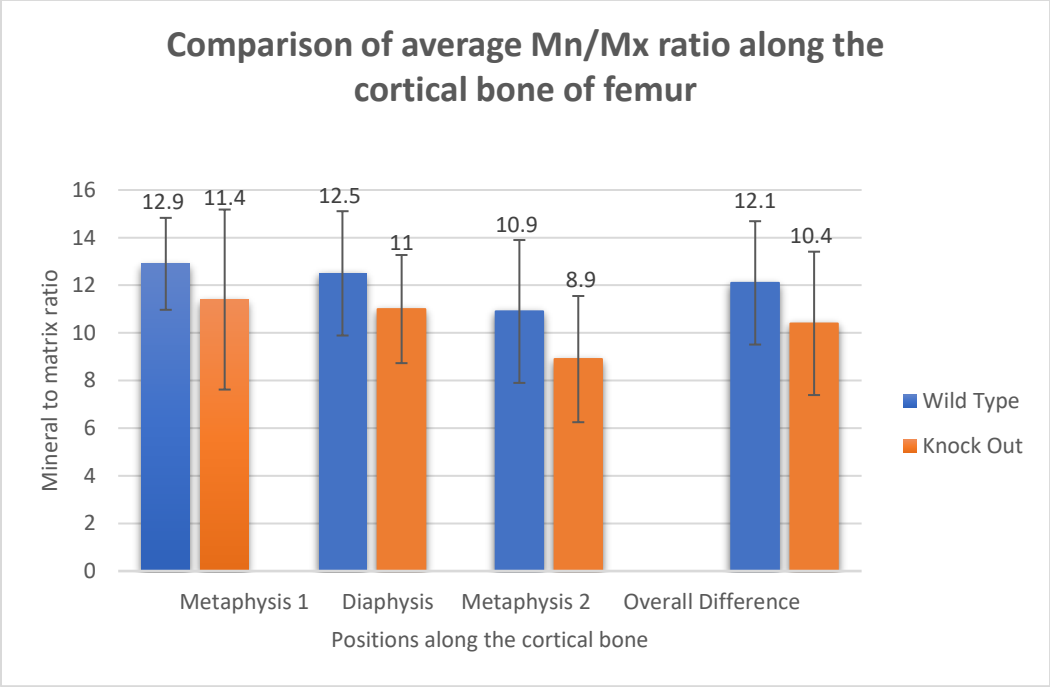

Figure 5-57 Average Mn/Mx ratio from cortical bone of femur

5.2.3 Raman Spectra and Ratio of Cortical Bone Tibia

This section contains the spectra obtained from a cortical bone tibia of a single sample but from different positions (Figure 5.41), along with the graph showing Mn/Mx ratios for those positions for all WT/KO rat bones.

(1) Wild-type

(i) 3-10-17 1F HL

Figure 5-58a does not show the clear peaks of the spectra. Figure 5-58b shows the Mn/Mx ratios for three different positions in the cortical bone. Here, the diaphysis region shows the lowest ratio.

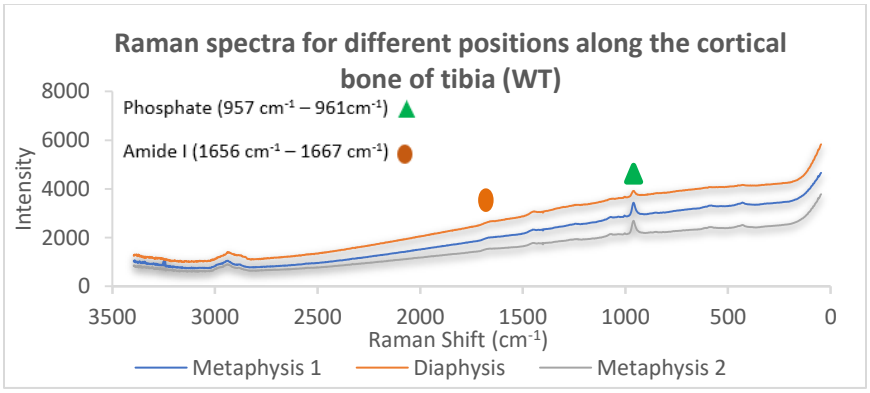

(a)

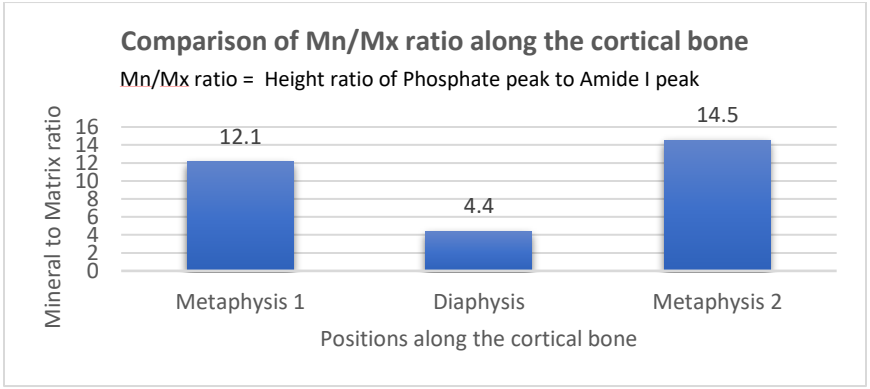

(b)

Figure 5-58 Cortical bone tibia—3-10-17 1F HL (WT) (a) Raman spectra (b) Mn/Mx ratio

(ii) 3-10-17 7F HL

The sample does not give a clear and intense signal for the desired peaks as shown in Figure 5-59a. Metaphysis 2 shows a high amount of fluorescence; however, observing these spectra in the software allows us to differentiate the peaks, and the ratio comes out to be lower in metaphysis 2 than the other two positions (Figure 5-59b).

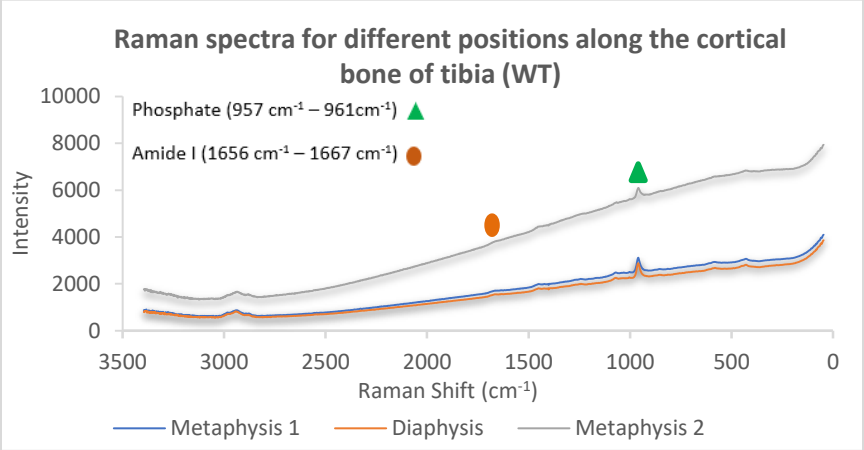

(a)

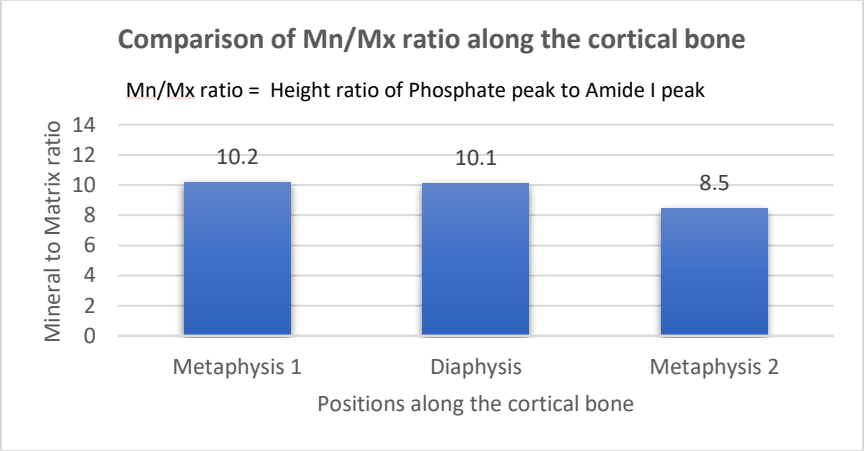

(b)

Figure 5-59 Cortical bone tibia—3-10-17 7F HL (WT) (a) Raman spectra (b) Mn/Mx ratio

(iii) 3-10-17 11F HL

The Raman spectra in Figure 5-60a illustrate the Mn/Mx ratio difference between different spots. Although without a clear and intense signal, the Mn/Mx ratio comes out considerably different for all the positions as shown in Figure 5-60b.

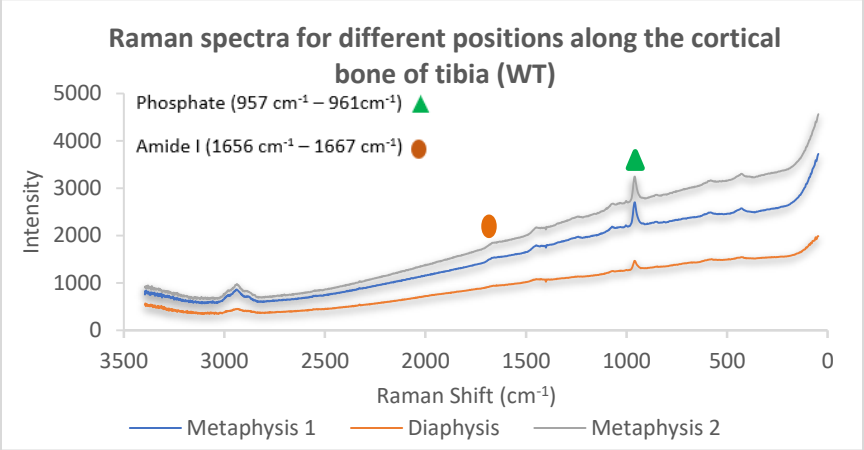

(a)

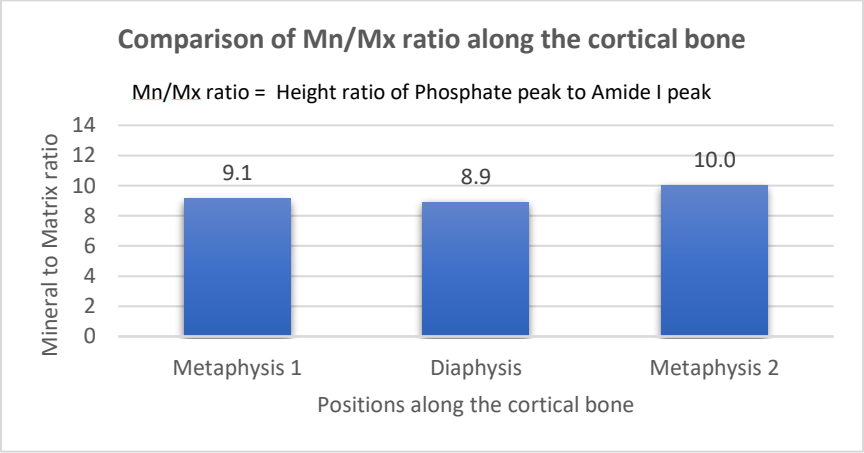

(b)

Figure 5-60 Cortical bone tibia—3-10-17 11F HL (WT) (a) Raman spectra (b) Mn/Mx ratio

(iv) 3-10-17 12F HL

As shown in Figure 5-61a, it is clear that the metaphysis 1 does not have the peak height for the amide I peak, which makes the Mn/Mx ratio very high. The other two positions show decent Mn/Mx ratios, with much less variation (Figure 5-61b).

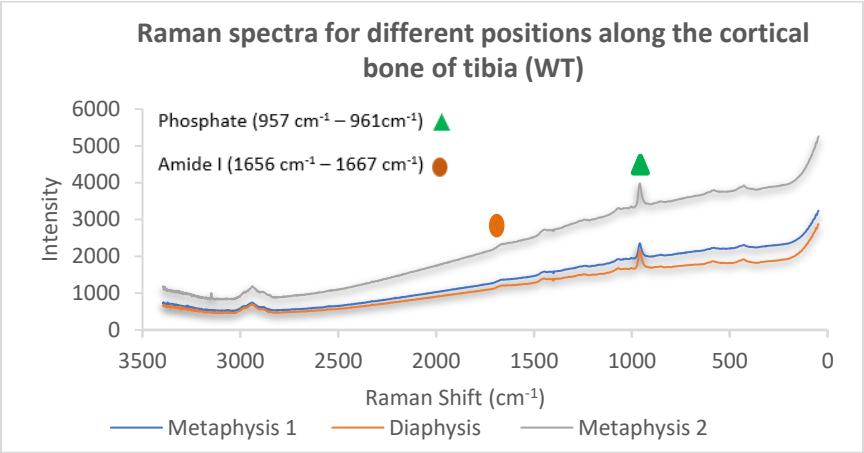

(a)

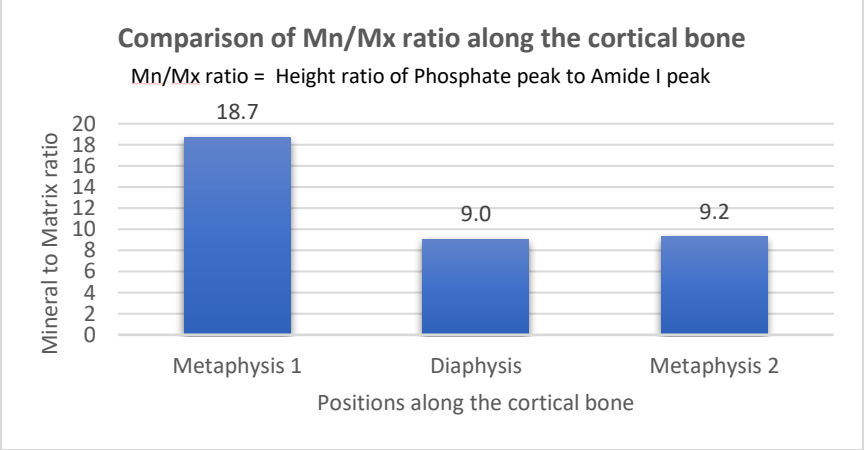

(b)

Figure 5-61 Cortical bone tibia—3-10-17 12F HL (WT) (a) Raman spectra (b) Mn/Mx ratio

(v) 3-13-17 2F HL

Figure 5-62a shows the Raman spectra of three different positions. Like the previous few samples, there is a weak signal for amide I peak. However, calculating those using the software gives the Mn/Mx ratio that decreases according to the bone positions (as shown in Figure 5-62b).

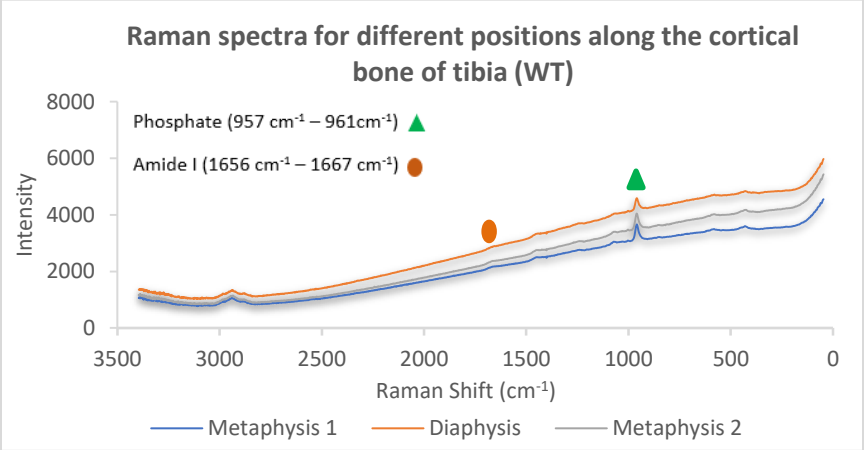

(a)

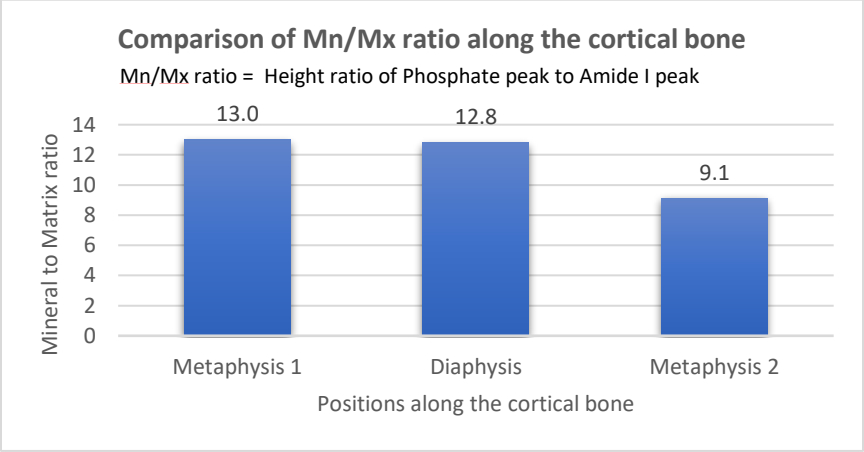

(b)

Figure 5-62 Cortical bone tibia—3-13-17 2F HL (WT) (a) Raman spectra (b) Mn/Mx ratio

(vi) 3-13-17 4F HL

Figure 5-63a shows the overlapping spectra for two different positions. The bar chart shown in Figure 5-63b indicates the highest Mn/Mx ratio on the diaphysis region. Two metaphysis positions show lower Mn/Mx ratios.

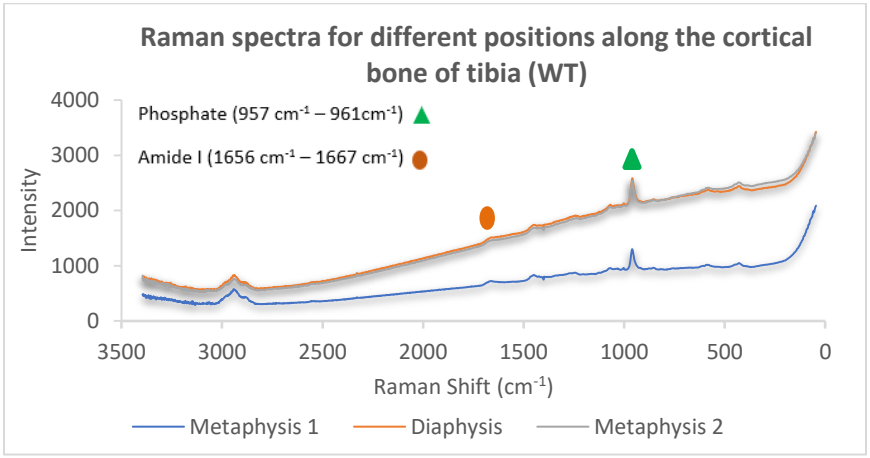

(a)

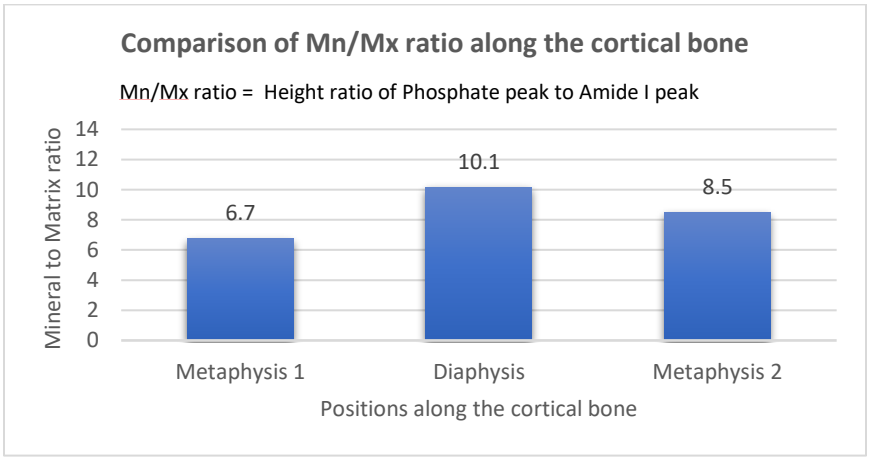

(b)

Figure 5-63 Cortical bone tibia—3-13-17 4F HL (WT) (a) Raman spectra (b) Mn/Mx ratio

(vii) 3-8-17 1F HL

Figure 5-64b indicates that there is a significant variation in the Mn/Mx ratios for all the different positions. Figure 5-64b shows that the Metaphysis 1 portion shows less height of the phosphate peak, which in turn results in such a low ratio, whereas the other two positions show an Mn/Mx ratio in the ideal range.

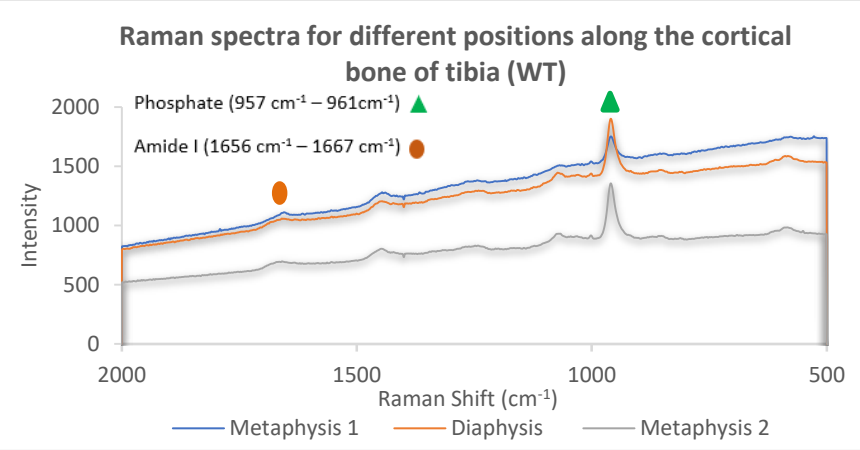

(a)

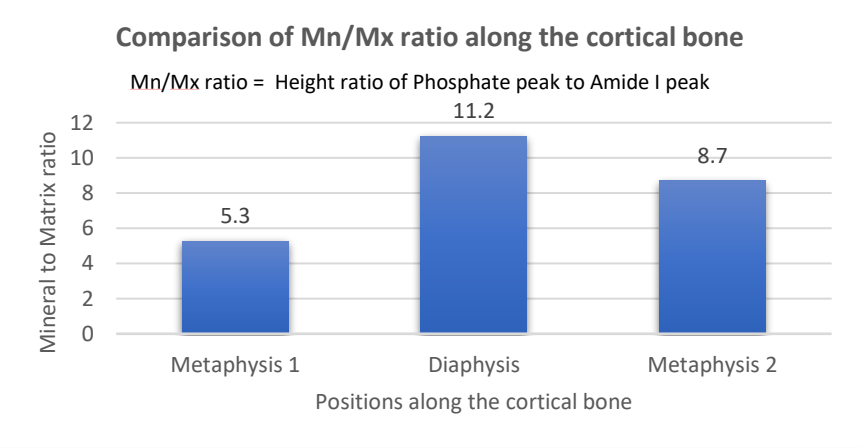

(b)

Figure 5-64 Cortical bone tibia—3-8-17 1F HL (WT) (a) Raman spectra (b) Mn/Mx ratio

(viii) 3-8-17 5F HL

It is seen from the Figure 5-65a that all the spectra from the different positions overlap one other, so it is difficult to predict the behavior of these positions. Calculating the spectral heights shows the lowest ratio from the diaphysis region (as shown in Figure 5-65b).

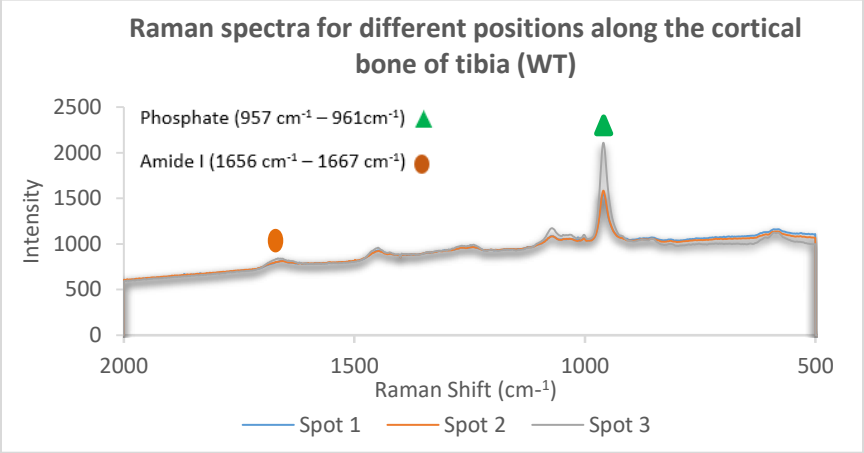

(a)

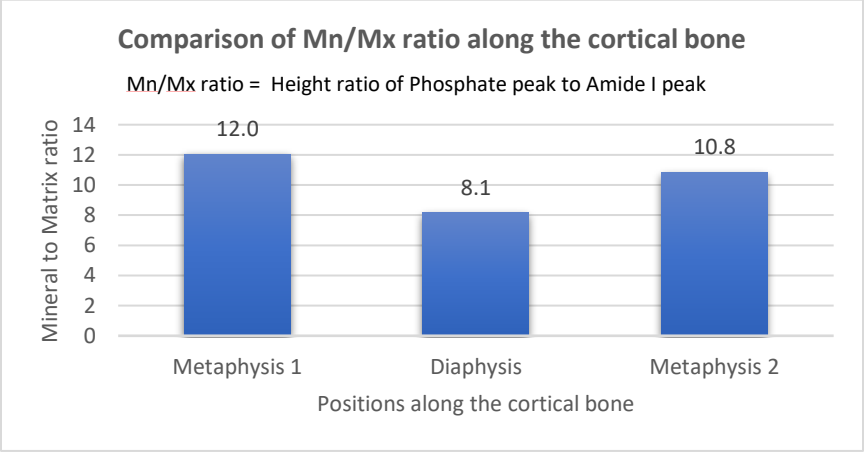

(b)

Figure 5-65 Cortical bone tibia—3-8-17 5F HL (WT) (a) Raman spectra (b) Mn/Mx ratio

(2) Knockout samples

(i) 1-23-17 9F HL

Figure 5-66a shows that like the previous sample, this sample also gives spectra with very similar intensities that overlap. Figure 5-66b represents the calculation of the Mn/Mx ratio and shows some variation for all the positions.

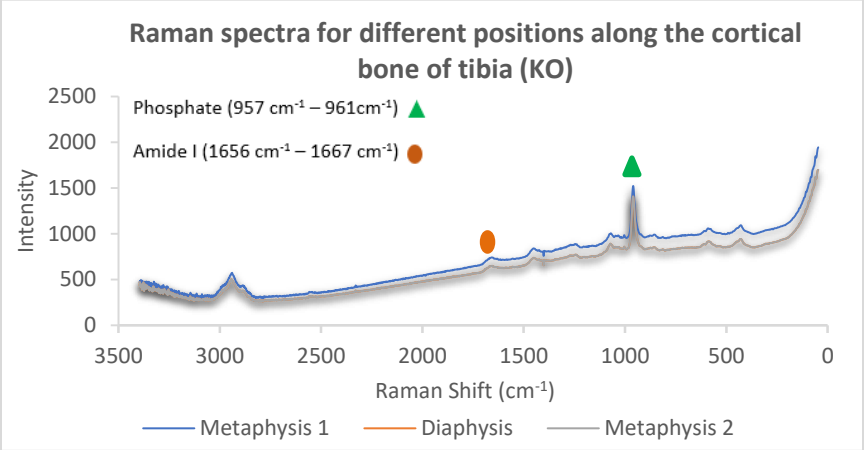

(a)

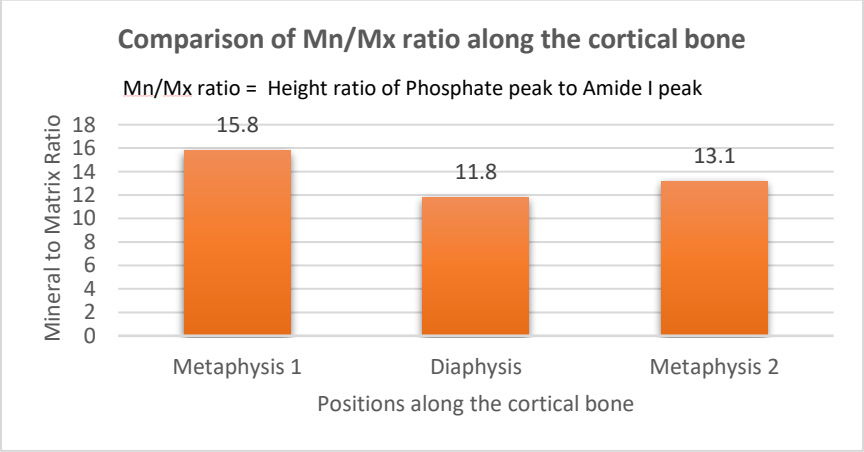

(b)

Figure 5-66 Cortical bone tibia—1-23-17 9F HL (KO) (a) Raman spectra (b) Mn/Mx ratio

(ii) 1-23-17 11F HL

Although Figure 5-67a does not give any idea of the Mn/Mx ratios in different positions, Figure 5-67b represents a good number of ratios. The diaphysis region gives a higher ratio than the other two spots.

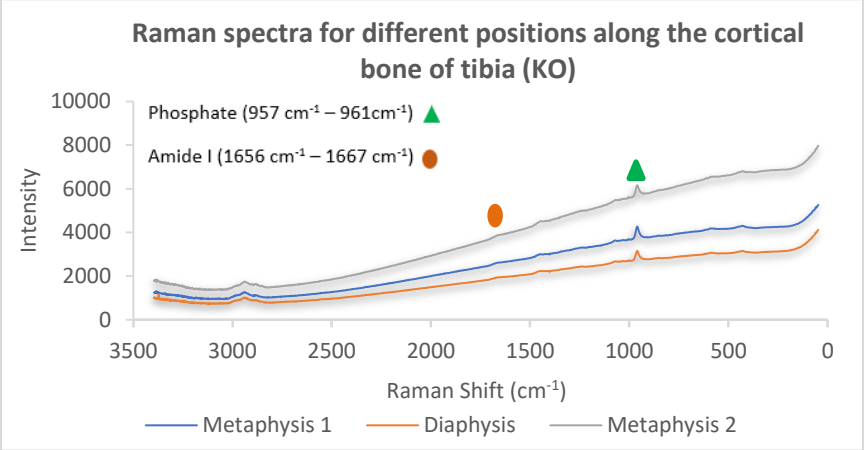

(a)

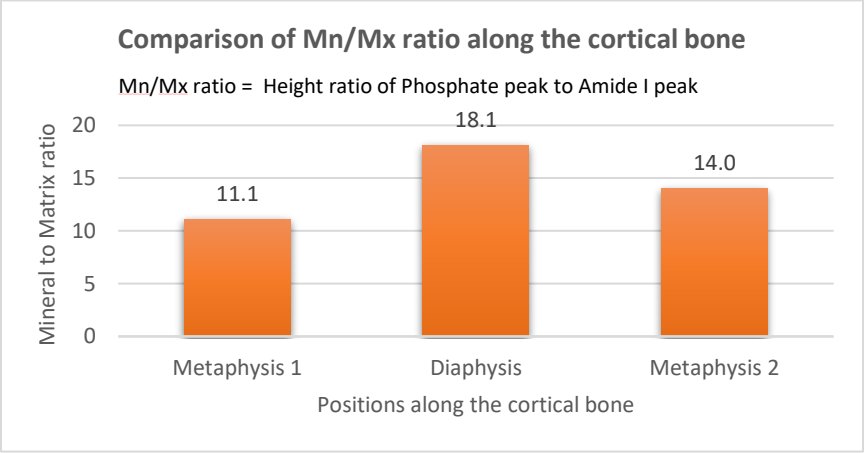

(b)

Figure 5-67 Cortical bone tibia—1-23-17 11F HL (KO) (a) Raman spectra (b) Mn/Mx ratio

(iii) 3-10-17 3F HL

Figure 5-68a shows that the Mn/Mx ratio decreases along the sample positions from top to bottom of the cortical bone. The variation in Mn/Mx ratios for different positions is less (as shown in Figure 5-68b).

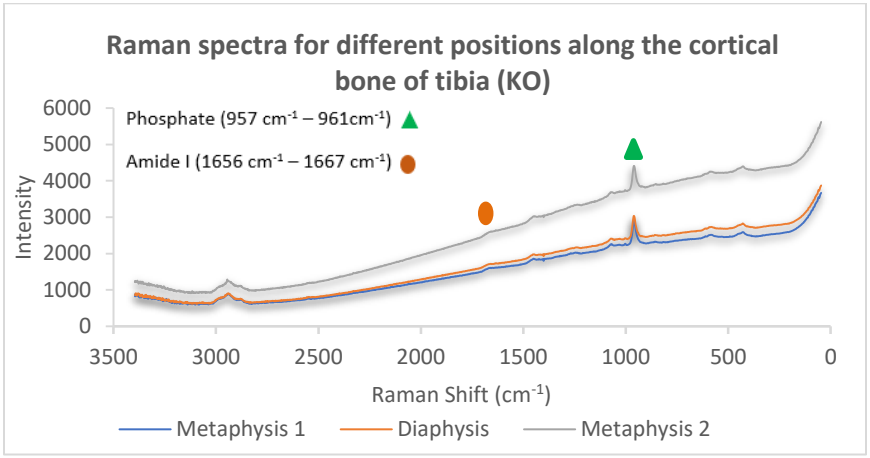

(a)

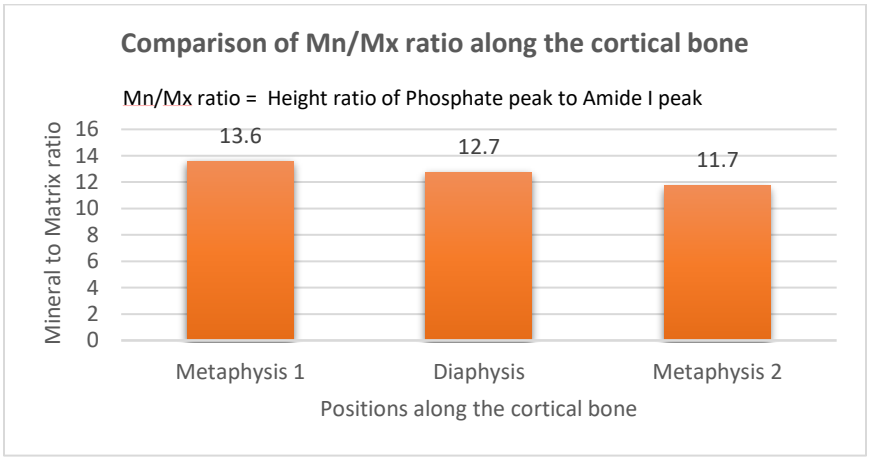

(b)

Figure 5-68 Cortical bone tibia—3 10-17 3F HL (KO) (a) Raman spectra (b) Mn/Mx ratio

(iv) 4-7-17 1F HL

Figure 5-69a shows the regular spectra obtained from different positions. Figure 5-69b shows an increase in the Mn/Mx ratio from top to bottom along the positions of the cortical bone. The variance in the diaphysis and metaphysis positions is very low.

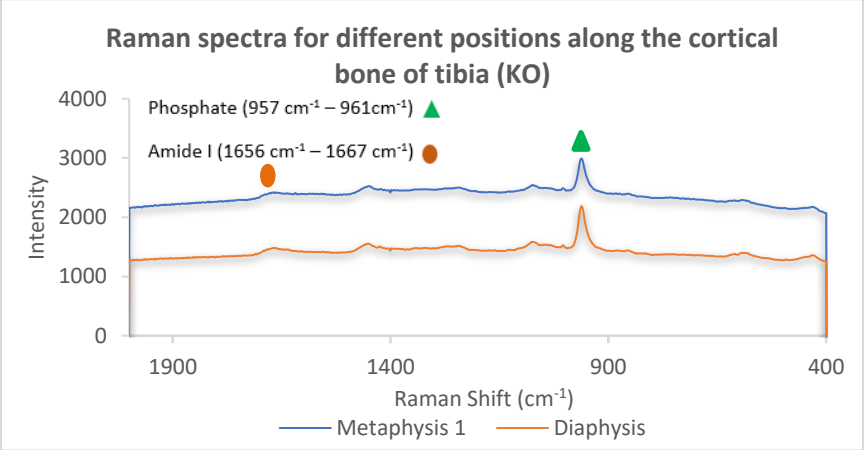

(a)

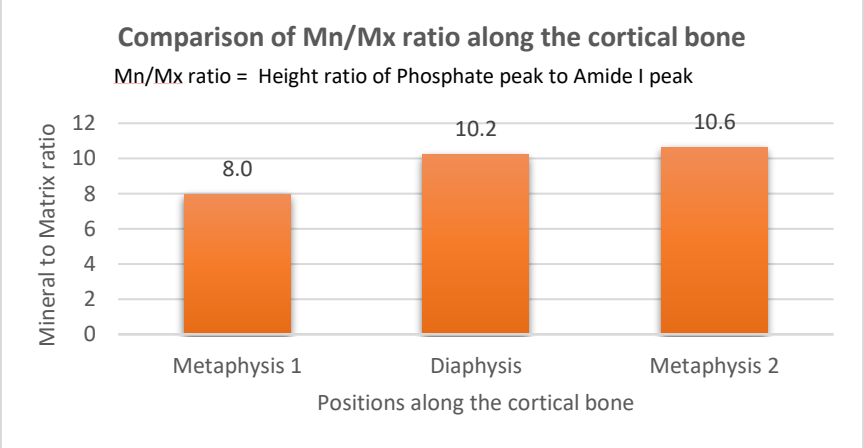

(b)

Figure 5-69 Cortical bone tibia—4-7-17 1F HL (KO) (a) Raman spectra (b) Mn/Mx ratio

(v) 4-7-17 2F HL

Figure 5-70a shows spectra for all the bone positions. The Mn/Mx ratios for different positions also fall within an ideal range. The Mn/Mx ratios for metaphysis 1 and diaphysis are mostly similar (as shown in Figure 5-70b).

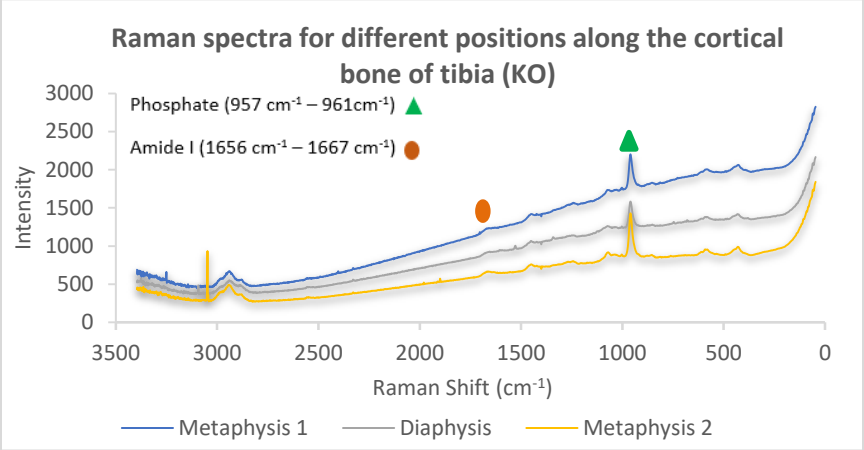

(a)

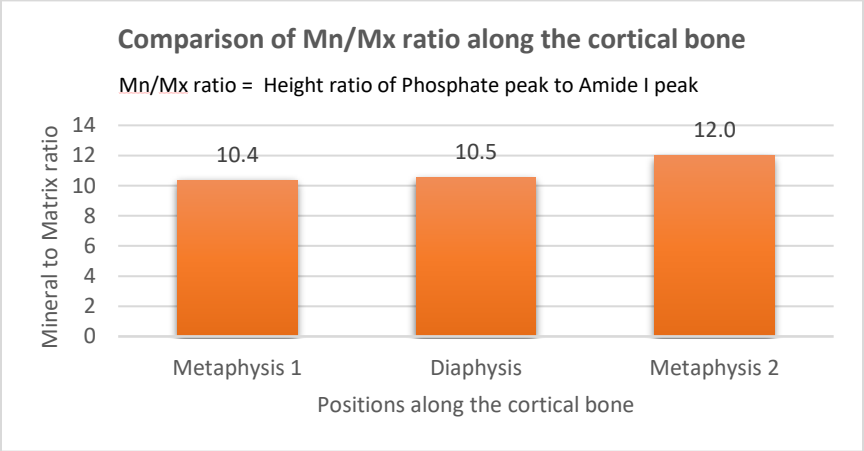

(b)

Figure 5-70 Cortical bone tibia—4-7-17 2F HL (KO) (a) Raman spectra (b) Mn/Mx ratio

(v) 4-7-17 7F HL

From Figure 5-71a, it is clear that the spectra for higher wavenumber regions show much noise compared to all other samples, but the lower wavenumber region gives the detectable peaks. The diaphysis region shows a normal Mn/Mx ratio, but both metaphysis ends show a lower ratio. This ratio is consistent for these two ends (as shown in Figure 5-71b).

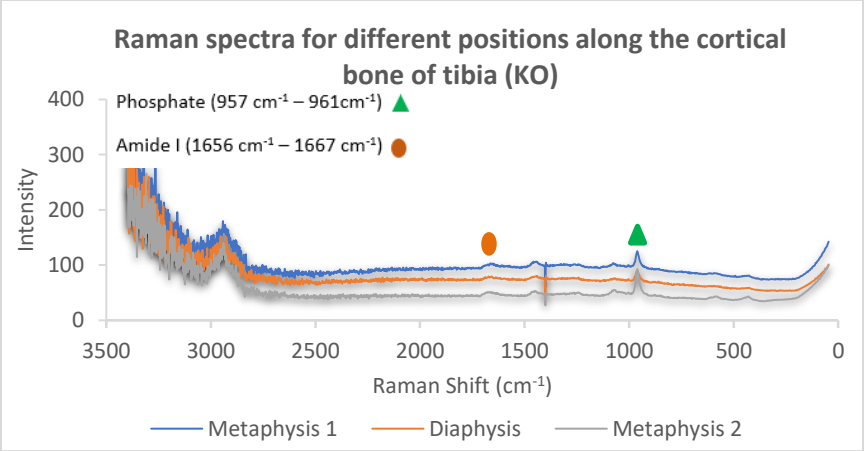

(a)

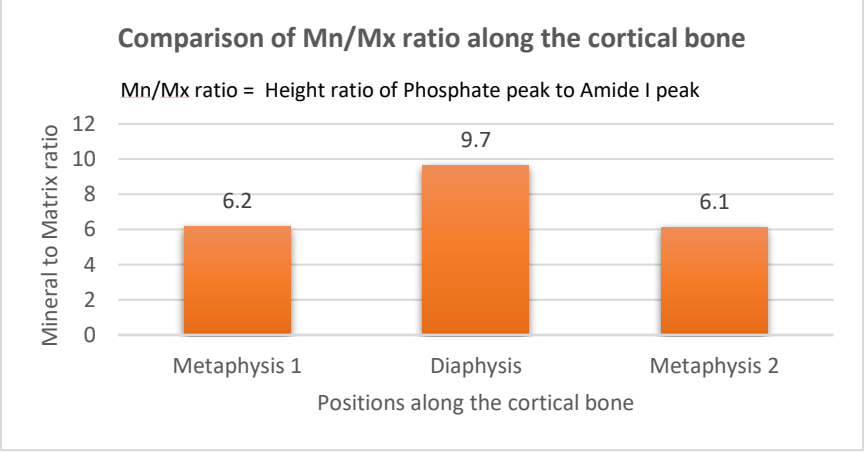

(b)

Figure 5-71 Cortical bone tibia—4-7-17 7F HL (KO) (a) Raman spectra (b) Mn/Mx ratio

5.2.4 Results and Discussion on Cortical Bone in the Tibia

Figure 5-72 shows the data taken from cortical bone of the tibia. It explains how mineral to matrix ratio changes throughout the sample from the top to the bottom of the tibia, which means from the metaphysis 1 to metaphysis 2. As with every other portion of bone, the results are shown in a way that includes the average of the same area of tibia but from all different samples. Figure 5-72 shows the averages including nine WT and six KO samples.

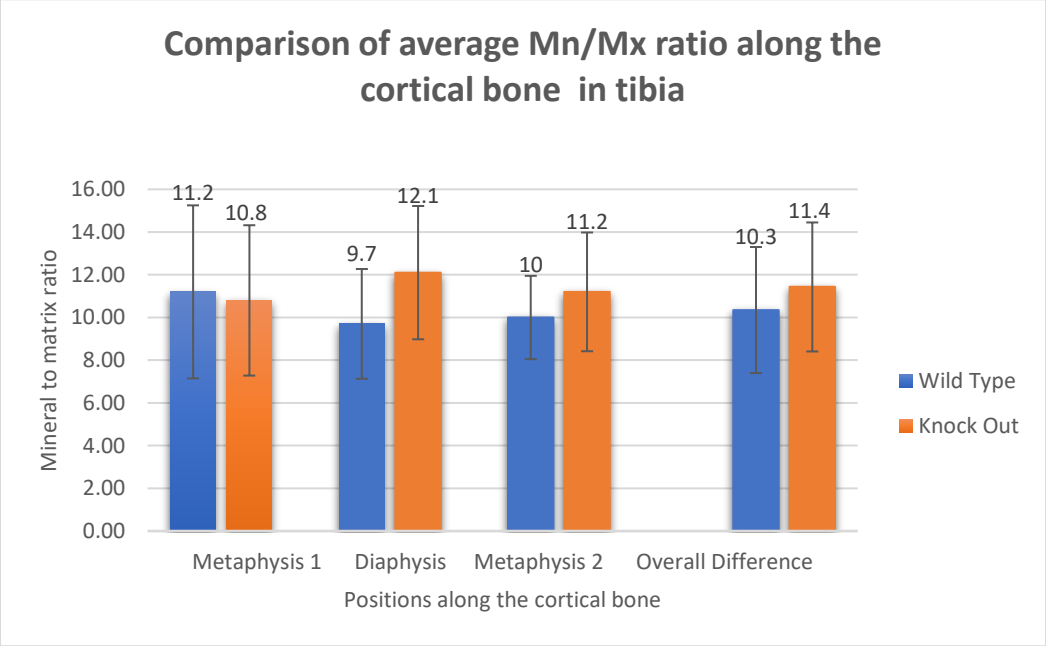

Figure 5-72 Average Mn/Mx ratio of different positions along the cortical bone in tibia

By observing the results shown in Figure 5.72, it is very clear that the diaphysis region of cortical bone from tibia in KO shows a much higher ratio than in WT. But the other two positions, which are the two metaphysis ends, show a very close average Mn/Mx ratio for WT and KO; however, the overall difference remains higher in KO than in WT. Since the gene deficiency plays a crucial role in the cortical bone of tibia, we

confined our further study to this portion. Later, we started our detailed study on the diaphysis region where crystal growth is mature [36]. The diaphysis region of cortical bone of the tibia, gives us a mineral to matrix ratio that we can correlate with the disorders.

5.3 Detailed Study on Diaphysis of Tibia

The following graph in Figure 5-73 represents the variation of Mn/Mx ratio of the diaphysis of the tibia from the different samples. There is a large-scale variance of mineral and matrix content for different samples. One of the KO bones shows a very high ratio and one of the WT shows a very low ratio because of the heterogeneous structure of bone.

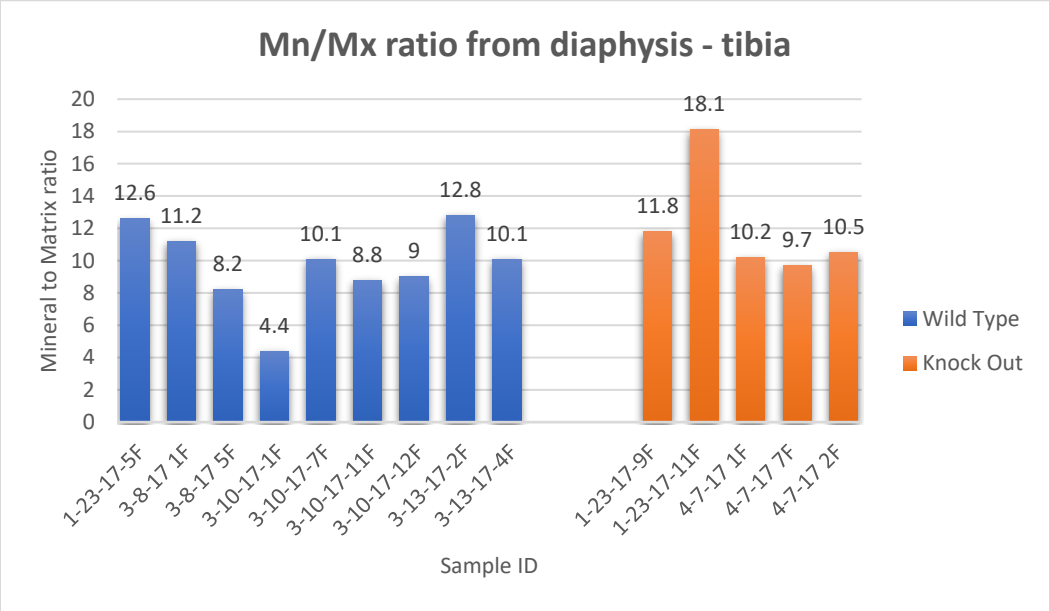

Figure 5-73 Mn/Mx ratio of diaphysis in the tibia of different samples

With Raman spectroscopy, it is difficult to detect a specific phase (mineral/matrix) as it does not show microstructure and the surface morphology. The maximum magnification through DXR Raman is 100X. Spot detection means that at a single time, the length covered by the laser is 3.1µm with the 10X lens that we used. Thus, relying on

the one single spot does not give an accurate result. If the detected spot contains more minerals than other phases, it will provide a high Mn/Mx ratio. In the same way, if the presence of any amide/protein on the detected spot is more, it will provide us with a low Mn/Mx ratio. To find the best way to overcome this limitation, we decided to collect several spectra from very near and small areas. Averaging of spots collected from a very small area gave us reliable Mn/Mx ratios. As shown in Figure 5-74, we took eight spots from a very small area (blue in the Figure) in five different samples, of which two samples were WT and three samples were KO.

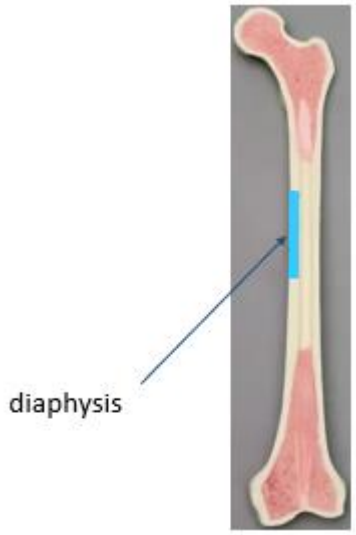

Figure 5-74 Image showing only diaphysis position of the cortical bone

5.3.1 Raman Spectra and Mn/Mx Ratio of Tibia Diaphysis in WT/KO Rat Bones

(1) Wild-type samples

For the study of the diaphysis region, we confined our analysis to a limited spectral range. Figure 5-75a shows the reproducibility of the results as all the spectra overlap one another at the same wavenumbers. Figure 5-75b shows the consistency in the results. Other than spot 3 and spot 4, all the spots represent an Mn/Mx ratio that falls in the range of 11.0 to 12.0.

(i) 3-8-17 1F HL

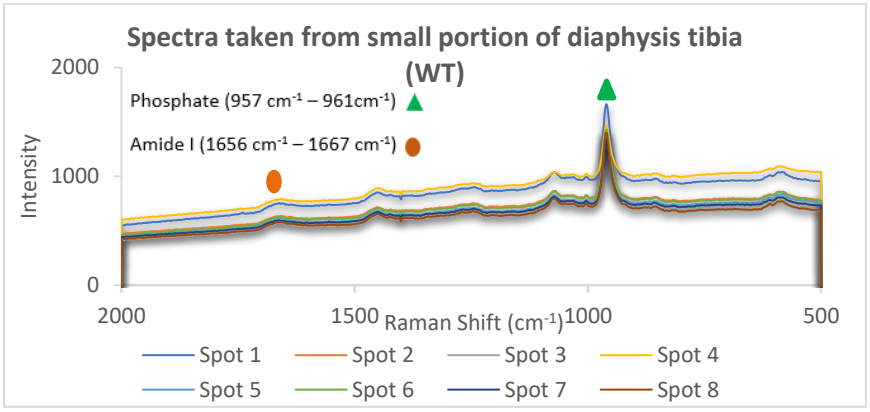

(a)

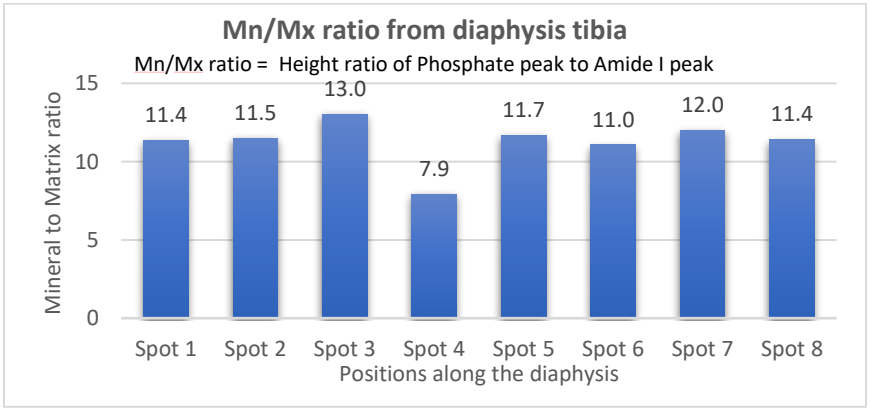

(b)

Figure 5-75 Mid-diaphysis tibia—3-8-17 1F HL (WT) (a) Raman spectra (b) Mn/Mx ratio

(ii) 3-8-17 5F HL

Figure 5-76a shows the reproducibility of the results. All the peaks match the wavenumbers for all of the different positions. The reproducibility of these data gives confidence in the accuracy of the results. Unlike the previous sample, the ratios for different positions vary in the range of 6.5 to 9.5 (as shown in Figure 5-76b).

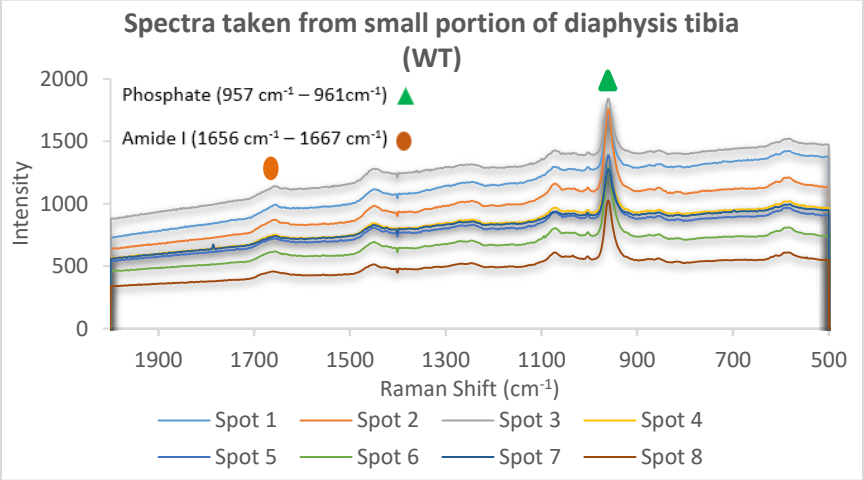

(a)

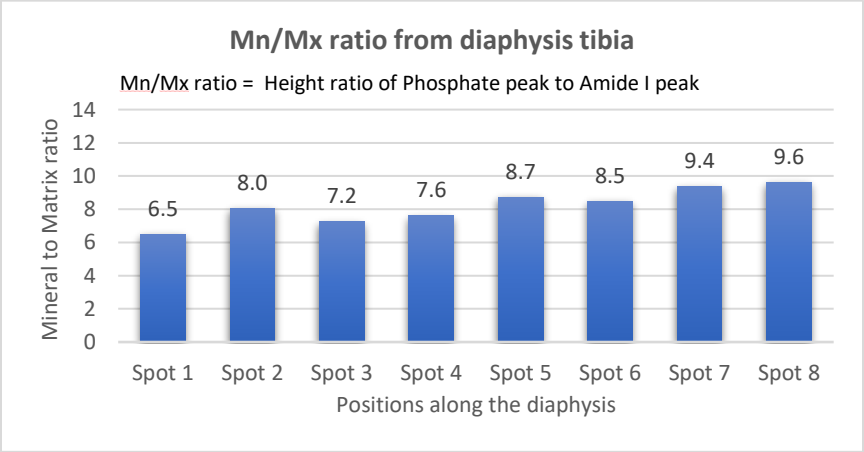

(b)

Figure 5-76 Mid-diaphysis tibia—3-8-17- 5F HL (WT) (a) Raman spectra (b) Mn/Mx ratio

(1) Knockout samples

(i) 4-7-17 1F HL

Similar to the previous two samples, this sample also shows the strong reproducibility of the spectra for the different positions (as shown in Figure 5-77a). The phosphate peak height for all the spots is relatively low compared to the previous two samples. Figure 5-77b shows the consistency in Mn/Mx ratios for all the positions, even more than the wild-type samples.

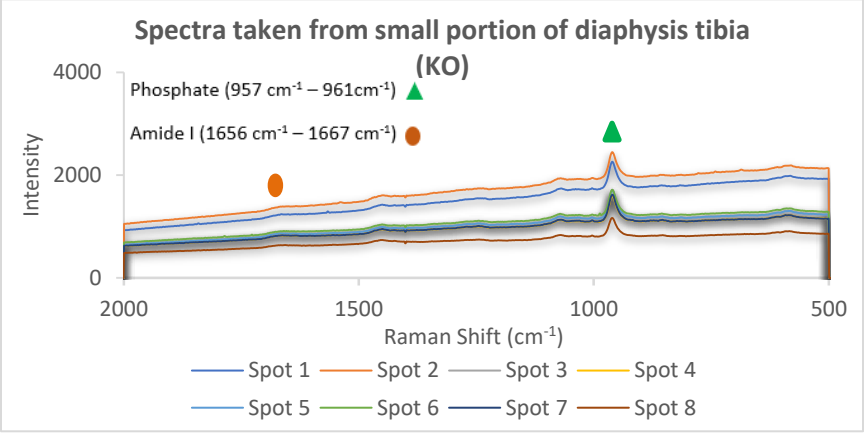

(a)

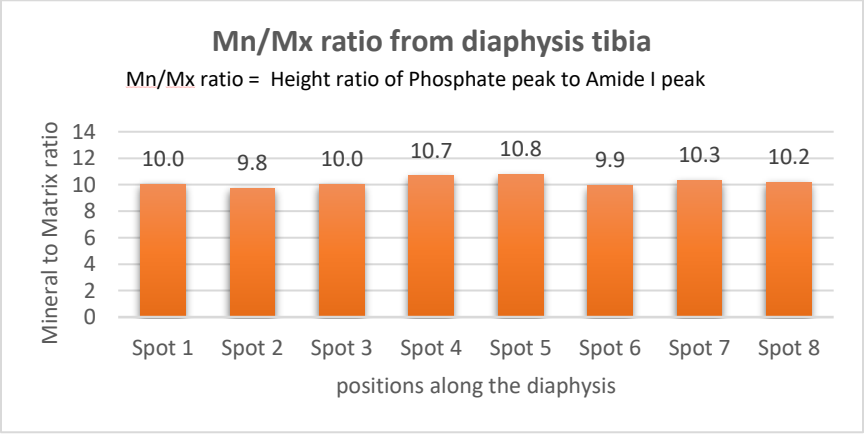

(b)

Figure 5-77 Mid-diaphysis tibia—4-7-17 1F HL (KO) (a) Raman spectra (b) Mn/Mx ratio

(ii) 4-7-17 2F HL

Figure 5-78a shows that reproducibility of the spectra still remains for this sample as well. Compared to the previous KO sample, this sample shows a higher height for the phosphate peak. However, compared to the last KO sample, there is more variance present in the Mn/Mx ratios of all the positions (as shown in Figure 5-78b).

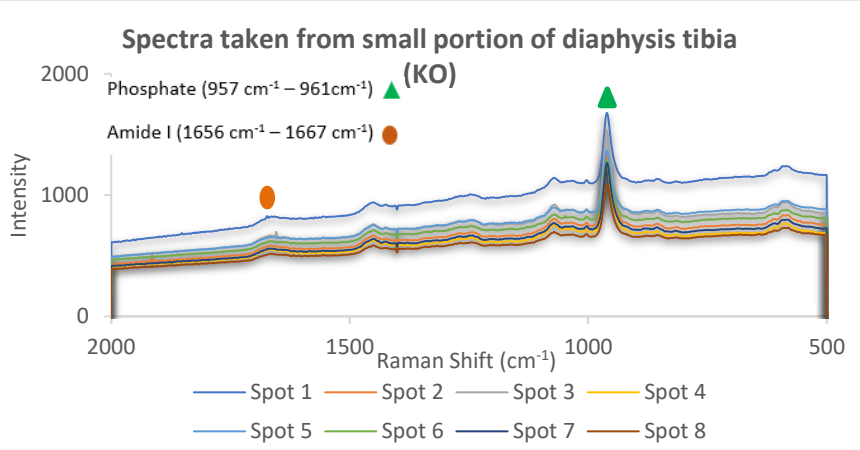

(a)

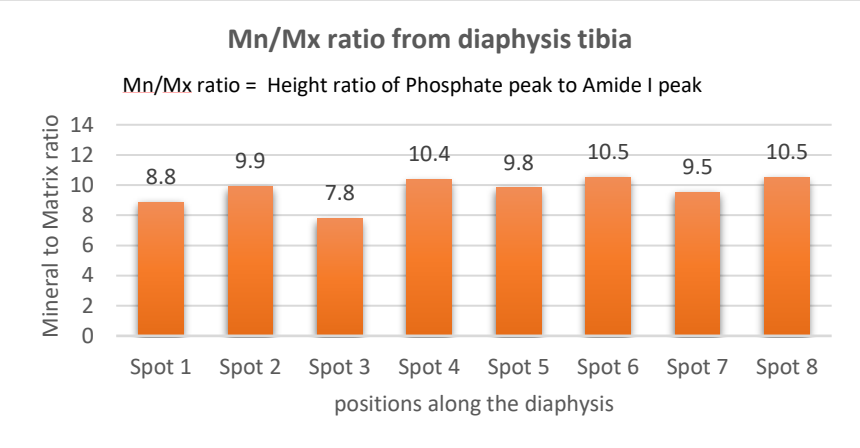

(b)

Figure 5-78 Mid-diaphysis tibia—4-7-17 2F HL (KO) (a) Raman spectra (b) Mn/Mx ratio

(iii) 4-7-17 7F HL

With reproducibility of the spectra as shown in the Figure 5-79a, this sample also shows less variation in the Mn/Mx ratio for the different positions (Figure 5-79b). A careful observation of all five samples supports the fact that the diaphysis region gives less variation in Mn/Mx ratio. The average ratio comparison between WT and KO can give us the best correlation of those with mechanical properties and disorders in the bone.

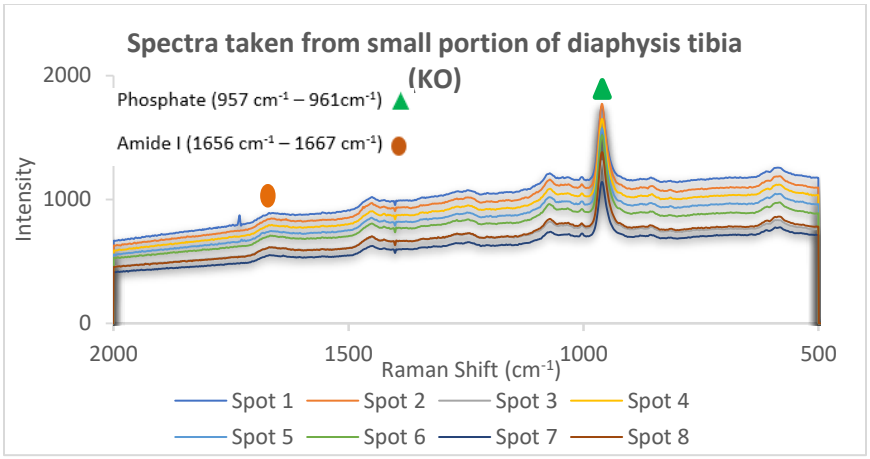

(a)

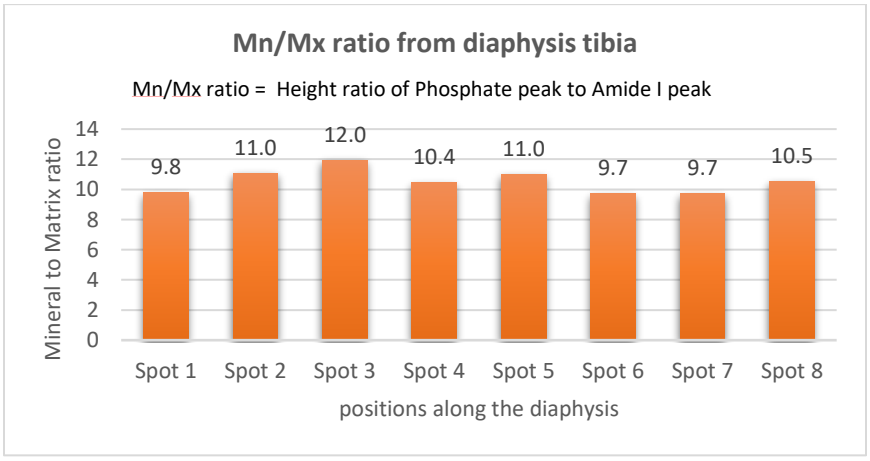

(b)

Figure 5-79 Mid-diaphysis tibia—4-7-17 7F HL (KO) (a) Raman spectra (b) Mn/Mx ratio

5.3.2 Results and Discussion on Diaphysis of Tibia

The graph in Figure 5.80 shows the variance in Mn/Mx ratio of small areas with more spots. It is observable from the graph that KO bones show a higher ratio than WT, which means the results favor the hypothesis made at the beginning of the research. The following Figure shows the averages including 2 WT and 3 KO samples.

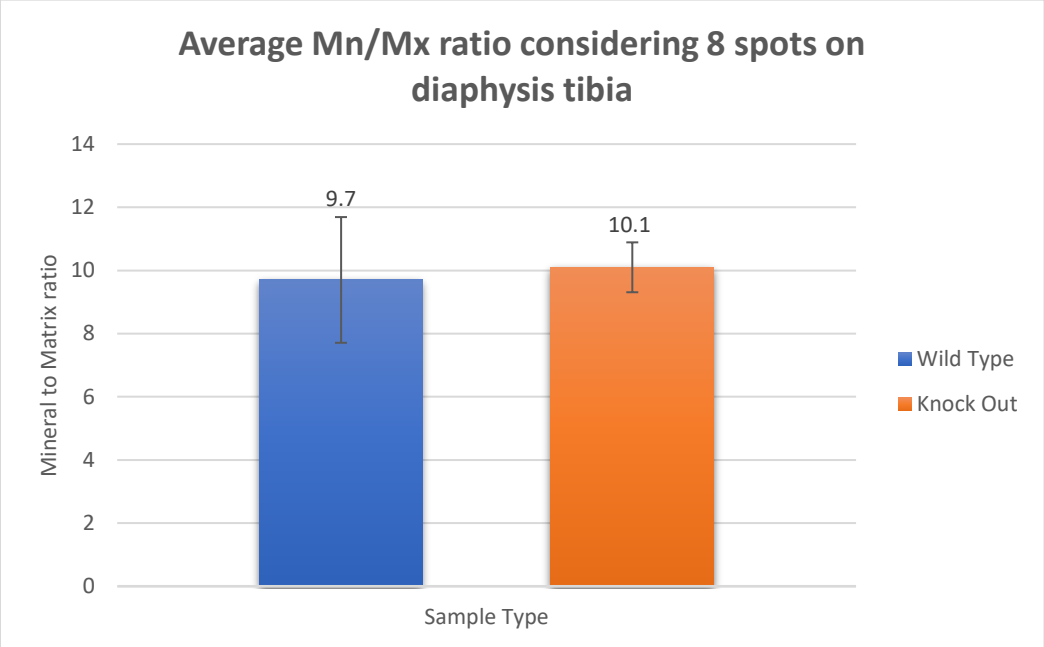

Figure 5-80 Mn/Mx ratio considering eight points

5.4 Mn/Mx ratio from Cortical Bone according to Age Group.

The following graph in Figure 5.81 shows the difference between the average Mn/Mx ratio of the different age group of rat bones from the cortical bone tibia. There is no separation of WT and KO rat bones shown as we did not have KO bones from all kinds of age groups. It is clearly shown that the oldest rat bones have higher Mn/Mx compared to other groups, whereas all other groups do not show a significant difference. The reason for the older age group with higher mineral content is the time of growth. As mentioned above, there have already been some studies that have shown higher Mn/Mx

ratios with increasing age.

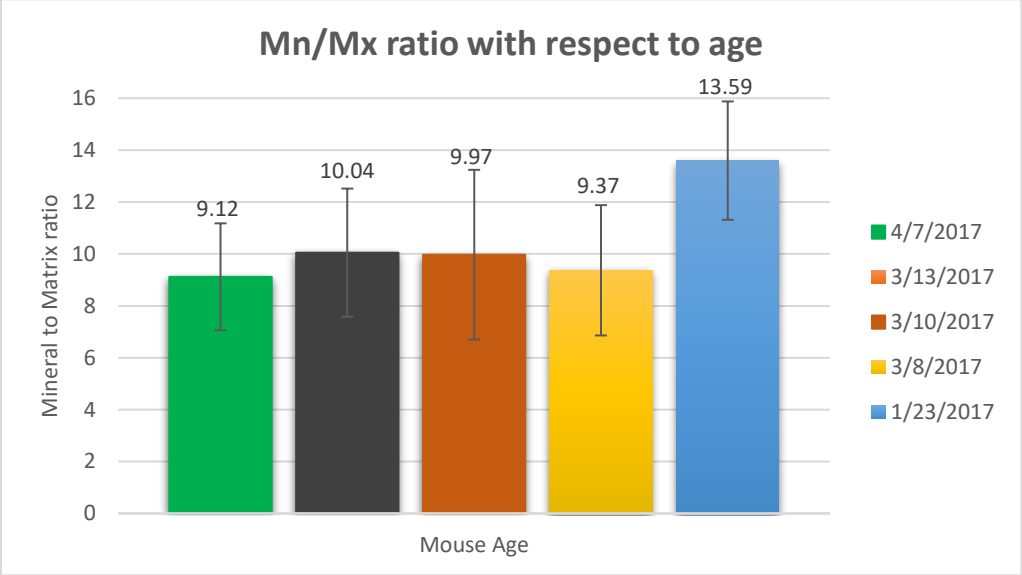

Figure 5-81 Variance in average Mn/Mx ratio of different age group

Chapter 6 Energy-Dispersive Spectroscopy of WT/KO Bones

6.1 SEM and EDS on the Cortical Bone Tibia

In addition to Raman spectroscopy, we used EDS mapping and EDS compositional analysis to verify data obtained from Raman Spectroscopy. Our plan was to check whether the amount of calcium and phosphorus as part of the minerals and the amount of nitrogen as part of the matrix directly correlates with the data obtained from Raman spectroscopy or not. To accomplish that, we analyzed four different samples with SEM-EDS, two of which were WT and other two were KO. We used the high vacuum method. It is necessary for the sample to be conductive for this method. Bone is nonconductive in nature, so to overcome this difficulty, we used the sputtering process to coat the bone with silver. In SEM-EDS, the area under observation is very important.

We have captured some images with SEM as shown in Figure 6.1. We captured most of the images at 400X. As we wanted to cover more area in the EDS for the compositional analysis, we decided not to go with higher magnification than 400X. The higher the area, the better the chance of covering different phases. As shown in the SEM images at 400X, the area covered by the image is a couple hundred micrometers, which can easily cover different cells present in the matrix. Standard cell size remains between 5 µm and 20 µm [37] [38]. This way, we can avoid detecting only a mineral dominant area or only a matrix dominant area. This area of the image at 400X clearly distinguishes between the higher minerals and the higher matrix region in EDS mapping.

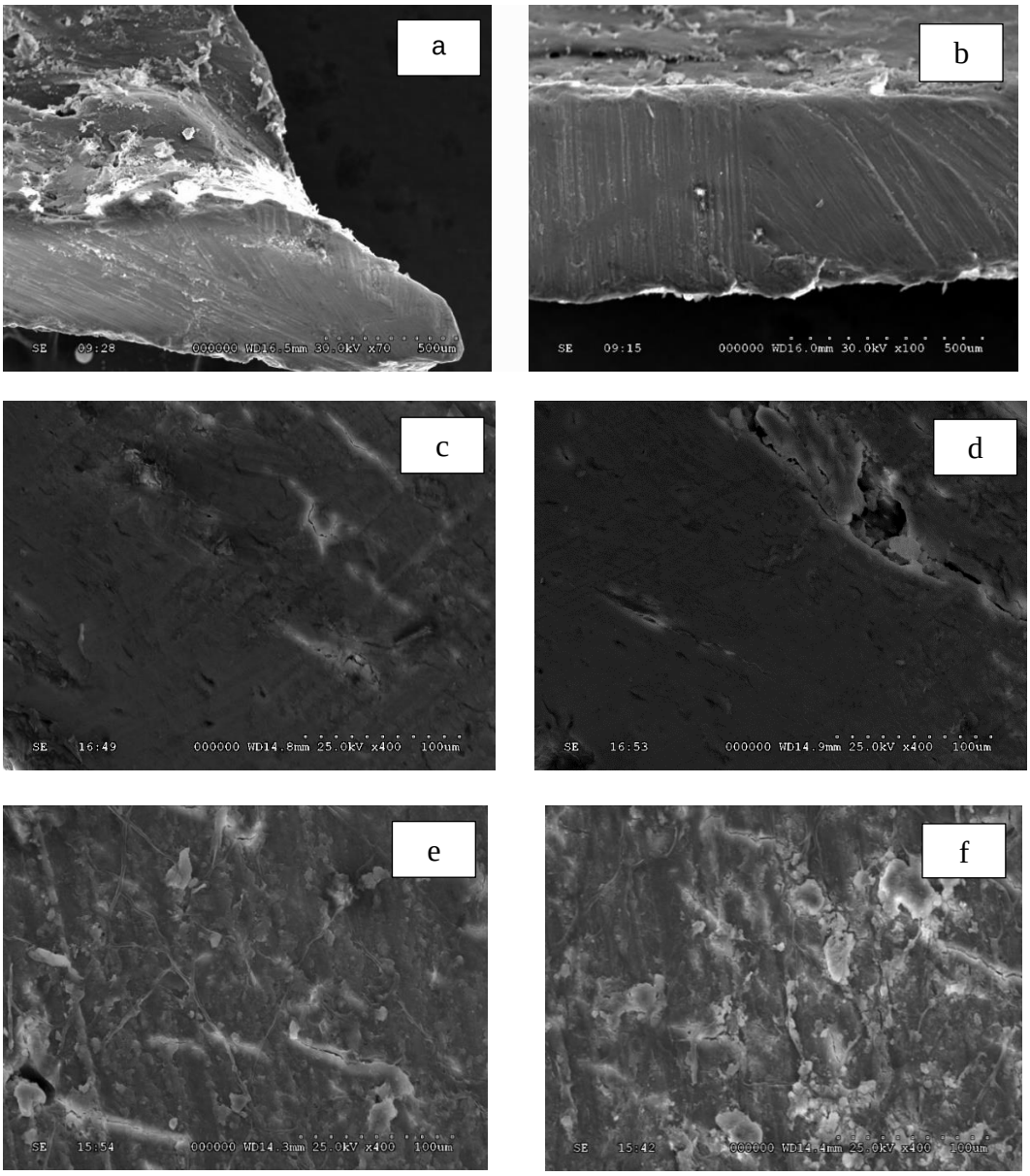

Figure 6-1 SEM Images of cortical bone (a) image—distinguish the cortical and cancellous bone (500 µm) (b) image—focusing on cortical bone (500 µm) (c), (d), (e), (f) images focused on microregions of mid diaphysis (100 µm)

6.2 Interpretation of EDS Mapping Analysis

The Figure 6-3a and b show the average elemental composition of WT and KO.

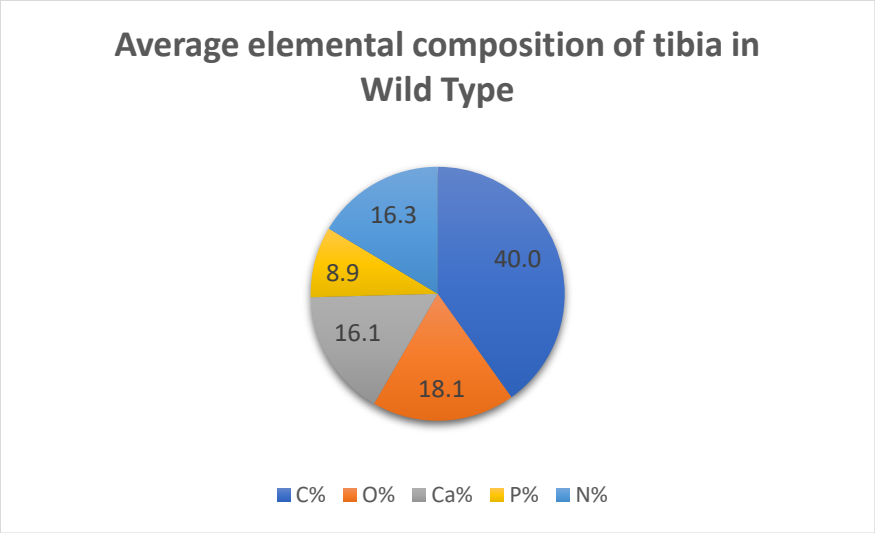

(a)

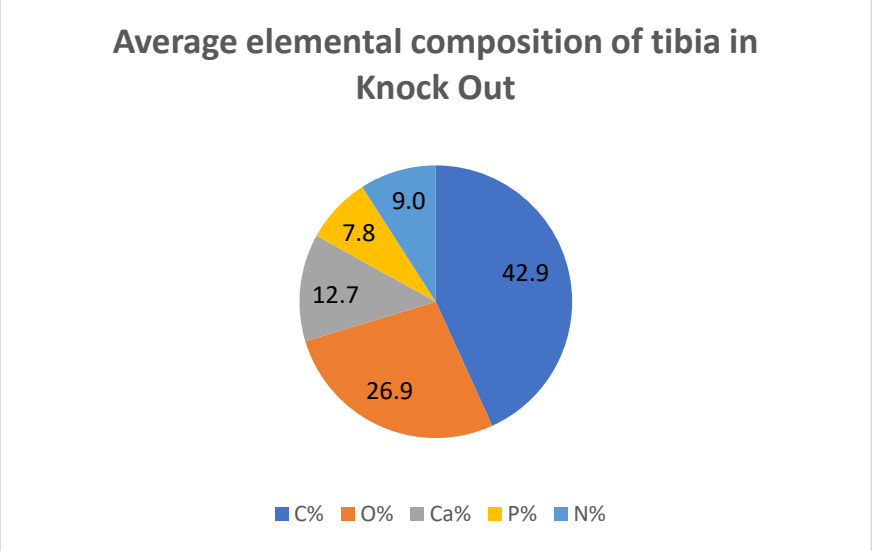

(b)

Figure 6-2 Average elemental composition of tibia in (a) WT (b) KO

It was difficult to find a direct relation of EDS compositional analysis with the ratio obtained from Raman spectroscopy. The WT should have a lower amount of minerals and higher matrix content than KO. The elemental composition analysis partially matches with Raman results because the average composition of calcium is higher in WT than in KO, and there is very little difference in the amount of phosphorous between WT and KO. But it is a fact that these elements in the bone are not present in their elemental form. As indicated in Figure 6.2, all of these elements are present in compound form, with different elements by sharing electrons. The following chemical formulae of minerals and matrix make it clear:

Minerals = Hydroxyapatite = $Ca_5(PO_4)_3(OH)$, Carbonate = (CO_3^{2-})

Matrix =

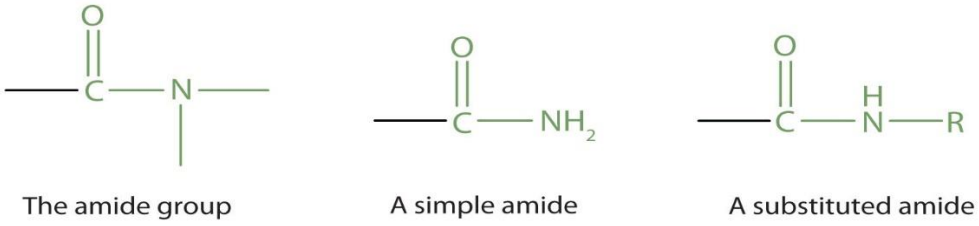

Figure 6-3 Image showing amides

Proline = $C_5H_9NO_2$, Hydroxyproline = $C_5H_9NO_3$

Observing all the chemical formulae of the different phases, it is clear that there is only one element, Ca, which is not present in the matrix; in minerals, it is present in the elemental form. So ideally, KO bones should contain higher calcium content than WT. But the presence of calcium is higher in the WT than in the KO. There is a substitution process that occurs during crystal reformation. In this process, Ca^{2+} ions are replaced by Cu, Si, or Zn, and those ions might be carried away with blood [39]. There is also one

more element, nitrogen, which is not at all present in the minerals. Nitrogen primarily represents the matrix portion. WT must have a higher amount of nitrogen than KO, which is satisfied by the EDS compositional analysis. Carbon is present in both mineral and matrix. Thus, it is difficult to correlate the composition of carbon to the Mn/Mx ratio. Besides these elements, there is one more important element left, oxygen. Minerals contain hydroxyapatite and carbonate; as a result, KO bones have a higher amount of oxygen than WT.

6.3 EDS Mapping of a Wild-Type Rat

To understand the concept of bonding as discussed above and the correlation of combined Raman and EDS compositional analysis, we carried out EDS mapping. This technique comes out as a strong way of observing the surface arrangement of the different elements. As discussed above, elements like phosphorous, carbon, and nitrogen can all combine with oxygen. Thus, oxygen should be present everywhere on the bone, whether it is the dense region of phosphorous, carbon, or nitrogen. Figure 6-4 below shows the distribution of elements. The lowermost zone is occupied with carbon and nitrogen, whereas the upper zone is filled with calcium and phosphorous. But it is clearly observable that oxygen is everywhere in the area, which proves the point discussed above.

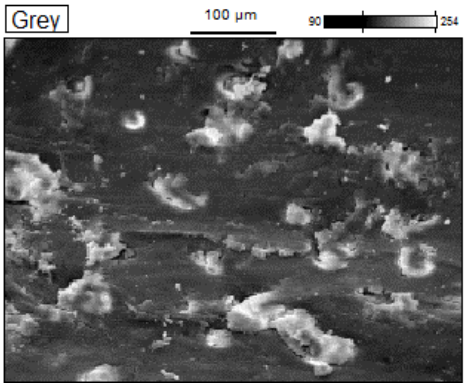
Grey
100 µm
90
254

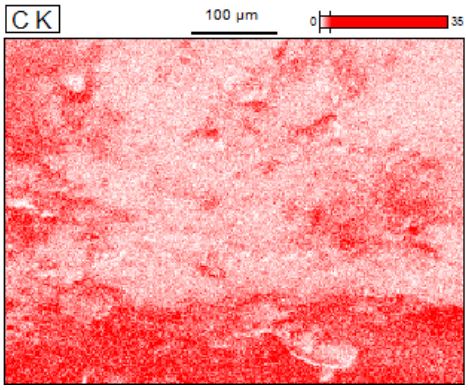
C K
100 µm
0
35

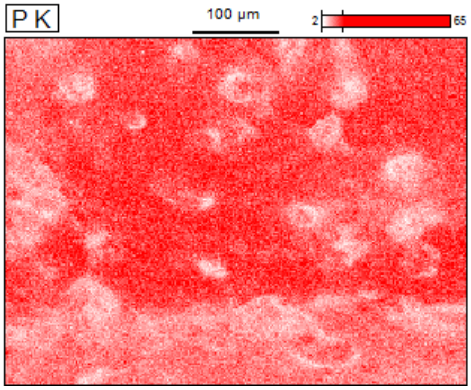
P K
100 µm
2
65

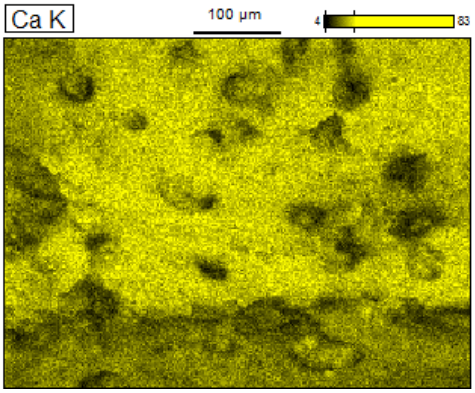
Ca K
100 µm
4
83

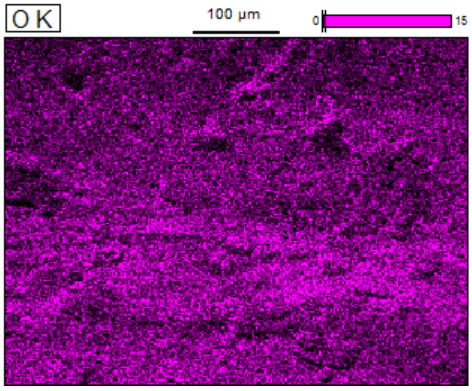
O K
100 µm
0
15

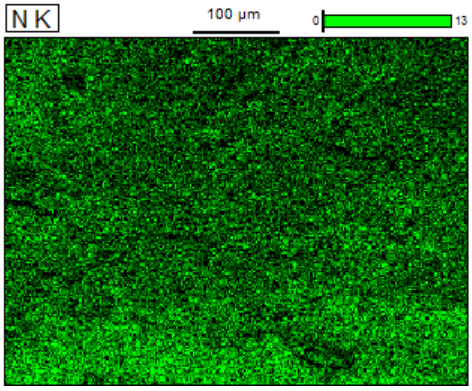
N K
100 µm
0
13

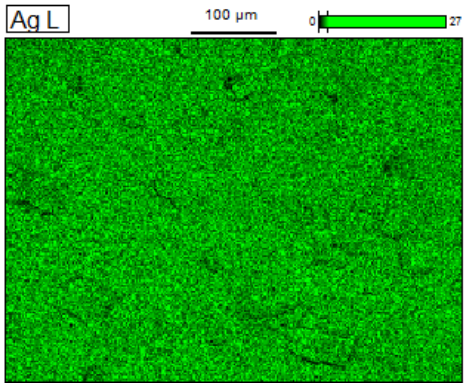
Ag L
100 µm
0
27

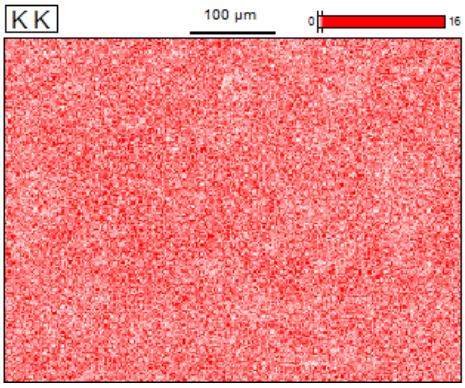
K K
100 µm
0
16

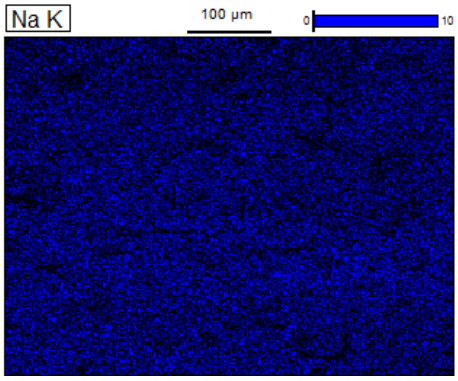
Na K
100 µm
0
10

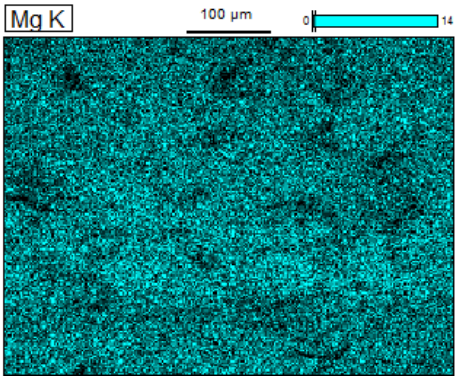
Mg K
100 µm
0
14

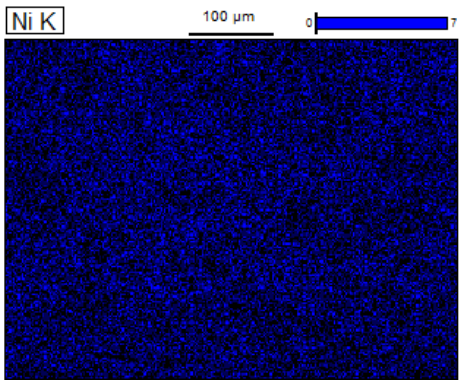
Ni K
100 µm
0
7

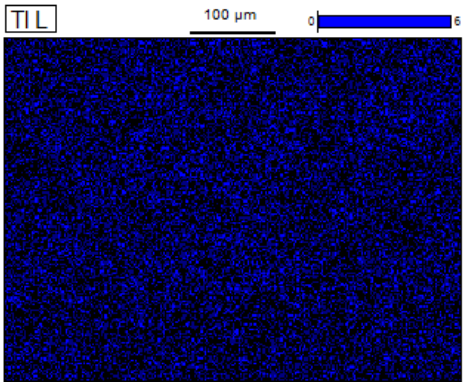
Tl L
100 µm
0
6

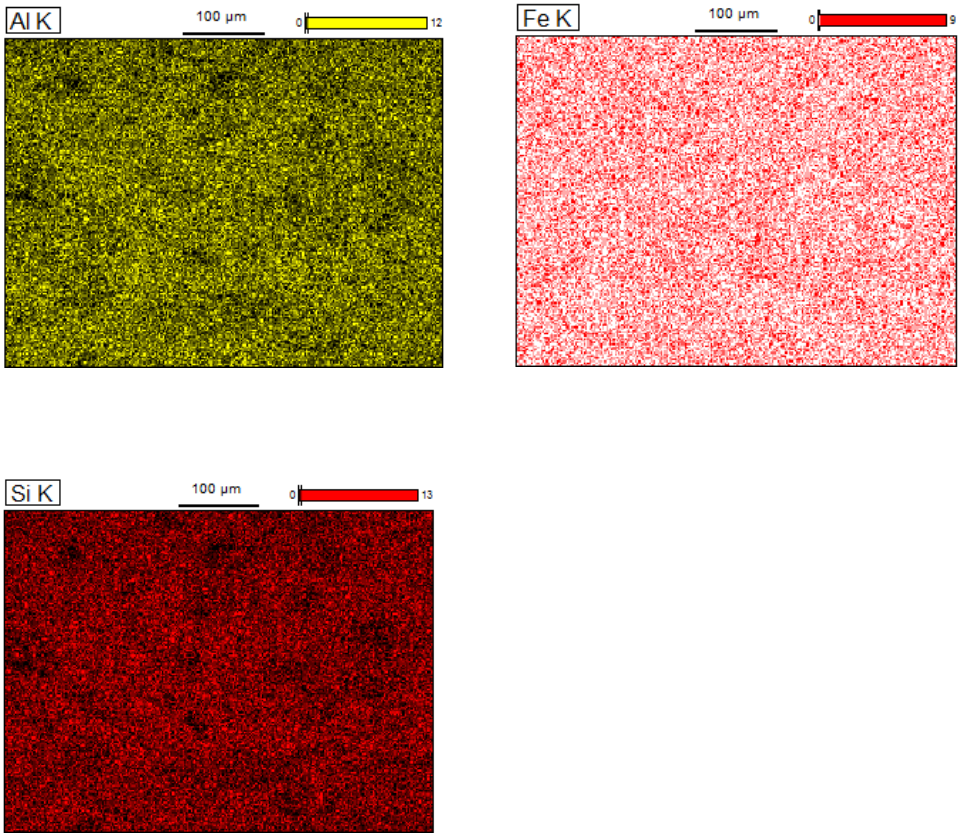

Figure 6-4 WT Elemental mapping images

Chapter 7 Conclusion and Future Work

7.1 Conclusion

The study of the mid-diaphysis region of the cortical bone gives reliable discrimination between WT and KO. The mid-diaphysis portion of the KO bones shows around 5% higher minerals than the WT in tibia, which satisfies the anticipation of increased mineral to matrix content due to FSTL5 disability. EDS compositional analysis and EDS mapping enhance the results of Raman, showing higher minerals in KO than WT and making it clear that nitrogen presence is higher in the WT than KO. Raman spectroscopy proves to be a very strong technique in finding the mineral and matrix content present in the bone. Raman spectroscopy can be a useful tool to determine the etiology of clubfoot.

7.2 Future Work

Focusing on the matured portions of bone (the middle of the femur and the tibia) and exploring a number of spots and averaging out all could give robust and reliable data. X-ray diffractometry could be a useful tool to see the pattern of minerals saturated in the wild-type and the knockout.

References

[1] Wynne-Davies, R. (1964). "Family studies and the cause of congenital club foot." *The Journal of Bone and Joint Surger 46.3,* 445-463.

[2] Dobbs, M. B., & Gurnett, C. A. (2009). "Update on clubfoot: etiology and treatment." *Clinical Orthopaedics and Related Research 467.5,* 1146-1153.

[3] Hoshino, A., and W. A. (1987). "Impact-absorbing properties of the human knee." *Bone & Joint Journal 69.5,* 807-811.

[4] Dorozhkin, S. V., & Matthias. (2002). "Biological and medical significance of calcium phosphates." *Angewandte Chemie International Edition 41.17,* 3130-3146.

[5] Currey, J. D. (1969). "The mechanical consequences of variation in the mineral content of bone." *Journal of Biomechanics 2.1,* 1-11.

[6] Currey, J. D., Brear, K., & Zioupos, P. (1997). "The effects of ageing and changes in mineral content in degrading the toughness of human femora." *Journal of Biomechanics 29.2,* 257-260.

[7] Burstein, A. H. (1975). "Contribution of collagen and mineral to the elastic-plastic properties of bone." *The Journal of Bone and Joint Surgery 57.7,* 956-961.

[8] Burr, D. B. (2002). "Bone material properties and mineral matrix contributions to fracture risk or age in women and men." *Journal of Musculoskeletal and Neuronal Interactions 2.3,* 201-204.

[9] Yerramshetty, J. S., & Ozan A. (2008). "The associations between mineral crystallinity and the mechanical properties of human cortical bone." *Bone 42.3,* 476-482.

[10] Wang, X., Bank R. A., Tekkoppele J. M., & Agrawal M. C. (2001). "The role of collagen in determining bone mechanical properties." *Journal of Orthopaedic Research 19.6,* 1021-1026.

[11] Burr, D. B. (2002). "The contribution of the organic matrix to bone's material properties." *Bone 31.1,* 8-11.

[12] Lewis, I. R., & Edwards, H. (2001). *"Handbook of Raman spectroscopy: from the research laboratory to the process line."* Boca Raton: Taylor and Francis Group, LLC.

[13] Butler, Holly J., Ashton, L., Bird B., Cinque, G., Curtis K., Dorney, J., . . .Fullwood, N. J. (2016). "Using Raman spectroscopy to characterize biological materials." *Nature Protocols 11.4,* 664 - 687.

[14] Mandair, G. S., & Morris, M. D. (2015). "Contributions of Raman spectroscopy to the understanding of bone strength." *BoneKEy Reports 4 620.*

[15] Timlin, J. A., Carden, A., & Morris, M. D. (2000). "Raman spectroscopic imaging markers for fatigue-related microdamage in bovine bone." *Analytical Chemistry 72.10,* 2229-2236.

[16] Morris, M. D., Carden, A., Rajachar, R, M., & Kohn, D. H. (2002). "Effects of applied load on bone tissue as observed by Raman spectroscopy." *Biomedical Vibrational Spectroscopy International Society for Optics and Photonics 4614,* 46-54.

[17] Carmejane, O., Morris, M. D., Davis, M. K., Stixrude, L., Tecklenburg, M., & Kohan D. H. (2005). "Bone chemical structure response to mechanical stress studied by high pressure Raman spectroscopy." *Calcified Tissue International 76.3,* 207-213.

[18] Carden, A., Rajachar R.M., Morris, M. D., & Kohn, D. H. (2003). "Ultrastructural changes accompanying the mechanical deformation of bone tissue: A Raman imaging study." *Calcified Tissue International 72.2,* 166-175.

[19] Akkus, O., Fran, A., & Schaffler, M. B. (2004). "Age-related changes in physicochemical properties of mineral crystals are related to impaired mechanical function of cortical bone." *Bone 34.3,* 443-453.

[20] Tarnowski, C. P., Ignelzi, M. A., & Morris, M. D. (2002). "Mineralization of developing mouse calvaria as revealed by Raman microspectroscopy." *Journal of Bone and Mineral Research 17.6,* 1118-1126.

[21] Akkus, O., Polyakova-Akkus A., Fran A., Schaffler, M. B. (2003). "Aging of microstructural compartments in human compact bone." *Journal of Bone and Mineral Research18.6,* 1012-1019.

[22] Timlin, J. A., Carden, A., Morris, M. D., Bonadio J. F., Hoffler C. E., Kozloff, K., & Goldstein S. A. (1999). "Spatial distribution of phosphate species in mature and newly generated mammalian bone by hyperspectral Raman imaging." *Journal of Biomedical Optics 4.1,* 28-35.

[23] Beier, E. E., Maher J. R., Sheu, T., Cory-Slechta D. A., Berger A. J., & Zuscik, M. J. (2013). "Heavy metal lead exposure, osteoporotic-like phenotype in an animal model, and depression of Wnt signaling." *Environmental Health Perspectives 121.1,* 97 - 104.

[24] Kozloff, K. M., Carden A., Bergwitz, C., Forlino, A., Uveges, T. E., Morris, M. D., Marini J. C., & Goldstein S. A. (2004). "Brittle IV mouse model for osteogenesis imperfecta IV demonstrates postpubertal adaptations to improve whole bone strength." *Journal of Bone and Mineral Research 19.4,* 614-622.

[25] Dehring, K. A., Crane, N. J., Smukler, A. R., McHugh J. B., Roessler B. J., & Morris M. D. (2006). "Identifying chemical changes in subchondral bone taken from murine knee joints using Raman spectroscopy." *Applied Spectroscopy 60.10,* 1134-1141.

[26] McCreadie, B. R., Morris, M. D., Chen T., Rao, D. S., Finney W. F., & Goldstein, S.A. (2006). "Bone tissue compositional differences in women with and without osteoporotic fracture." Bone 39.6, 1190-1195.

[27] Crane, N. J., Popescu, V., Morris, M. D., Steenhuis, P., & Ignelzi, M. A. (2006). "Raman spectroscopic evidence for octacalcium phosphate and other transient mineral species deposited during intramembranous mineralization." *Bone 39.3,* 434-442.

[28] Kazanci, M., Fratz, P., Klaushofer, K., & Paschalis E. P. (2006). "Complementary information on in vitro conversion of amorphous (precursor) calcium phosphate to hydroxyapatite from Raman microspectroscopy and wide-angle X-ray scattering." *Calcified Tissue Iinternational 79.5,* 354-359.

[29] Awonusi, A., Morris, M. D., & Tecklenburg, M. J. (2007). "Carbonate assignment and calibration in the Raman spectrum of apatite." *Calcified Tissue International 81.1,* 46-52.

[30] Schulmerich, M. V., Dooley, K. A., Vanasse T. M., Goldstein S. A., & Morris, M. D. (2007). "Subsurface and transcutaneous Raman spectroscopy and mapping using concentric illumination rings and collection with a circular fiber-optic array." *Applied Spectroscopy 61.7,* 671-678.

[31] Crane, N. J., Morris, M. D., Ignelzi, M. A., & Yu, G. G. (2005). "Raman imaging demonstrates FGF2-induced craniosynostosis in mouse calvaria." *Journal of Biomedical Optics 10.3,* 1-8.

[32] Pienkowski, D., Dores, T. M., Monier-Faugere, M., Gemg, Z., Camancho, N. P., Boskey, A. L., & Malluche, H. H. (1997). "Calcitonin alters bone quality in beagle dogs." *Journal of Bone and Mineral Research 12.11,* 1936-1943.

[33] Ou-Yang, H., Paschalis, E. P., Mayo, W. E., Boskey, A. L., & Mendelsohn R. (2001). "Infrared microscopic imaging of bone: spatial distribution of CO32−." *Journal of Bone and Mineral Research 16.5,* 893-900.

[34] Legros, R., Balmain, N., & Bonel, G. (1987). "Age-related changes in mineral of rat and bovine cortical bone." *Calcified Tissue International 41.3,* 137-144.

[35] Chan, J. W., Taylor, D. S., Zwerdling, T., Lane, S. M., & Ihara, K. et al. (2006). "Micro-Raman spectroscopy detects individual neoplastic and normal hematopoietic cells." *Biophysical Journal 90.2,* 648-656.

[36] Boskey, A. L., Spevak, L., Paschalis, E., Doty, S. B., & Mckee, M. D. (2002). "Osteopontin deficiency increases mineral content and mineral crystallinity in mouse bone." *Calcified Tissue International 71.2,* 145-154.

[37] Tanaka-Kamioka, K., Kamioka, H., Ris, H., & Lim, S. (1998). "Osteocyte shape is dependent on actin filaments and osteocyte processes are unique actin-rich projections." *Journal of Bone and Mineral Research 13.10,* 1555-1568.

[38] Sugawara, Y., Kamioka, H., Honjo, T., Tezuka, K., & Yamamoto, T. (2005). "Three-dimensional reconstruction of chick calvarial osteocytes and their cell processes using confocal microscopy." *Bone 36.5,* 877-883.

[39] Smith, E. L. (1983). *"Principals of Biochemistry: General Aspects and Mammalian Biochemistry."* New York: McGraw-Hill.

Biographical Information

Meet Shah has completed his master's in Materials Science and Engineering from the University of Texas at Arlington (UTA). He earned his bachelor's degree in the Metallurgical and Materials Engineering from the Indus University, India. He has two years of experience in characterization working as a research assistant at UTA. He has worked as a President of American Society of Materials (ASM) – UTA Chapter. He wants to pursue his career in the fields like failure analysis and reliability, materials characterization, semiconductor/ corrosion Industry.